An Assessment of Extreme Mooring Loads for Floating Offshore Wind Structures Using Conditional Waves

Aminda Marlen Titlestad Ripe

Master's Thesis in Ocean Technology

University of Bergen,

Department of Physics and Technology

August 3, 2022

Abstract

Wind power is one of the fastest-growing industries in the world and plays a significant role in the transition to sustainable energy systems. However, the costs of substructures and moorings limit the potential of floating wind turbines to be placed at depths greater than 60 m with stronger and steadier winds.

Experimental tests on two types of foundations for floating wind turbines at 1:100 scale representing a full-scale water depth of 220 meters have been tested in irregular sea states and conditional waves to study the relationship between local wave characteristics and extreme response and mooring loads. Both models are moored using a light mooring system mounted above the still water level, where the slack mooring lines for a spar buoy frequently induce snap loads, compared to a tauter mooring system for a semi-submersible float avoiding snap loads in all three sea states.

The irregular waves are modeled using JONSWAP spectra representing 50-year storm conditions. The conditional waves consist of a focused wave group embedded in a random background sea, called the Most likely Wave (MLW), and two wave series conditioned on the floater's transfer functions called the Most Likely Response Wave (MLRW) and Conditional Random Response Wave (CRRW). The conditional waves need new methods when calibrated to ensure their properties are preserved, whereas the methods used are experimental and cause significant uncertainties in the results. Still, the recorded mooring loads and responses at the focal time in MLRW and CRRW are higher for both models than recordings at the focal time in the MLW, indicating that the most extreme events do not necessarily arise from extreme wave heights. This is supported by findings in the 3-hour sea-states, where the top ten mooring loads in all three sea-states appear to correlate with the devices' dominant behavior.

The spar buoy is as well modeled in OrcaFlex in full-scale using experimental parameters as input. OrcaWave is used to compute the hydrodynamic coefficients, and the system characteristics in OrcaFlex are tuned after experimental decay tests. Despite a good agreement between the numerical and experimental decay tests, the short-term response statistics are severely underpredicted.

Sammendrag

Vindkraft er en av de raskest voksende industrien i verden og spiller en betydelig rolle i overgangen til bærekraftige energisystemer. Kostnadene til fundamenter og fortøyningsliner begrenser imidlertid potensialet til flytende vindturbiner til å utnytte områder med vanndybder større enn 60 m med sterkere og stødigere vindressurser.

Eksperimentelle tester på to typer fundamenter for flytende vindturbiner i 1:100 skala som representerer en fullskala vanndybde på 220 meter er testet i irregulære sjøtilstander og betingede bølger for å studere sammenhengen mellom lokale bølgeegenskaper og ekstrem respons og fortøyningsspenninger. Begge modellene er fortøyd ved hjelp av et lett fortøyningssystem montert over stillevannstanden, der de slakke fortøyningslinene for en sparbøye ofte induserer sjokklaster, sammenlignet med et strammere fortøyningssystem for en halvt nedsenkbare flyter, som representerer et mer realistisk system, unngår sjokklaster i alle tre sjøtilstandene.

De uregelmessige bølgene er modellert ved hjelp av JONSWAP-spektre som representerer 50-års stormforhold. De betingede bølgene som er studert er én bølgeserie med en fokusert bølgegruppe modellert i en tilfeldig sjø, kalt Most likely Wave (MLW), og to bølgeserier betinget på flyterens overføringsfunksjoner kalt Most Likely Response Wave (MLRW) og Conditional Random Response Wave (CRRW). De betingede bølgene krever nye metoder når de kalibreres for å sikre at deres egenskaper bevares, mens metodene som brukes her er eksperimentelle og forårsaker betydelige usikkerhetsmomenter i resultatene. Likevel er de målte fortøyningsbelastningene og responsene ved fokuspunktet i MLRW og CRRW høyere for begge modellene enn ved fokuspunktet i MLW, noe som indikerer at de mest ekstreme hendelsene ikke nødvendigvis oppstår ved ekstreme bølgehøyder. Dette støttes av funnene i 3-timers sjøtilstandene, der de ti mest ekstreme fortøyningslastene i alle tre JONSWAP sjøtilstandene ser

ut til å korrelere med enhetens dominerende, ekstreme oppførsel.

Sparbøyen er også modellert som en fullskala turbin i OrcaFlex med eksperimentelle parametere som input. OrcaWave brukes til å beregne de hydrodynamiske koeffisientene, og systemkarakteristikkene i OrcaFlex er justert etter eksperimentelle innsvigninstester. Til tross for en god overensstemmelse mellom de numeriske og eksperimentelle innsvigninstestene, er korttids-responsstatistikken svært underestimert.

Preface

This master's thesis is written as a part of an integrated master's program in Ocean Technology at the Department of Physics and Technology, University of Bergen (UiB). This 60 ECTS thesis specializes in marine installations and collaborates with the Western Norway University of Applied Sciences (HVL).

Several people at both institutions, amongst others, have contributed to this master's thesis. For this, I am very thankful for their dedication and everything I have learned from their experiences in the field.

First and foremost, I would like to thank my supervisor, Dr. David Roger Lande-Sudall (HVL), for his guidance and support throughout this project and for providing excellent knowledge in hydrodynamics. I would also like to thank my internal supervisor at UiB, Dr. Harald Totland, for his help and feedback, and Irlin Nyland for showing tremendous support during a challenging time.

Furthermore, thanks to my fellow students at the university for five great years. A special thanks to Hannah Benus, for always having my back and for all the memories we have created over the years. Lastly, thanks to my loving family and boyfriend for patience, support, and reassurance throughout this year. Not mentioned, not forgotten - you have all made the last five years memorable, and for that, I am grateful.

Bergen, 20.07.2022

Aminda M. T. Ripe

Contents

1. Introduction

1.1 Background and Motivation

Wind power is one of the fastest-growing industries in the world and plays a significant role in the transition to sustainable energy systems [1]. The success of early floating offshore wind farm projects such as Hywind Scotland and WindFloat Atlantic, along with several projects currently in the planning stages, provide a promising means of increasing renewable energy production to meet Paris' 2°C target enshrined in the 2015 Paris Agreement [2].

Over the last decade, international efforts have been put in place to develop strategies to reduce GHG emissions. For example, in 2019, the European Union's Commission presented a roadmap for becoming climate neutral by 2050 [3], in which the installed offshore wind power capacity in the EU, including Norway and UK, is targeted to reach 450 GW in 2050 [4]. To meet these ambitious goals, significant obstacles, such as the costs of substructures for supporting wind turbines and the cost of the mooring system for floating structures, must be overcome in order to utilize floating offshore energy more effectively, especially in deep-water with floating wind farms that require multiple floating substructures [5]. Moorings have, in particular, shown to be a vulnerable component [6], with snap loads occurring in extreme conditions affecting fatigue [7; 8].

One way to make offshore wind energy economically competitive is by persisting in optimizing the platform that supports the floating offshore wind turbine (FOWT) to suit areas with stronger and steadier wind resources at water depths greater than 60 meters where bottom fixed substructures are not applicable [1; 9]. Currently, optimization of the platforms is mainly performed by hydrodynamic modeling in engineering tools, such as OrcaFlex [10] and OpenFast [11]. Nevertheless, such tools need prior knowledge of platform hydrody-

namic features to tune model coefficients. Wavebasin experiments with physical models are traditionally used to obtain the necessary information. Even though wavebasin experiments are generally reliable and efficient, they are not well-suited to accommodate the rapid design changes common to optimization processes [5]. Usually, multiple 3-hour sea-states are used with different seed numbers to ensure the most extreme events are considered, which can be significantly time-consuming and expensive. Therefore, using a wave series shorter than 3 hours but conditioned to excite the device's dominant, extreme behavior appears to be an effective method to reduce both computational time and the time needed in a wave tank.

Most platform designs are variations or combinations of three main concepts from the oil and gas industry: a spar buoy, semisubmersible, and a tension-leg platform (TLP). These are categorized by how they stabilize the system to prevent the wind turbines from tipping over in wind and wave excitations. The spar buoy concept is a long cylindrical-shaped structure with a deep draft that achieves stability through a ballast installed below its center of buoyancy and is characterized by its small vertical motions and large rotations. The semisubmersible achieves stability by distributing buoyancy widely at the water plane. It consists of large diameter columns connected by means of submerged pontoons. The spar buoy and semisubmersible are both usually moored using three catenary mooring lines for station keeping [12], and are the two platforms studied in this thesis.

Floating wind structures are smaller in size and highly sensitive to the coupling between the aero-hydro-servo-elastic loads compared to oil and gas installations. This introduces challenges for accurate hydrodynamic modeling of responses and mooring line loads in numerical codes, which can be sensitive to second- and higher-order effects [13] which must be considered. When these effects are not considered, device forces and response predictions can be inaccurate, resulting in an inherent conservatism in mooring system dimensioning. Therefore, verifying the hydrodynamic modeling in these codes is necessary to make the FOWT further economically competitive [5].

1.2 Related Work

Efforts have been made to verify the hydrodynamic modelling in numerical codes. An example of this is the third Offshore Code Collaboration (OC3) project, with an aim to verify the accuracy and correctness needed in the industry for aero-hydro-servo-elastic codes [14]. This project started in 2009 and has since extended its work in OC4 - OC6. Bottom fixed wind turbines were studied in the first three phases, where phase IV studied the NREL 5-MW baseline wind turbine described in [15] mounted on the Hywind Scotland floating spar buoy foundation. This foundation was positioned using three catenary mooring lines in deep water (320 m). The results from this case study were compared between participants across academics and industry using different industrial codes, such as Simo (Sesam) and Ansys AQWA, to mention a few. This project demonstrated that codes with hydrodynamic models based on Morison's equation and extended to include hydrostatics and wave forcing in heave, or potential flow models incorporating nonlinear drag, predicted realistic hydrodyanmic loadings in most conditions where radiation damping is negligible. Further, codes that neglected wave-radiation damping predicted significantly different RAOs for the OC3 spar buoy system [14].

Further research needs initiated the OC-project extension into OC4, OC5, and the ongoing OC6. From OC4 to OC6, a semisubmersible foundation (defined in [16]) is studied due to the lack of previous work and studies on this foundation's complex hydrodynamic nature. At the time of OC4, OrcaFlex released an expansion including a turbine model object where a validation report [17] has demonstrated the new extension's capabilities to model the coupled dynamics of FOWTs, and OrcaFlex has since been included from OC4 and ongoing OC6. The OC3 and OC4 illustrated in Figure 1.1 only addressed the differences between the codes where their limitations was further addressed in OC5 [18]. The OC5 project compared numerical and experimental results in both model- and full-scale measurements, and demonstrated that engineering tools predicted the system dynamics and loads relatively well. However, a steady under-prediction of loads and motions in the low-frequency region was observed due to insufficient modelling of nonlinear hydrodynamic excitation forces, which initiated the ongoing OC6 project [19].

Other researchers have also documented the under-prediction of loads and motions of FOWTs in the low-frequency region. For instance, [20] investigated other methods for better predicting response and loads in the low-frequency region using a semisubmersible floater. The authors of this article found that tuning damping coefficients from the response in each irregular sea-state was better than tuning these values from decay tests, which is the method commonly used in the industry. The authors of [21] investigated by comparing numerical and experimental measurements how the inclusion of wind loading on the system, using a semisubmersible model, still resulted in a under-prediction of the response in the low-frequency region. These article demonstrate the further need for research and verification of numerical tools.

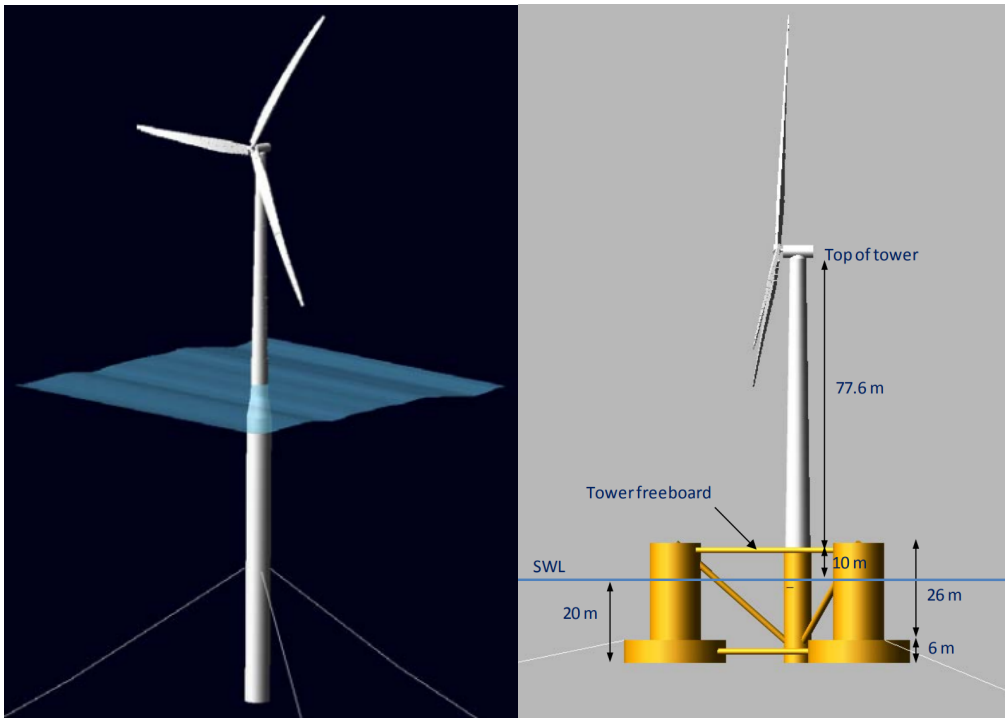

(a) Spar buoy. (b) Semisubmersible.

Figure 1.1: Illustration of two FOWT concepts used in Offshore Code Collaboration (OC3) Phase IV in (a) and Offshore Code Collaboration Continuation (OC4) in (b) from [14; 16]

1.3 Objectives and Thesis Outline

The aim of this thesis is two-fold; firstly, to assess the ability of OrcaFlex for hydrodynamic analysis of mooring systems for floating offshore wind structures, and secondly, to experimentally evaluate whether the extreme response and tensions in the mooring system can be more effectively generated using conditional waves rather than traditional 3-hour irregular sea-states. For experimental validation, a spar-buoy and semisubmersible, both at a 1:100 scale, are tested. Due to time constraints, only the spar-buoy is considered for the numerical work, but it is intended that the approaches explored in this thesis should be general to all substructure types.

The specific objectives of the projects in this thesis are to:

- Conduct experimental tests on two types of foundations for floating offshore wind turbines in model scale in irregular sea-states modelled using JONSWAP and conditional waves to study extreme responses and mooring loads.
- Generate a 3D model of the spar buoy used in experimental tests for time-series analysis in OrcaFlex and compare numerical results to experimental results.

This thesis consists of nine chapters in addition to appendices. Chapter 1 begins with the background, motivation, and previous work related to this project. Chapter 2 introduces relevant theory, with chapters 3 and 4 explaining the experimental and numerical methodology used in this thesis. Following are the results presented in two chapters: Chapter 5 presents results from experimental tests for both foundations in irregular waves modelled using wave spetra. Additionally, numerical results with a spar buoy are compared to experimental results at the end of this chapter. Chapter 6 explains the methods used to generate and calibrate the conditional waves followed by results from time-series analyses using these for both the spar-buoy and semisubmersible. Finally, chapters 7, 8 and 9 finalize this thesis with discussion of the results with concluding remarks and suggestions for further work.

2. Theory

When the responses and loads related to marine structures are studied experimentally or numerically, the ocean environment must be modeled as accurately as possible to represent realistic phenomena. This is due to the importance of capturing effects induced by wave-body interactions needed to be considered in the design of marine structures. As the wave-body interactions are complex, the relevant theory used to describe wave kinematics and how a structure responds in addition to relevant hydrodynamic forces will be described in this chapter.

2.1 Basic Concepts for Wave Theories

Fundamental to all wave theories are the assumptions that water is an incompressible fluid and that the flow of water is continuous. This means the mass is assumed to be preserved. These assumptions give rise to the basic differential equation describing a wave's motion where the conservation of volume is expressed using fluid velocities, as:

$$\frac{\partial u}{\partial x} + \frac{\partial v}{\partial y} + \frac{\partial w}{\partial z} = 0,$$

where u, v and w are the fluid particle velocities placed in a right-handed cartesian system. The positive x-direction is aligned with the direction of the propagating waves, with the positive y-direction pointing upwards, defining a 2-dimensional coordinate system. The z-direction forms the right-handed system following the formulations presented in [22]. The conservation of mass expressed in the forms of the velocity vector gives the continuity equation, well known as:

$$\nabla \cdot \mathbf{V} = 0.$$

A fluid particle's motions are complex where codes based on the Navier-Stokes equations, who describes the motions of viscous fluids [23], result in realistic predictions but are also quite time-consuming. The potential flow theory is a simpler model commonly used in engineering tools for computing wave kinematics. This model assumes that no shear forces are acting on the fluid elements, which supposes that the fluid can be treated as an inviscid fluid. Additionally, assuming the flow is irrotational, a velocity potential function, φ, can be defined. This results in the fluid velocities to be described as the gradient of the velocity potential function, such that:

$$\mathbf{V} = \nabla\varphi.$$

This equation can be substituted for the velocity vector in the continuity equation, which results in the Laplace equation given as:

$$\nabla^2\varphi = \frac{\partial^2\varphi}{\partial x^2} + \frac{\partial^2\varphi}{\partial y^2} + \frac{\partial^2\varphi}{\partial z^2}\,. \tag{2.1}$$

The hydrodynamic loads on a body in water are due to the integration of the pressure of the fluid on the body computed using Bernoulli's equation. This equation is derived from the Navier-Stokes equation under the assumption that the water is an incompressible and inviscid fluid, and the flow of water is irrotational. This results in the unsteady form of the well-known Bernoulli's equation presented here in terms of the fluid particle velocities equal to the formulation used in [24] as:

$$p + \rho\frac{\partial\varphi}{\partial t} + \frac{\rho}{2}\nabla\varphi\cdot\nabla\varphi + \rho g z = c(t). \tag{2.2}$$

This equation includes a hydrostatic term where the only external force acting on the fluid is assumed to be the gravitational acceleration. ρ is related to the density of the fluid, and p is the pressure of the fluid, whereas $c(t)$ is simply an arbitrary function in time. The horizontal acceleration term of the fluid elements is the so-called nonlinear term in the Bernoulli equation. From Eq. 2.2, the only unknown parameter is the velocity potential, which is the fundamental issue in any wave theory to compute the wave kinematics and kinetics. In order to determine the potential function, a set of boundary conditions must be applied. These depend on the wave theory used, where linearization reduces the complexity caused by nonlinearities. The Boundary value problems for developing wave theories in a two-dimensional

case are summarized by [22], as follows:

Bottom Boundary Condition:
The ocean floor at a water depth of, d, is undisturbed and flat where the particle velocity in the y-direction is zero, such that

$$\frac{\partial \varphi}{\partial y} = 0, \qquad \text{at} \quad y = -d. \tag{2.3}$$

The Free Surface Kinematic Condition:
The fluid particle on the free surface continues to stay on the surface, mathematically expressed in forms of the surface elevation, η, as:

$$\frac{\partial \zeta}{\partial t} + \frac{\partial \varphi}{\partial x}\frac{\partial \zeta}{\partial t} - \frac{\partial \varphi}{\partial y} = 0, \qquad \text{at} \quad y = \eta\,. \tag{2.4}$$

Free Surface Dynamic Condition:
The third and final is derived from the Bernoulli equation given in Eq. 2.2, under the assumption that the atmospheric pressure outside the fluid is constant,

$$\frac{\partial \varphi}{\partial t} + \frac{1}{2}\left[\left(\frac{\partial \varphi}{\partial x}\right)^2 + \left(\frac{\partial \varphi}{\partial y}\right)^2\right] + g\eta = 0, \qquad \text{at} \quad y = \eta\,. \tag{2.5}$$

The Laplace equation in Eq. 2.1, and the three boundary conditions stated by Eq. 2.3 - 2.5, must be fulfilled by the velocity potential function in order to solve for the wave kinematics and kinetics.

2.2 Regular Waves

In early stages of the design process, regular waves are often used to study preliminary responses and loads of marine structures. These waves are deterministic wave trains characterized by sinusoidal described by the basic wave parameters illustrated in Figure 2.1. The wave height, H, wave amplitude, A, and wavelength, λ is illustrated in this figure. The wave

period is defined as the time it takes for a wave to travel one wavelength. Other parameters are defined as:

- phase velocity, c, in m/s
- wave frequency, f, in 1/s
- wave frequency, ω, in rad/s
- surface elevation, η, in m

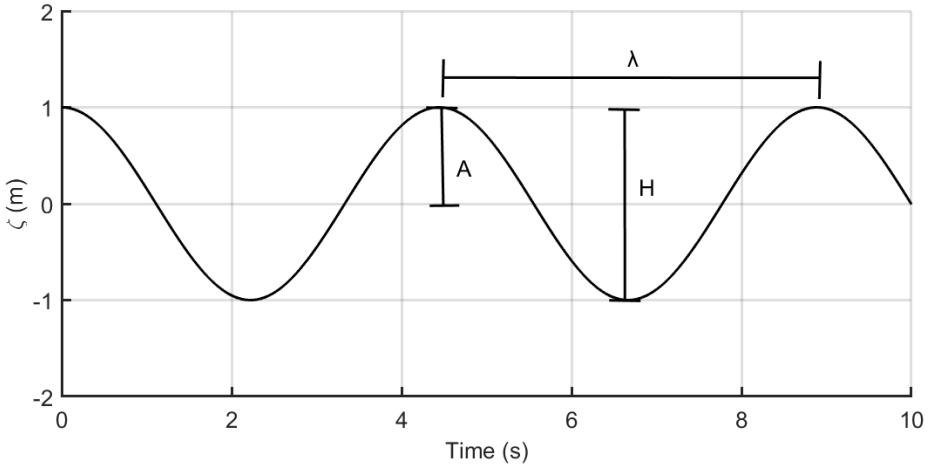

Figure 2.1: Illustration and definitions of basic wave parameters

Numerous wave theories describing the shape of regular waves have been developed over the years and applied to different water depths. Therefore, standard formulations and equations related to regular wave theories in this thesis apply to deep waters.

2.2.1 Linear Airy Wave Theory

The simplest wave theory is the linear Airy wave theory well presented in literature and will therefore not be derived in detail here. To summarize, this theory assumes the wave height, H, is significantly smaller than its wavelength, λ, or water depth. This assumption allows the dynamic boundary conditions given in Eq. 2.5 to be linearized such that the higher order term can be neglected. The Free Surface conditions can also be satisfied at the mean water level instead of the instantaneous surface elevation, which simplifies Eq. 2.4. This results in a combined linearized free-surface condition:

$$\frac{\partial^2 \varphi_1}{\partial t^2} + g\frac{\partial \varphi_1}{\partial y} = 0 \qquad \text{at} \quad y = 0,$$

where the subscript of 1 stands for being the first order solution. The linearized free-surface and bottom boundary conditions are then used to solve the differential equation in Eq. 2.1. For deep water conditions, defined by the deep water criterion: $H/\lambda \geq 0.5$, the first order solution for the potential function in space and time, as given in [25], is finally:

$$\varphi(x, y, z, t) = \frac{g\eta_a}{\omega} e^{kz} \cos(\omega t - kx), \tag{2.6}$$

where ω is the angular wave frequency, g is the gravitational accelerational constant, η_a is the linear wave amplitude, and k is the wave number given by the linear dispersion relation in Eq. 2.8. The surface profile for linear waves in deep water is then given as:

$$\eta(x, y, t) = \eta_a \sin(\omega t - kx). \tag{2.7}$$

By substituting the solution of the potential in the free-surface boundary condition, the dispersion relation relating the wave frequency to the wave number for deep water is:

$$\omega^2 = gk, \tag{2.8}$$

where the wave number also can be computed using the wavelength ($k = 2\pi/\lambda$), where the wavelength is dependent on the wave period, T, related by:

$$\lambda = \frac{gT^2}{2\pi}. \tag{2.9}$$

Linear waves are characterized by a sinusoidal oscillating about MSL where the crests and troughs are equal in magnitude such that the wave height, $H = \eta_a/2$. The linear wave theory applies to waves with a wave height up to the breaking wave limit, called the Stokes criterion, given by:

$$\frac{H}{\lambda} < \frac{1}{7}. \tag{2.10}$$

Waves approaching this limit will result in steeper waves introducing nonlinearities. As a result, the discrepancy between associated predictions using linear theory deviates from reality, and other wave theories of higher orders will be more accurate. A comparison of a linear wave compared to a second-order wave is presented in Figure 2.2. In the following section, nonlinear wave theories are described in more detail.

2.2.2 Second-Order Stokes Wave Theory

Linear wave theory gives a good approximation for waves with small amplitudes, and because of its simplicity, it is commonly used by engineers. However, as waves become steeper, this introduces nonlinearities not predicted by the Airy wave theory. Therefore, higher-order wave theories have been developed to extend the range covered by linear theory to include these. Therefore, the solutions presented by Stokes' higher-order wave theories are not derived using the linearized boundary conditions such as the linear wave theory presented in Section 2.2.1. Instead, the solution to the velocity potential function and surface elevation is for these to be computed through a power series, where the nth order increasingly complicates the mathematical computations. The simplest of Stoke's higher-order theories is the second-order wave theory. Here, the solution is a series of the first- and second-order solutions in terms of the linear wave height, H as stated in [26] and given in Eq. 2.11.

The formulation of the second order wave profile used in this thesis is a combination of the formulation presented in [22] and [24], resulting in:

$$\eta(x,t) = \frac{H}{2}\cos\left(kx - \omega t\right) + \left(\frac{H}{4}\right)^2 k\cos\left[2(kx-\omega t)\right]. \tag{2.11}$$

The higher-order regular wave profiles are characterized by a steeper wave profile with narrower crests with broader and shallower troughs, as illustrated in Figure 2.2. Here, a regular wave with a wave height of $H = 6$ m and a wave period of $T = 9$ s are parameters used as input in Eq. 2.7 and Eq. 2.11. As these formulations are used for deep water conditions, the wave number is computed using the dispersion relation given in Eq. 2.8. The nonlinear effects are associated with the increased asymmetry about the wave crests the nonlinear waves present. Therefore, the highly nonlinear effects occur in large waves as breaking is approached in extreme conditions. While this thesis uses linear wave theory throughout, it also includes nonlinear wave profile definitions and explanations since wave-body interactions in the open sea are prone to nonlinear effects, especially in extreme conditions.

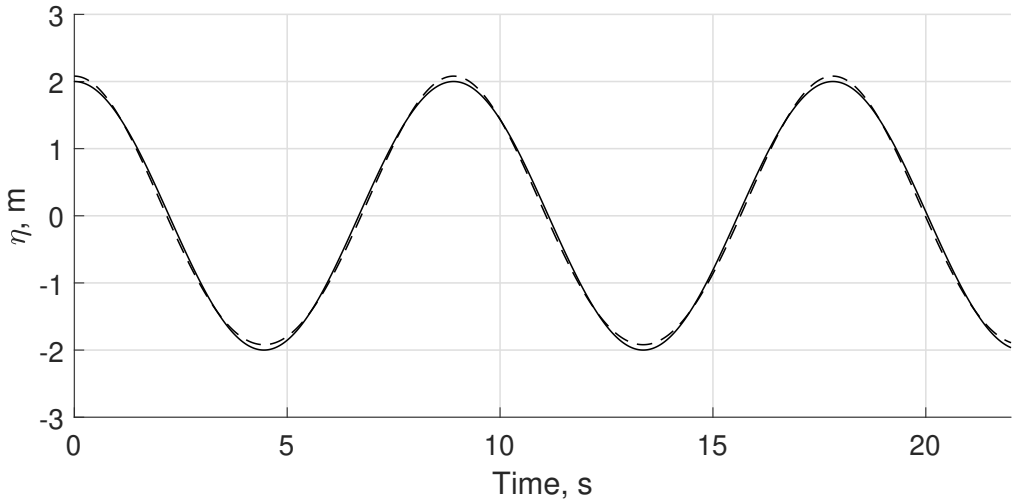

Figure 2.2: A comparison of a regular wave profile modeled using linear wave theory (—), and Stoke's second order wave theory (- - -), for a wave characterized by: $H = 6$ m, and $T = 9$ s.

2.3 Irregular Waves

The previous sections used both linear wave theory and nonlinear wave theory to define regular waves. However, ocean waves are stochastic, so their randomness must be modeled as accurately as possible to capture all effects not accounted for in regular waves.

Irregular sea surfaces are commonly generated through a linear superposition of long-crested regular waves with different amplitudes, frequencies, and phase angles illustrated in Figure 2.3 where the irregular sea surface at the position, x, at the time , t, is well described in the literature as:

$$\eta(x,t) = \sum_{n=1}^{N} \eta_{An} \cos\left(\omega_n t + k_n x + \epsilon_n\right). \tag{2.12}$$

Here η_{An}, ω_n and k_n are respectively the individual wave amplitudes, frequencies, and wave number from linear theory, whereas ϵ is a phase-offset consisting of random values between 0 and 2π.

Irregular waves can be treated by use of statistical theories, and are commonly generated from wave spectra, further explained in the following subsections, hence the wave amplitudes η_{An} are computed from the wave spectrum, $S(\omega)$, as:

$$\eta_{An} = \sqrt{2S(\omega)\triangle\omega}\,. \tag{2.13}$$

Over the next subsections, relevant theory to irregular seas are further explained in line with relevant equations for irregular wave tests.

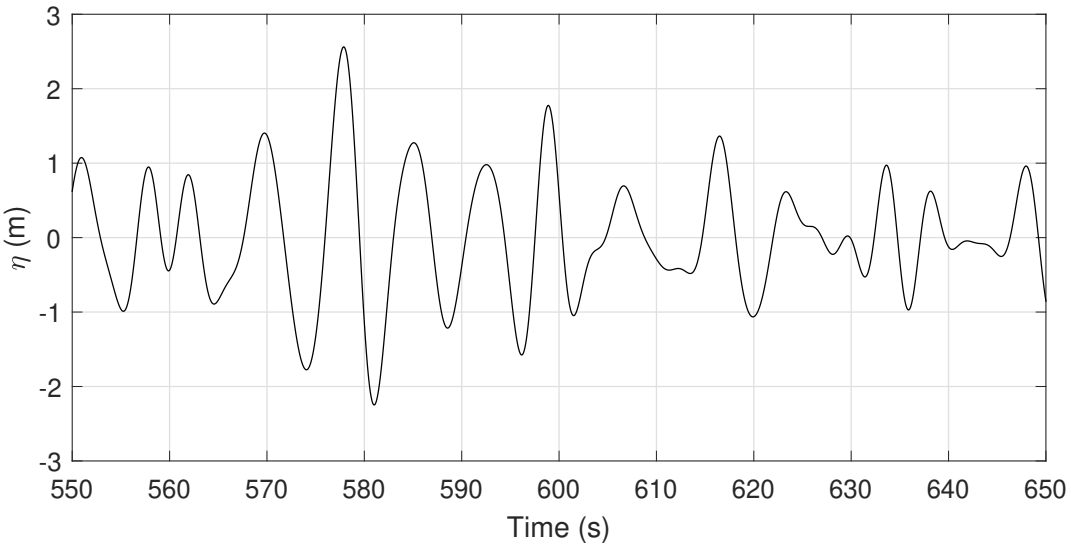

Figure 2.3: Illustration of an irregular wave time series.

2.3.1 Wave Spectra

A standard approach in modeling irregular seas, both experimentally and numerically, is utilizing standard wave spectra for a given area of interest. Multiple wave spectra types exist, all of which measure the energy distribution of individual wave frequencies for a given location. These are standardized mathematical spectral models for different geographical areas and characterize the wave climate for a short-term period, called sea-states. A sea-state is a sea climate typically limited to 3 hours described using one or more wave parameters such as the significant wave height, H_s, and the spectral peak period, T_p [26].

One of the most widely used wave models is the JONSWAP spectrum which is applicable for fetch-limited and developing sea states. This spectrum was established by the authors of [27] and developed from measurements of the wave climate in the North Sea's southeast part on shallow water. Using the formulation from [28] where $\omega_p = 2\pi/T_p$, the JONSWAP spectrum is generated according to:

$$S_J(\omega) = A_\gamma \frac{5}{16} H_s^2 \omega_p^4 \omega^{-5} \exp\left(-\frac{5}{4}\left(\frac{\omega_p}{\omega}\right)^4\right) \gamma^{\exp\left(-0.5\left(\frac{\omega-\omega_p}{\sigma\,\omega_p}\right)^2\right)} \tag{2.14}$$

where:

σ = spectral width parameter with values:

$\sigma_a = 0.07$ for $\omega \leq \omega_p$

$\sigma_b = 0.09$ for $\omega > \omega_p$, and

A_γ = $1 - 0.287\ln(\gamma)$ is a normalizing factor.

The values presented here for the non-dimensional peakedness parameter, γ, and the spectral width parameter, σ, are mean values stated by [27] and are commonly considered and used as constants. Therefore, in this thesis, they are also considered constants.

The JONSWAP spectra are a modification of the Pierson and Moskowitz (P-M) spectrum formulated in 1964 for fully developed seas and reduced to a P-M spectrum for $\gamma = 1$ as seen in Eq. 2.14. In Figure 2.4, the two-wave spectrum is compared with the JONSWAP spectrum using γ= 3.3. The peakedness parameter is a measure of how energy is distributed over the wave spectrum. A higher peakedness parameter results in a narrower spectrum where most wave energy is centered around the peak frequency. A narrow wave spectrum characterizes developing seas compared to a fully developed sea spectrum, as shown in Figure 2.4, where the same wave parameters are used in a P-M and JONSWAP spectrum. The two-wave spectra yield the same energy content with a different energy distribution where the JONSWAP spectrum contains more wave energy over frequencies around the peak frequency.

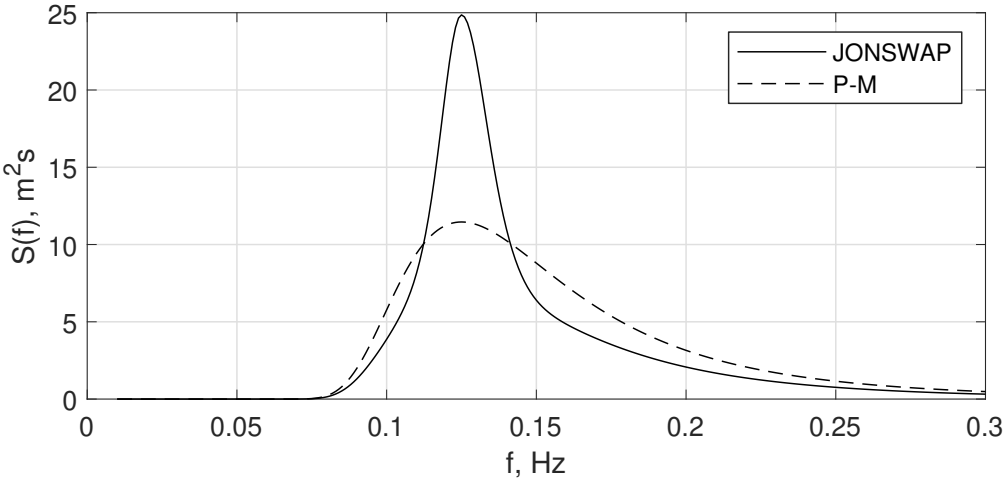

Figure 2.4: A comparison of a JONSWAP and Pierson and Moskowitz (P-M) wave spectrum both defined by H_s=4 m, and T_p=8 s.

2.3.2 Spectral Analysis

Sea states consist of waves with different frequencies. Therefore, when analyzing these, it is often convenient to transform the results from the time domain to the frequency domain, called spectral analysis. Here, the spectral density functions of the recorded time series are computed. These are usually obtained by taking the Fast Fourier Transformation (FFT) of either the autocorrelation function or the cross-correlation function [25].

The autocorrelation function, $R_{xx}(\tau)$ describes the correlation between a stochastic process, x, at time t compared to the time series at a time shift $t + \tau$, dependent on the time lag τ, formulated as follow:

$$R_{xx}(\tau) = \lim_{T\to\infty} \frac{1}{T} \int_0^T x(t)x(t+\tau)\, dt. \tag{2.15}$$

Using the assumption that the recordings take place over a time interval ($0<t<T, T \to \infty$), the power spectrum, $S_{xx}(\omega)$, of the time wave signal, can be obtained by taking an FFT transform of the autocorrelation function, $R_{xx}(\tau)$, as follows:

$$S_{xx}(\omega) = \int_{-\infty}^{\infty} R_{xx}(\tau)e^{-i\omega\tau}\, d\tau. \tag{2.16}$$

As the autocorrelation function of a sinusoidal is a cosine function with the same frequency, meaning the phase information is lost [29], the cross-correlation function correlates two different signals such that the phase between the two is considered. For instance, using the wave input, $x(t)$, as a reference with $y(t)$ as the measured response, the cross-correlation function is given in the form:

$$R_{xy}(\tau) = \lim_{T\to\infty} \frac{1}{T} \int_0^T x(t)y(t+\tau)\, dt. \tag{2.17}$$

Taking the FFT of the cross-correlation function between the input wave and the recorded response of the structure, the cross-spectrum can be obtained by:

$$S_{xy}(\omega) = \int_{-\infty}^{\infty} R_{xy}(\tau)e^{-i\omega\tau}\, d\tau. \tag{2.18}$$

A complex linear transfer function is simply defined as the ratio between the response spectrum, $S_{xy}(\omega)$, and the input wave spectrum, $S_{xx}(\omega)$, as:

$$H(\omega) = \frac{S_{xy}(\omega)}{S_{xx}(\omega)}\,, \tag{2.19}$$

and the relative phase between the response and incident wave is computed from the complex transfer function by:

$$\phi = \arctan\left(\frac{a}{b}\right), \tag{2.20}$$

where a and b are the real and imaginary parts of the linear transfer function $H(\omega)$ in Eq. 2.19.

2.3.3 Response Amplitude Operator

The Response Amplitude Operator (RAO) is commonly used to describe a marine structure's motion amplitude in incident waves for a given wave frequency. The RAO curves can be computed by taking the modulus of the transfer function in Eq. 2.19, meaning:

$$RAO = |H(\omega)|, \tag{2.21}$$

or the RAO-curves can be computed from the input wave spectrum, S_{xx}, and measured response spectrum, S_{yy}, as:

$$RAO = \sqrt{|H(\omega)|^2} = \sqrt{\frac{S_{yy}}{S_{xx}}}\,. \tag{2.22}$$

In the last formulation, the RAO is computed from the ratio between the power spectrums computed using Eq. 2.16 which is based on the autocorrelation function. This means the relative phase between the incident wave and the structure's response is lost in the transformation, and the motion amplitude is the sole information obtained.

2.3.4 Short-term Sea State Statistics

A sea state is an ocean climate limited to a short period and treated as a random process. Common assumptions in describing the short-term statistics are the sea surface being a stationary and an ergodic process. Therefore the wave statistics are assumed to be constant during the time considered, and a single event at a random time can be used to characterize the entire sea state. In addition, the sea surface is assumed to follow a gaussian distribution with zero means, whereas the individual waves are commonly assumed to follow a Rayleigh

distribution with a non-zero mean.

For a short-term design, it is often necessary to calculate the extreme loads and response statistics during a short-term storm condition. The focus is, therefore, on the distribution of extreme values of a stationary Gaussian process, which is specified by an appropriate wave spectrum that characterizes a short-term wave condition. If the wave spectrum is known, the statistical quantities can be computed in the frequency domain using the nth spectral moments of the spectrum, $S(\omega)$, given in [30] as:

$$m_n = \int_0^\infty \omega^n S(\omega)\, d\omega. \tag{2.23}$$

The relationship between the wave spectrum formulated using the angular frequency, ω, and the wave frequency, f, is obtained from: $S(f) = 2\pi S(\omega)$. The spectral moments from Eq. 2.23 are used to compute several describing wave parameters, where only a few are selected and presented here.

The significant wave height is the most common parameter used to describe ocean statistics and is defined as the average of 1/3 of the highest waves in a sea state. Using a wave spectrum, this parameter is related to the variance of the spectrum and can be computed by the zeroth-moment commonly known as:

$$H_s = 4\sqrt{m_0}\,. \tag{2.24}$$

The average of the 1/10 highest waves in a given sea state is also a quantity commonly used, and the relation used in this thesis is the formulation given by [22] as:

$$H_{1/10} = 5.091\sqrt{m_0}\,. \tag{2.25}$$

The average wave period between the given waves is estimated using the zeroth and first spectral moments:

$$T_1 = T_{m01} = \frac{m_0}{m_1}. \tag{2.26}$$

Theoretical maximum wave height in a wave record can be estimated using the formulation presented by Longuet-Higgins in [31] as:

$$H_{max} = H_s\sqrt{\frac{ln(N)}{2}}. \tag{2.27}$$

Here, the maximum wave height is sensitive to the number of waves, N, in the sea state. In the frequency domain, the total number of waves can be determined using the duration of the sea state in seconds, D, and mean period T_1, as follows:

$$N = \frac{D}{T_1}. \tag{2.28}$$

The same formulations for computing wave statistics presented in this section can also be used for estimating extreme response statistics. This is because the surface elevation follows a Gaussian process, meaning the response process in this sea state is assumed to follow the same distribution. This extends to other statistics assuming the process follows a Gaussian distribution where the individual sinusoidal waves follow a Rayleigh distribution.

2.4 Most Likely Wave (MLW)

In the previous sections, theories regarding regular and irregular waves have been presented. An alternative wave theory is the NewWave model developed by Tromans in 1991 in [32]. This wave model consists solely of a deterministic wave group focused on position and time by aligning the phases of the standard wave components in a random sea state. The NewWave theory has been shown to provide a realistic deterministic alternative to regular wave theories. However, when used as a time history for analyzing dynamically sensitive structures, such as wind turbines, NewWave's single profile does not account for the randomness of the sea and, therefore, not the effect this randomness has on the structure's dynamic response [33]. By embedding a NewWave in a random background sea, this wave profile can be used to produce a time series of a random surface elevation with an extreme event constrained to a specific time [34].

A model using a focused wave embedded in a random sea is the Most Likely Wave model used in Dietz [33]. The formulations used in this thesis to derive the Most Likely Wave pro-

file is by using the NewWave definition from Tromans in [32] embedded in a random sea using methods presented in Dietz in [33]. This method is complemented by formulations presented in [35] and [34].

The NewWave profile presented by Tromans in 1991 is formulated using the autocorrelation function multiplied with a scalar, a. The NewWave autocorrelation function in the MLW profile is derived from the wave spectrum used to model the random background sea. Therefore, the autocorrelation function used to define the focused wave profile is computed by taking the inverse FFT of the wave spectrum. This results in the autocorrelation (here: $\rho(x,t)$), presented on discrete form as in [35], given by:

$$\rho(x,t) = \frac{\alpha}{\sigma^2} \sum_{n=1}^{N} \sigma^2 \cos\left(k_n x - \omega_n t\right). \tag{2.29}$$

The variance, σ^2, is computed from the wave spectrum; either as a summation of the individual wave spectrum amplitudes squared and divided by two or using the relation between the individual wave amplitudes and the wave spectrum in Eq. 2.13, equivalent to:

$$\sigma^2 = \sum_{n=1}^{N} \frac{\eta_{An}^2}{2} = \sum_{n=1}^{N} S(\omega_n) \triangle\omega. \tag{2.30}$$

The scale factor, a, determines the amplitude of the focused wave and is computed here using the theoretical maximum wave height given by Eq. 2.27, where $a = H_{max}/2$. The focused wave can also be constrained to a focal position (x_{foc}), and a focal time (t_{foc}) by replacing the variables: $x = x - x_{foc}$ and $t = t - t_{foc}$ in the NewWave autocorrelation function in Eq. 2.29.

Assuming the random sea surface has a surface elevation a_{foc} and slope $\dot{a}_{foc}$ at time t_{foc}, the realization of the MLW profile, as formulated by the authors of [35], and [33], is given as:

$$\eta_{MLW}(x,t) = \eta(x,t) - a_0\rho(x,t) - \dot{a}\dot{\rho}(x,t) + a\rho(x,t). \tag{2.31}$$

Here, the random background sea, $\eta(x,t)$, is modeled using Eq. 2.12. This methodology subtracts the random surface elevation at the focal time before the NewWave realization ($a\rho(x,t)$) is added back to the modified wave profile creating a focused wave in a random

sea state. These waves allow for easy and efficient computation of an extreme event which can be used to evaluate extreme response statistics. This is under the assumption that the extreme response is related to the occurrence of an extreme wave within the stochastic sea state.

2.5 Most Likely Response Wave (MLRW) and Conditional Random Response Wave (CRRW)

For dynamically responding structures, extreme response and mooring loads do not always result from extreme wave heights and may result from a combination of local extreme waves with an unfavorable background sea due to structural memory effects, as stated by Dietz in [33]. Compared to the NewWave theory by [32], and MLW from Section 2.4, a different wave model described by [33], called Most Likely Response Wave (MLRW), is a wave group conditioned on the marine structure's characteristics. This deterministic wave model is conditioned on a response amplitude, a, and the instantaneous response frequency, ω, of the structure's linear response to account for structural memory effects and used to model a critical wave episode for a ship in [33].

The process used to model the MLRW in this thesis uses the formulations given by Dietz in [33]. In Dietz's Ph.D. thesis, the wave model is modeled as a vector process meaning its definition is formulated using a set of random constrained coefficient vectors ($\overline{V}_{c,n}, \overline{W}_{c,n}$). These are computed using the spectral moments of a chosen sea-state (m_0, m_1, m_2), the structure's transfer function, $H(\omega)_n$, and its associated phase angles, $\theta^e_{\eta,n}$,in:

$$\overline{V}_{c,n} = \frac{a^e_{\eta,n}}{m_0 m_2 - m_1^2} \cdot \left[a_\eta(\omega_{e,n} m_1 - m_2) \cos\left(\theta^e_{\eta,n}\right) - a_\eta \overline{\omega}_\eta (\omega_{e,n} m_0 - m_1) \cos\left(\theta^e_{\eta,n}\right) \right] \quad (2.32)$$

and,

$$\overline{W}_{c,n} = \frac{a^e_{\eta,n}}{m_0 m_2 - m_1^2} \cdot \left[a_\eta(\omega_{e,n} m_1 - m_2) \sin\left(\theta^e_{\eta,n}\right) - a_\eta \overline{\omega}_\eta (\omega_{e,n} m_0 - m_1) \sin\left(\theta^e_{\eta,n}\right) \right], \quad (2.33)$$

where the linear response amplitude, a_η is an input value of the extreme response amplitude wished to achieve, and the mean response frequency is determined from the spectral mo-

ments: $\overline{\omega}_\eta = \frac{m_1}{m_0}$. The MLRW is conditioned on the linear response of the structure where the coefficient $a^e_{\eta,n}$ is determined using the wave spectrum, $S(\omega_n)$, and the structure's transfer function, given as:

$$a^e_{\eta,n} = H(\omega_n)_{\eta,n} \sqrt{S\left(\omega_n\right) \Delta_n}\,. \tag{2.34}$$

Finally, the MLRW surface using the vector-process formulation as a function of position, x, and time, t, is given by:

$$\eta_{MLRW}\left(x,t\right) = \sum_{n=1}^{N} a^e_{\zeta,n} \left[\overline{V}_{c,n} \cos\left(k_{e,n}x - \omega_{e,n}t\right) \; + \; \overline{W}_{c,n} \sin\left(k_{e,n}x - \omega_{e,n}t\right)\right] \tag{2.35}$$

where the wave number, $k_{e,n}$ is formulated using the dispersion relation for deep water from linear wave theory given in section 2.2.1, ω_n is the wave frequency, and the coefficients, $a^e_{\zeta,n}$, are computed from the wave spectrum:

$$a^e_{\zeta,n} = \sqrt{S\left(\omega_n\right) \Delta_n}\,. \tag{2.36}$$

MLRW embedded in a random background sea is called a Conditional Random Response Wave (CRRW). This wave definition is computed by adding the wave amplitudes of a given random background sea, $\eta(x,t)$, and MLRW surface elevations, η_{MLRW}, such as:

$$\eta_{CRRW}\left(x,t\right) = \eta(x,t) + \eta_{MLRW}(x,t). \tag{2.37}$$

The purpose of this model is to accurately predict short-term statistics in a more time-efficient way than using a single full three-hour sea-state or multiple short-term sea states in a brute force simulation in which both are significantly more time demanding.

2.6 Response of Floating Marine Structures

When a marine structure is exposed to waves, it responds as a rigid body in six degrees of freedom (DOF): surge, sway, heave, roll, pitch and yaw. These are three displacement modes and three rotational modes defined in a cartesian coordinate system using a right-hand rule as illustrated in Figure 2.5.

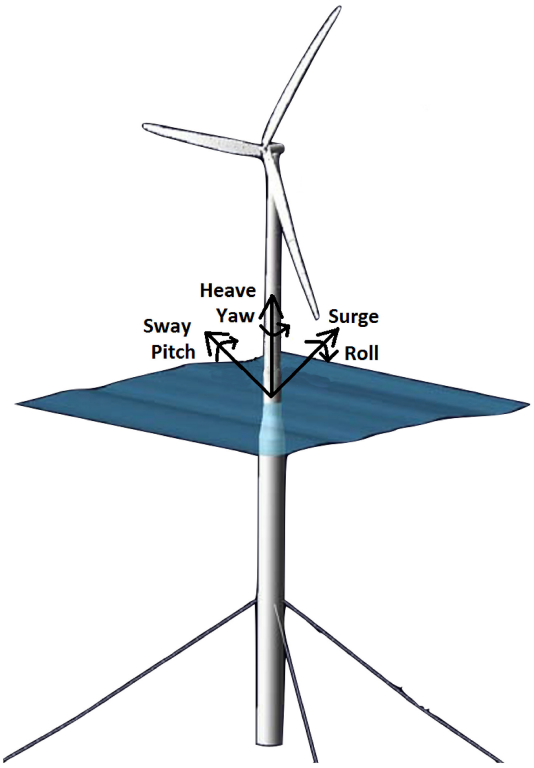

Figure 2.5: Illustration of the six degrees of freedom (DOF) for a rigid body in waves [36]

2.7 Equation of Motion

The equation of motion describes how a marine structure responds to incident waves. This equation is a force equilibrium between the inertia, damping, and restoring forces resisting the excitation forces and moments arising from the wave-body interactions. By using linear and angular momentum from Newton's 3rd law or the Principle of Virtual Work in Lagrangian dynamics, the formulation presented in this thesis is in the form from [23] where the force equilibrium in terms of the n,j degrees of freedom is given as:

$$\sum_{n=1}^{6}[(M_{n,j}+A_{n,j})\ddot{x}_n + B_{n,j}\dot{x}_n + C_{n,j}x_n] = F_j e^{-i\omega_e t} \qquad (j=1,2,...,6). \tag{2.38}$$

Here,

- $\ddot{x}$, $\dot{x}$ and x is the acceleration, velocity and displacement of the marine structure in its n degree of freedom,
- $M_{n,j}$ and $A_{n,j}$ are the components of the mass and added mass matrix of the structure,
- $B_{n,j}$ and $C_{n,j}$ are the component of the damping and restoring matrix, and

- F_j^{exc} are the complex amplitudes of the total excitation forces acting on the body in the jth degree of freedom.

2.7.1 First-Order Wave Excitation Forces

The total excitation forces on a submerged structure in waves arise from the pressure distribution on the body's wetted surface [23]. These contributions result from the fluid motion without the presence of a body (incident), pressures from the body disturbing the wave field (scattered), and radiated waves generated by the oscillating body affecting the local wave field summarized in Eq. 2.39 from [37] as:

$$F^{exc}(t) = F_I + F_S + F_R. \tag{2.39}$$

Here F_i is the forces due to the incident waves (Froude-Krylov force), F_S scattered waves, and F_R arise from radiated waves. The linear first-order forces are computed assuming the free surface condition can be satisfied at the mean water level.

When a structure's size is sufficiently large, it disturbs the free surface by generating and reflecting (radiating) waves in each degree of freedom, in addition to local disturbances due to the body (wave diffraction). These disturbances change the pressure on the submerged structure, and therefore the forces on the structure vary with these effects [25]. A limit for when the diffraction forces are significant is when the ratio between the wavelength and diameter (λ/D) is greater than five, and the flow around the structure is assumed to remain attached. Then the flow can be well predicted by the potential flow theory and is commonly used in the boundary element method (BEM) [37] and is the method used in several commercial codes. This technique's essential is describing the structure's geometry using panels. The local coordinates of its corners describe each panel on the structure surface. Due to complex flow around small structures and the formation of vortices in their surroundings, it is difficult to compute these pressure distributions, thus the need for Morison's empirical equation, further discussed in Section 2.8.

The total wave-field is made up of radiated, incident, and diffracted waves. The linear potential flow theory allows for a separate solution of the individual potential functions, referred

to as the principle of superposition. Therefore, the total potential function is given as a summation of each contribution in [23]:

$$\varphi = \varphi_0 + \varphi_7 \sum_{j=1}^{6} \varphi_j. \tag{2.40}$$

Here φ_0 is the incident wave potential, φ_7 is the diffraction velocity potential, and φ_j is the radiation potential for the jt degree of freedom. These velocity potentials satisfy the Laplace equation and the linearized versions of the boundary conditions in Section 2.1. The incident potential (from Froude-Krylov) is assumed to be known from the linear wave solution. Once the diffraction potentials are known, the linear dynamic pressure can be determined by Bernoulli's equation (Eq. 2.2), and the wave excitation force in the jth degree of freedom can be computed by multiplying the dynamic pressure with the body average of the jth degree of freedom and then integrating over the mean wetted body surface, S_0 [23] by:

$$F_j^{exc} = \rho \int_{S_0} \frac{\partial \varphi_0}{\partial t} n_j \, dS + \rho \int_{S_0} \frac{\partial \varphi_7}{\partial t} n_j \, dS. \tag{2.41}$$

The solution consists of the Froude-Krylov force, and the diffraction forces added, forming the total linear excitation wave forces in the equation of motion in Section 2.7.

2.7.2 Free Oscillation

When the applied forces to the marine system are removed, the equation of motion can be solved as a homogeneous equation as derived in [23]. In waves, a rigid body acts like a harmonic oscillator. Under the assumption that marine systems are sub-critically damped systems, meaning the damping ratio is $\zeta << 1$, the damped natural frequency, ω_d, can be derived from:

$$\omega_d = \omega_0 \sqrt{1 - \zeta^2}\,, \tag{2.42}$$

where ζ is the damping ratio between the damping and critical damping coefficient. ω_0 is the systems undamped natural frequency depending on the stiffness and total mass in the following relation:

$$\omega_0 = \sqrt{\frac{k}{m}}. \tag{2.43}$$

From the general solution of Eq. 2.38, the damped motions can be described by an exponential sinusoidal decay curve on the form:

$$y_n = A \sin\left(\sqrt{1-\zeta^2}\,\omega_0 t + \phi\right)\, e^{-\zeta\omega_0 t} \tag{2.44}$$

where A is the initial amplitude of the oscillations, ϕ is a random phase shift, and ω_0 is the undamped natural angular frequency defined as $\omega_0 = 2\pi f_0$, with f_0 being the undamped eigenfrequency. The decaying rate is dependent on the damping coefficient, n, computed using:

$$n = -\zeta\omega_0 t\ . \tag{2.45}$$

2.8 Morison's Equation

Previously mentioned in Section 2.1 the assumptions used for the potential flow theory neglect viscous effect, which is an essential part of damping [25]. Therefore, commonly used in numerical tools is to include viscous effect by incorporating Morison's equation by [38] for calculating hydrodynamic loads on fixed slender circular structures exposed to oscillating flow [24]. As OrcaFlex is the numerical code used in this thesis, the extended form of Morison's equation used in their computations for a moving body is formulated in [39] as:

$$F = (\Delta a_f - C_a \Delta a_b) + \frac{1}{2}\rho C_d A |v_r| v_r, \tag{2.46}$$

where C_a is the added mass coefficient for the body, a_f, and a_b are respectively the fluid and body acceleration relative to earth. Similarly, v_f and v_r are the fluid velocities relative to the earth and the body. The added mass component results from the body disturbing the local fluid flow. As explained in Section 2.7.1, the Froude-Krylov arises from the acceleration of the fluid without the disturbances of the presence of a body. The added mass coefficient is taken as $C_m = 1 + C_a$ and is therefore not included in the formulation.

Morison's equation is well-known to be applicable when the diffraction parameter (=π D/λ) is less than 0.5 computed using the diameter, D, and wavelength, λ. This is when the potential flow assumptions are less valid as the flow starts to separate from the structure's surface

and viscous effects are assumed to contribute significantly [37].

2.9 Mooring Line Forces

Floating wind turbines are positioned using mooring lines in different materials and formations depending on the water depth and platform type [40]. The combined system characteristics of a marine structure, and its positioning system combined, are also influenced by the effect the mooring lines have on the floater's response. Therefore, mooring lines are mounted with a pre-tension value such that the total forces arising in moorings will be the pre-tension force and the dynamic force combined, such that the total mooring line force, as given by [41], is:

$$F_{mooring} = F_{static} + F_{dynamic}. \tag{2.47}$$

The mooring line configuration used in this thesis both experimentally and numerically is a slack mooring line configuration mounted above the water level in a horizontal direction. Therefore, the mass and damping of the material are assumed negligible such that the mooring line forces arising due to the FOWTs motion in incident waves can be computed considering a linear relation between the mooring line stiffness, k, and the displacement length, x, as:

$$F_{mooring} = kx. \tag{2.48}$$

When the mooring lines are mounted at an angle, α, relative to the direction of the incoming waves, the horizontal force can be computed utilizing trigonometric identities, as given in [22]:

$$F_x = F_{mooring} \cos(\alpha). \tag{2.49}$$

A particular load to which FOWT's moorings are vulnerable is a sudden extreme tension spike in the mooring line tensions called a snap load. These are defined as a spike in tension when the mooring lines re-engage after a slack event. A criterion used in the definition of a snap load is the one suggested by the authors of [42]:

$$F_{dynamic} \leq 0.9 \cdot F_{static}\,. \tag{2.50}$$

This criterion is revised from [41] under the assumption that this criteria can be generalized to apply for snap loads in moorings for FOWTs, and is also the criteria used in this thesis.

3. Experimental Methodology

3.1 Test facility

The experimental tests in this thesis are conducted in MarinLab, a hydrodynamic research facility located at the Western University of Applied Sciences (HVL's) campus in Bergen. MarinLab is a 50x3x2.2 m water tank equipped with an Edinburgh Designs towing carriage and six flap-type wave paddles with force-feedback control in addition to a Qualysis motion-capture system with four cameras installed above the tank. The force-feedback controller allows a stable wave generation to be maintained throughout the experiments. This controller measures the forces on the front of the paddle to modify the paddle motion accordingly and prevent cross-waves from being generated as a result of reflections in the tank [43]. The individual wave paddles are 0.5 m wide and capable of generating regular waves with a maximum wave height of 0.5 m at a corresponding wave period close to 2 s ($\approx$1.9 s). The wavemaker can also generate different irregular sea states described by wave spectrums.

At the opposite end of the wavemaker is a beach made of perforated steel plates. These plates are designed with an exponential profile to be asymptotically 8° to allow for waves to be absorbed and not reflected into the tank. This prevents reflected waves from interfering with incoming waves generated by the wavemaker.

3.2 Model Descriptions

There are two different floating foundations for offshore wind turbines studied in this thesis: 1) spar-buoy and 2) semisubmersible. The experiments are carried out on a 1:100 model scale with a full-scale water depth of 220 meters scaled using Froude's geometrical similarity [44]. The semisubmersible is currently under a confidential agreement with a company that

remains anonymous for this publication. The experimental setup will, therefore, only be described in detail for the spar-buoy as limited information can be presented in this thesis regarding the semisubmersible.

3.2.1 Spar buoy

This model is a deep draft floater previously used in experiments at HVLs MarinLab. It is an old design such that the information about its full-scale version is limited. Therefore, the model's main dimensions are measured and presented in Figure 3.1. Its main characteristics are presented in Table 3.1 with estimated full scale dimensions. This model is designed with damping plates with an equivalent diameter of 20.3 m and a thickness of 1.2 m, included in the same figure.

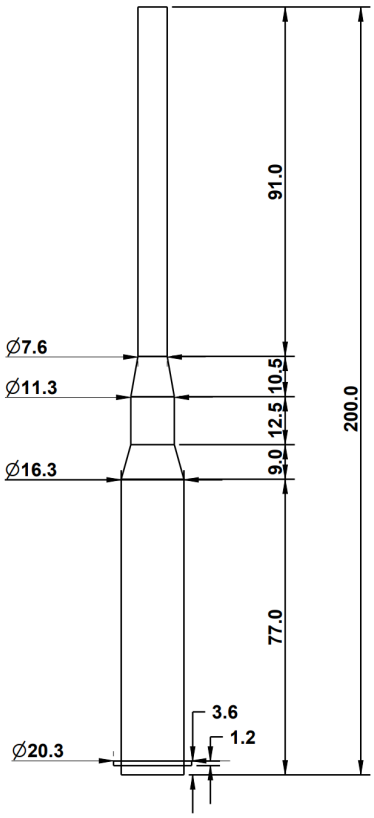

Figure 3.1: Measured dimension of the spar-buoy in full-scale dimensions given in meters.

.

The model's center of gravity is determined using a Bifilar suspension method following the procedure presented in [45]. This method uses the model's equilibrium position when

hanging freely to determine its CoG. The model is therefore lifted from the ground using two ropes, and a position on the model placed directly 90 degrees below the hinged position is marked. The model is then flipped, where the same procedure is used to mark a second position on the model. The point where the two lines intersect is the estimated position of its center of gravity using this method. An illustration of this method is sketched in Figure 3.2.

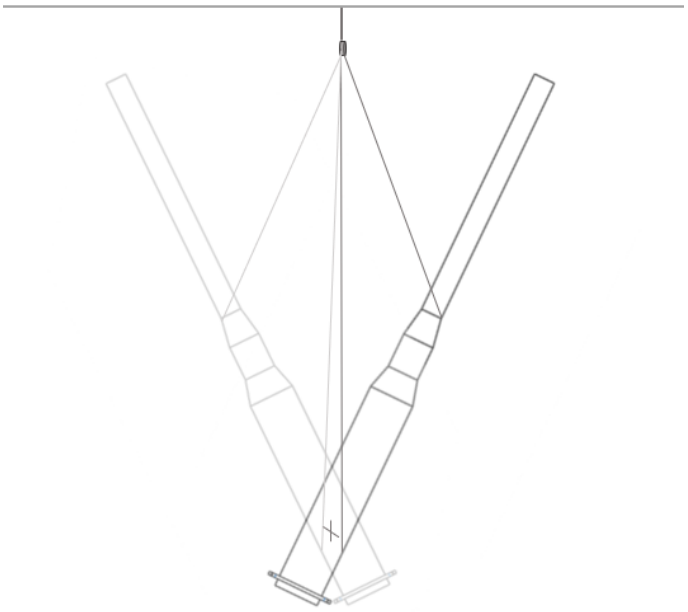

Figure 3.2: Sketch of the Bifilar suspension method used to estimate the location of the spar buoy's center of gravity without the top mass included.

The top mass was not included in this setup as this was performed earlier than the experimental tests conducted in this thesis. Therefore, the Bifilar's suspension method was performed without the top mass as this weight depends on the additional equipment and apparatus used in the experimental tests. Therefore, the CoG of the entire model with the additional weight of the equipment is computed using the center of mass formulation under the assumption that the spar-buoy is homogeneous such that the center of mass coincides with the center of gravity. Both the model's top mass and mass are considered point masses, m, at a vertical distance, z from the baseline. Then the center of gravity is determined from this equation [46]:

$$z_{COG} = \frac{m_1 z_1 + m_2 z_2}{m_{tot}} \, .$$

The estimated position of the center of gravity is included in Table 3.1 with the spar buoys' main dimensions and parameters. The position of CoG is used for defining the local coor-

dinate system in Qualysis and the diffraction analysis of the full-scale version of the buoy described in Chapter 4.

The Bifilar's suspension method can be extended to calculate the gyration radii if using a pendulum, but this requires a different setup, including a second Qualisys camera, unless the model was suspended over the tank where the camera system is already placed. These are both complicated procedures in which the safety of the latter method is questionable. Therefore this test was not conducted.

Table 3.1: Structural properties of the spar-buoy in full and model scales

Parameter, unit	**Model scale**	**Full scale**
Total Mass, Kg	18.1237	18,123,700
Mass RNA, Kg	0.9898	989,800
Mass tower+platform, Kg	17.1339	17,133,900
Draft, m	0.90	90.0
Center of Gravity, m	[0, 0, 0.35]	[0, 0, 35]

3.2.2 Semisubmersible

The floating semisubmersible wind turbine foundation model is a three-column stabilized foundation, common to several designs already used commercially. As several features of this specific design have yet to be patented, it will be treated confidentially were the only dimensions and parameters made publicly available are summarized in Table 3.2.

Table 3.2: Overview over publishable data of the semisubmersible floating wind turbine foundation used in the wave tank tests given in full-scale valus.

Parameter, unit	**Value**
Length between columns, m	90
Column height, m	40
Column outer diameter, m	12

3.3 Experimental Set-Up and Measurement Apparatus

The spar-buoy and semisubmersible are moored using a light mooring system consisting of three mooring lines. These lines are connected to the bodies at MSL and mounted to an individual load cell with a capacity of 30 N. Two load cells are placed along the tank walls, and one is placed in line with the incoming waves, as illustrated in Figure 3.3. The stiffness in the system is introduced by linear springs where a total of five springs have been connected in series in each line for the spar-buoy. This number is determined by the springs' ability to be stretched 10 cm without being plastically deformed, thus introducing nonlinearities into the system. For simplicity, the mass is assumed to be massless and the stiffness linear.

The mooring line stiffnesses are calculated using Hooke's law, assuming a linear relation between the change in displacement and change in force: $k = \triangle F / \triangle x$. F equals the mass multiplied by the gravitational acceleration, and x is the displacement. The exact weights are used for all three lines: 0.05 Kg and 0.1 Kg, and the resulting mooring line stiffness and the individual mooring line lengths are given in Table 3.3. Since the load cells along the tank walls are placed at different distances from the tank walls due to the ramp for the towing carriage, the length of mooring lines 2 and 3 differ slightly. The measured mooring line angles are also included in Figure 3.3. The FOWT's response in different sea states is recorded via Qualisys camera system. Reflective balls are mounted at different locations on the model to track the floater's response accurately. The responses are measured relative to a local coordinate system defined by the user, in this case, at CoG.

Table 3.3: Measured mooring line stiffness and individual mooring line lengths.

Line nr.	**Stiffness, k [N/m]**	**Length, l [cm]**
Line 1	8.04	162
Line 2	8.76	205
Line 3	8.18	200

Wave elevations are measured using six resistance-type wave gauges. These are placed at different locations to measure the changes in wave characteristics due to the various wave components traveling at different speeds. One wave gauge is placed 10 meters from the wave

paddles and 8.5 meters from the model to measure the undisturbed wave elevations. At this distance from the model, the disturbance in the wave field due to radiated and diffracted waves are noted to be very small, according to the authors of [47]. The digital wave gauges record data at a sampling rate of 128 Hz and are downsampled to Qualisys' sampling frequency in post-processing.

The experimental set-up is displayed in Figure 3.3 and illustrates the locations of the measurement apparatus relative to the model's position. The exact positions of the wave gauges relative to the model's center at resting position, and wave paddles, are given in Table 3.4. The distances between wave gauges 2-6 are picked from Øen's arrangement in [48]. Here the wave gauges are related to wave gauge 4, which is placed at the model's center at the resting position. The model's center is located in the middle of the tank (1.5 m from either tank wall) and 18.5 m from the wave paddles due to the position of the Qualisys camera system. An illustration of the full setup in MarinLab is presented in Figure 3.4.

Table 3.4: Location of wave gauges (WG) respective to wave paddles ($x_{paddles}$), and the center of the spar-buoy's resting position (x_{model}) given in meters.

WG #	**1**	**2**	**3**	**4**	**5**	**6**
$x_{paddles}$ [m]	10.0	17.03	17.58	18.5	19.05	19.78
x_{model} [m]	-8.5	-1.47	-0.92	0	0.55	1.28

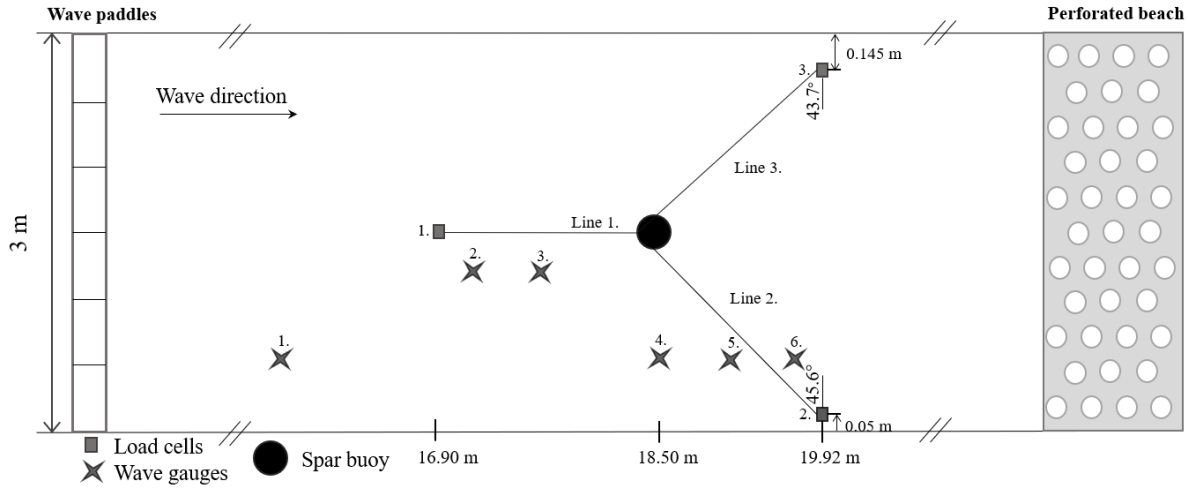

Figure 3.3: Experimental setup of the spar-buoy with three mooring lines connected to individual load cells with wave gauges placed relatively to the model.

.

Figure 3.4: The complete experimental setup with the spar-buoy in MarinLab, a hydrodynamic research facility at HVLs campus in Bergen.

3.4 Wave Conditions

Both irregular waves and constrained waves are studied in this thesis. The sea states are chosen to represent extreme environments for measuring extreme response and mooring loads. The waves are uni-directional, and the same irregular sea states are used for all three models.

3.4.1 Irregular waves

As floating wind turbines are highly dynamic systems, wave conditions for structural design purposes will be designed by a stochastic method applying wave spectra in modeling sea surfaces and wave kinematics. This is modeled using an irregular sea-state spectrum, JONSWAP, where the extreme sea-states are selected from a contour plot from measured wave parameters in the Barents Sea. The location is referred to as Block B by [49] with a water depth of 220 m. The wave conditions studied represent extreme conditions with a 50-year return period. As this contour line is not represented in the probability contour plot for the given site, the sea states are chosen based on measured wave parameters between the 10-year and

100-year contour line in Figure 3.5. The chosen sea states to represent storm conditions are given in Table 3.5 in both full- and model scales and are chosen to represent steep waves.

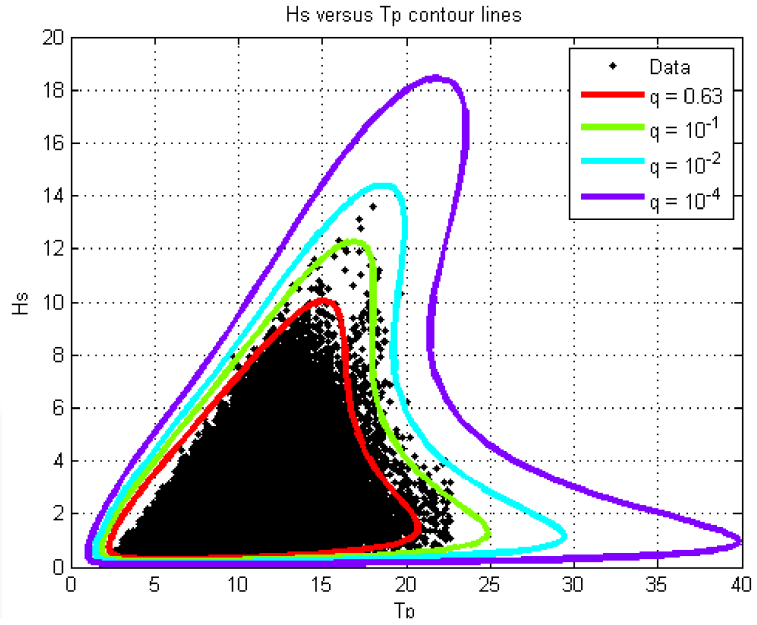

Figure 3.5: Probability contour lines of H_S versus T_p for omni-directional waves at Block B located in the Barents Sea [49].

In addition to wave conditions based on the JONSWAP spectra, a white noise test is also included among the test cases. The white noise spectra are modeled using a H$= 0.02$ m over a frequency range of $f = 0.3 - 2$ Hz. The wave parameters for the white noise test are chosen due to its combination of wave amplitudes with the given wave frequency range being below the steepness limit, as illustrated in Figure 3.9. As breaking waves dissipate wave energy, waves above this limit are challenging to generate with the required energy over all frequencies.

As a measure of how steep the waves in a given sea state are, a significant wave steepness limit adapted for towing tanks given in DNV's class guidelines in [28] is used with the following formulation:

$$S_p = \frac{2\pi H_s}{gT_p^2} < 0.03$$

Sea-state nr. 1 and 2 exceed this limit, and sea state 3 is just below the limit meaning this sea state contains steep and non-breaking waves.

Table 3.5: Experimental values of Hs for JONSWAP spectra with γ=3.3, and white noise spectra.

	Model-scale		Full-scale		Steepness
Sea-state nr.	H_s, m	T_p, s	H_s, m	T_p, s	S_p
1	0.08	1.25	8	12.5	0.033
2	0.13	1.46	13	14.6	0.039
3	0.13	1.73	13	17.3	0.028
4	White noise test: H=0.02 m, f=0.3-2 Hz				

3.4.2 Conditional Waves

In addition to the irregular sea states previously presented, three different conditional wave series are generated. All three design waves are designed for 400 s with a given focal time set for 350 s at a focal position in the model's center at the resting position. The focal time is set towards the end of the time series to allow the model to drift before the focal time to excite extreme events. As MLRW and CRRW depend on the transfer function and phase information for the given model, the design and calibration are described in Section 6.2. As MLW is designed with a focused wave in a random sea, independent of the floaters' characteristics, the design process and calibration are further explained in this chapter.

MLW and CRRW depend on the background sea state, as their elevations, phase, and frequency will change with these. The background sea state used for MLW and CRRW is sea state nr. 3 in Table 3.5. This decision was due to the intention of scaling the wave amplitudes with factors in a range of 0.7 - 1.5 to create steeper and steeper waves to study the nonlinearity effects compared to the expected responses from linear wave theory. As the time was limited in the lab, these tests were not conducted. Therefore the ideal sea-state for the background sea would be sea nr. 2 to represent extreme responses and induce greater non-linear effects, but sea state nr. 3 is used instead without scaling the wave amplitudes.

The focused wave amplitude in MLW is computed after New Wave theory, with the wave amplitude using the theoretical maximum wave height for the given sea state. The theoretical maximum wave height in the random background sea is computed using Eq. 2.27

resulting in a theoretical wave amplitude of 0.118 m. Steep waves introduce nonlinearities; hence a measure of the wave steepness is of interest. Using the breaking wave limit for deep waters from linear wave theory given in Eq. 2.10 results in the steepness of $0.11 < 0.14$, and the focused wave should, in theory, not break. An illustration of the MLW compared to a random background sea is displayed in Figure 3.6 where the difference between the two series is observed around the focal time at 350 s and is identical elsewhere.

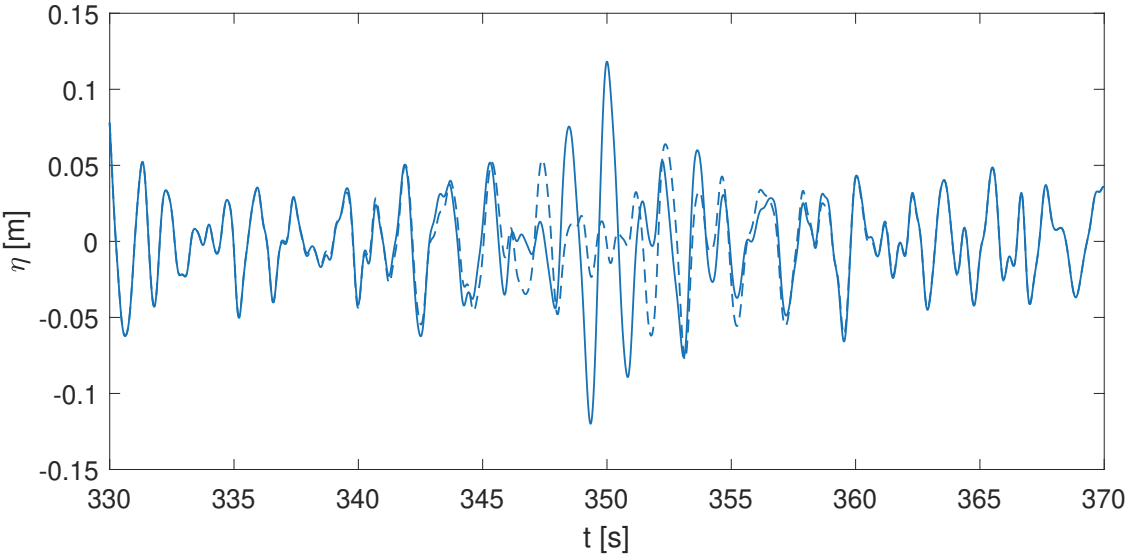

Figure 3.6: A comparison of a random background sea modeled using a JONSWAP spectrum (- - -) and the Most Likely Wave definition in (——).

3.5 Calibration of Measurement Apparatus

All three load cells are linearly calibrated over their complete range using known weights and measuring the output load. The output load is averaged over 10 s to allow the output to settle before each reading. A convergence limit 0f 0.1% is also used for the same reason, in addition, to reducing the hysteresis. The load cell measurements are recorded through a LabView script, and the results from the load cell calibration are given in Figure 3.7a. As a measure of how much the output values vary depending on whether the input is increasing or decreasing, is given in Table 3.6 with other results from the calibration, and the percentage error of full capacity is shown in Figure 3.7b.

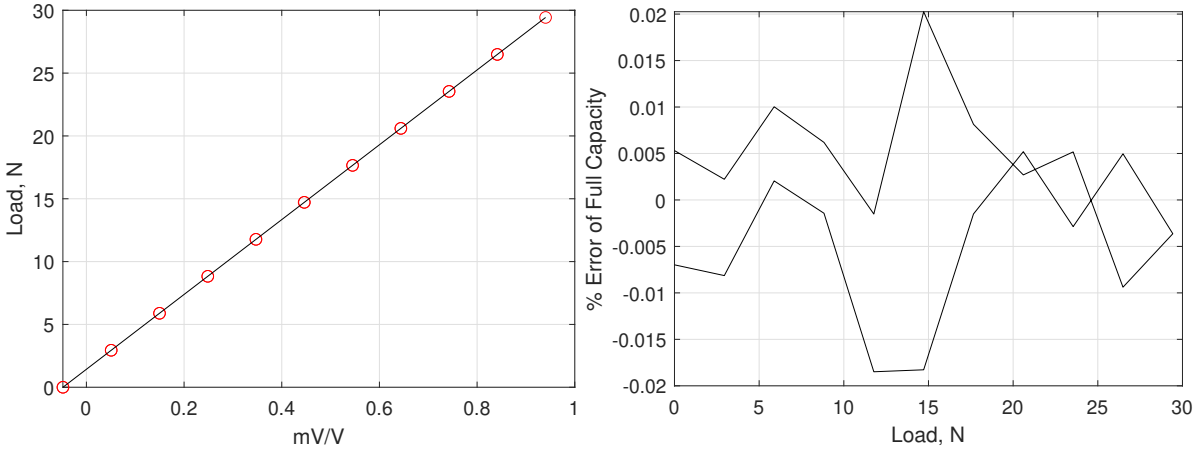

(a) Recorded averaged output load.

(b) Percentage error of full capacity

Figure 3.7: Results from a 10-point calibration of Load Cell 1 using 10 known weights and averaging the output load.

Table 3.6: Applied point loads and hysteresis from calibration of load cell 1

Parameter, unit	Value					
Mass, Kg	0	0.3	0.6	0.9	1.2	1.5
Hysteresis, mV/V	0.00021	0.00017	0.00013	0.00013	0.00028	0.00065
Mass, Kg	1.8	2.1	2.4	2.7	3.0	
Hysteresis, mV/V	0.00016	0.00004	0.00013	0.00024	∼	

The digital wave gauges are calibrated using a three-point static calibration through the wavemaker's software. They are calibrated over a range of 35 cm with an approximate uncertainty of 0.1%. The smallest wave amplitude of 0.01 m generated in the experiments yields an error of less than 1% in the measured wave elevations, considered sufficient.

3.6 Wave Calibration

In order to study extreme response and mooring loads in irregular sea states and constrained waves, it is of utmost importance to calibrate the wavemaker to ensure the energy content and the designed waves' definitions are correctly generated. Therefore, the irregular sea states and the designed waves are calibrated using different methodologies; this section explains both methodology and the resulting wave definitions used in the experimental tests.

3.6.1 Irregular Waves

The random waves are generated and calibrated in the Njord Wave Synthesis software. The wave definitions are defined by a JONSWAP spectra model with wave parameters given in Table 3.5. The down-scaled time length for the simulations is determined using the Froude scaling factor of 100 and a repeat-time of 64 s from the sampling step of 1/64 Hz. A full three-hour duration in model-scale results in an experimental run time of:

$$\frac{10800 \text{ s}}{60 \text{ s} \cdot \sqrt{100}} \cdot 64 \text{ s} = 1152 \text{ s}.$$

An additional time of 30 s is added as a pre-run time to allow for a fully-developed sea only to be considered. This is a measure to ensure greater accuracy and reliability in the estimates of wave spectra and short-term characteristics where movements in the tank and other disturbances are damped out. The focal position in the software is set at a distance of 18.5 m from the wave paddles, adequate to the center of the model at resting position, as illustrated in Figure 3.3. The waves are calibrated without the presence of any models to exclude any diffracted or radiated effects disturbing the generated wave field.

Implemented in the software is the ability to create a linear gain correction based on the differences between target spectra and measured spectrum, a method called Standard Spectral gain correction. This allows phases and amplitudes at different frequencies to be modified to correct errors in the wave tank's transfer function or adjust for other tank effects. Therefore, the uncorrected wave definition is generated and measured where the differences between target and measured spectra are used to compute a linear gain factor added to the wave definition. The adjusted wave definition is then generated and measured. This process is repeated until the measured wave spectra achieve the correct amount of energy.

The measured wave spectra versus target spectra for the irregular sea states are given in Figure 3.8. The fit is, in general, quite close to the target spectra. However, there are some discrepancies in the measured spectra where the peak energy in (b) and (c) is slightly underestimated. This is also observed in the measured wave parameters in Table 3.7. Nevertheless, the difference between the theoretical and measured parameters is less than 5% and there-

fore considered to be within the given tolerances by Chakrabarti in [37] for irregular wave parameters.

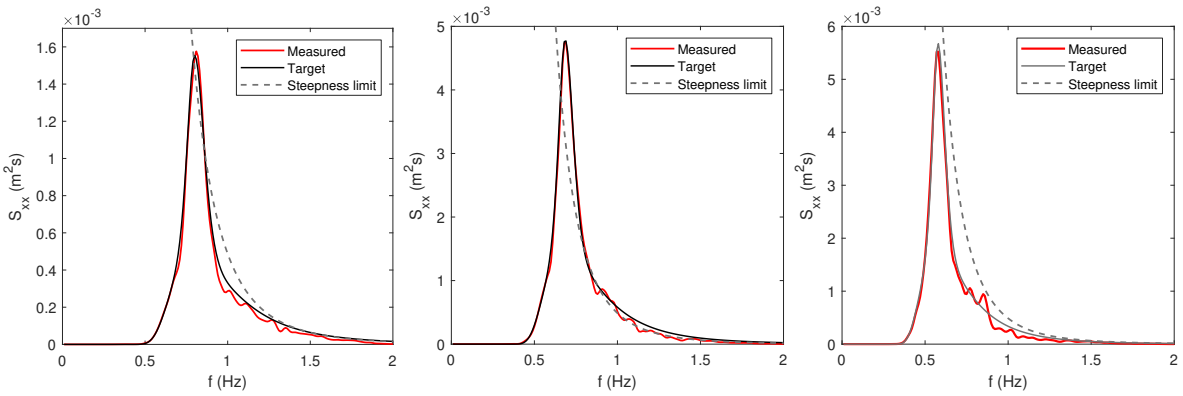

(a) H_s=0.08 m and T_p=1.25 s (b) H_s=0.013 m and T_p=1.46 s (c) H_s=0.13 m and T_p=1.73 s

Figure 3.8: Results from calibration of wave spectra cases with a JONSWAP fit (—) compared to their respective target spectra (—) and a steepness limit for the wave tank (- - -).

Generating a white noise spectrum with uniform energy over all frequencies is challenging in a wave tank due to reflections from the tank walls and beach. The measured spectrum compared to the target spectrum is displayed in Figure 3.9 where an increase in the magnitude of the amplitudes at frequencies close to the steepness limit can be observed. This is due to the measured wave amplitudes possibly becoming greater than defined by the steepness, but the wave will be broken at the crest, possibly causing the increase in energy close to the steepness limit. The target spectrum is computed from the formulation given in Njord wave synthesis manual [50] as:

$$S_{xx} = \frac{(0.25 \cdot H_s)^2}{f_{max} - f_{min}},$$

Where the amplitudes are theoretically zero outside the specified frequency-interval.

Table 3.7: Results from the calibration of the irregular sea-states.

Sea state nr.	Target H_s, [m]	Measured H_s, [m]	Error $\pm$ %
1	0.08	0.0776	3.0
2	0.13	0.1271	2.2
3	0.13	0.1284	1.2
White Noise test	0.02	0.0212	6.0

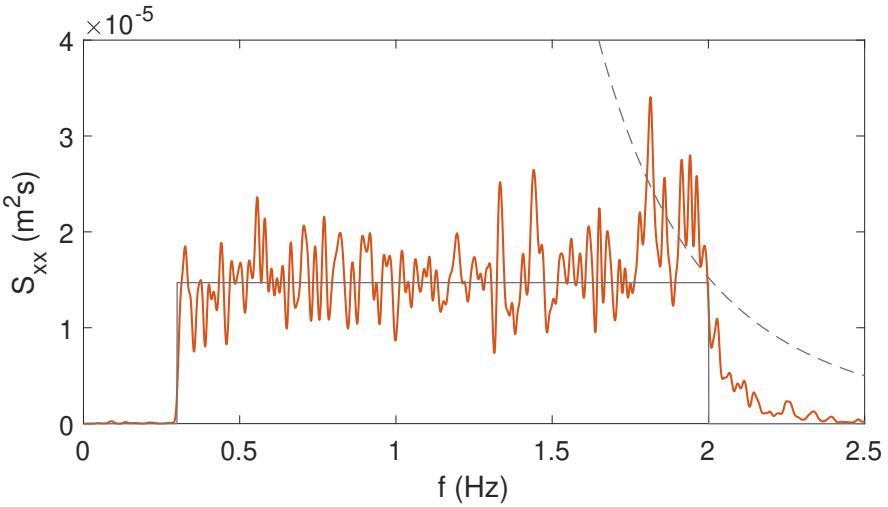

Figure 3.9: Results from the calibration of the white noise spectrum in (—) compared to target spectra in (—) with the steepness limit (- - -) for breaking waves recorded without the presence of models.

3.6.2 Conditional Waves

MLW, MLRW, and CRRW are wave definitions computed with specific properties compared to the random sea states calibrated in Section 3.6.1. This results in a different approach when calibrating these, where wave amplitudes and frequencies around the focal time are essential to be generated as close to the theoretical wave definitions as possible. The theoretical wave definitions are calculated in MATLAB and imported to the wave generating software as a .CSV file containing amplitudes with the corresponding time stamps. The time step in the wave definitions is computed to match the wave gauges' Nyquist frequency. The wavemaker then generates the theoretical time series, and the recorded surface elevations are imported into MATLAB and not calibrated in the Njord wave synthesis as the irregular sea states are.

The method used in this thesis is based on the difference between the measured and theoretical energy amplitude of each frequency component in their respective wave spectra, similarly to the method used for irregular waves. For comparison, the method used for irregular waves uses the software connected to the wavemaker, where the adjustments are added to the wavemaker's transfer function. For the conditional waves, this is done manually, where a linear transfer function is computed based on the measured wave spectra compared to the theoretical spectra. The phase and amplitude of the focused wave are also considered in the calibration, as this specific wave height is designed to occur at a specific time and at the cen-

ter of the model to excite extreme responses and mooring loads. For this reason, the surface elevation of MLW is measured at the same position from the paddles as the location of the model's center at resting position. As the focused wave is constrained such that its peak is computed to occur at 350 s, allowing the model to drift from the resting position, the focal position should ideally have been set to occur at a different position from the wave paddles in order to materialize at the new position of the model due to drifting.

The recorded time series is transformed into the frequency domain using FFT, which gives the wave spectra. The ratio between the measured amplitudes of the nth frequency component versus nth theoretical amplitude is used to create a linear transfer function, K_n. For every correction, the last gain correction is multiplied by the new linear factor of the nth frequency component, as given by:

$$K_n \; = \; (K_{n-1}) \left(\frac{A_{target,\, n}}{A_{measured,\, n}} \right), \quad n = 1, 2, 3, .., N.$$

As the MLW definition is computed by adding the focused wave and random background sea definition together, this transfer function is multiplied by both the background sea amplitudes and focused wave amplitudes before the wave definitions are added together, creating a corrected wave series of MLW. The new wave definitions are then exported as a table with amplitudes and time steps to be generated and recorded. This process continues until the recorded time series are sufficiently close to the target spectrum. The root-mean-square error (RMSE) between the measured and target time series is used as a measure of the quality of the wave generation of the MLW, computed by the following equation:

$$RMSE = \sqrt{\frac{1}{N} \sum_{n=1}^{N} (WG4 - TTS)^2}\,,$$

where N is the total number of recorded samples, WG4 stands for the signal from wave gauge 4 placed at the center of the body, and TTS stands for the target time series.

The measured wave spectra of the initial wave series yield a lower energy content over the frequency range, where a linear gain correction results in wave spectra close to the theo-

retical spectra as depicted in Figure 3.10b. The target is a JONSWAP spectrum defined by $H_s = 0.13$ m and $T_p = 1.73$ s and is used because there exist no standard wave spectra for the MLW known to the author at the time being. Using pwelch in the computation of a wave spectrum of the input wave definition of MLW results in a H_s estimate of 0.1338 m, a difference of approx. 2.9% from the target wave spectra of the random background sea without the focused wave. As this difference is relatively small, it most likely results from the wave amplitudes being higher than the initial random sea around the focal time depicted in Figure 3.6. Therefore the difference is considered sufficiently small, and the JONSWAP spectrum is used for computing the gain correction. Figure 3.10a-c show that the distribution of wave energy increases with each gain correction added, whereas the second correction appears to contain too much energy around the peak frequency.

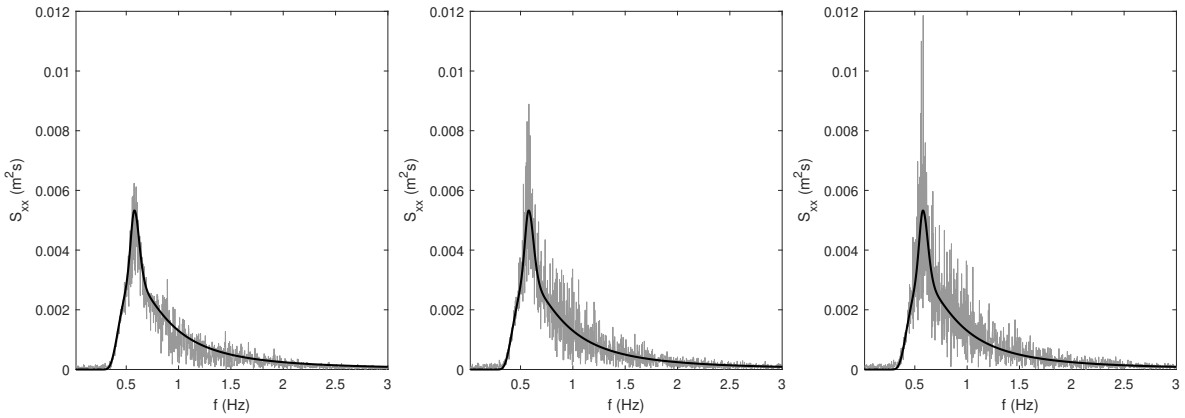

Figure 3.10: Measured wave spectra of MLW (—) compared to target spectra (—), with a JONSWAP fit with $H_s = 0.13$ m, $T_p = 1.73$ s, with (a) being the uncalibrated wave series spectra, (b) being the two-gain corrected wave series spectra, and (c) being the two-gain corrected wave series spectra.

As shown in Figure 3.11, the amplitude of the focused wave with no gain correction is approx. -18% lower than the target amplitude. After one gain correction, the focused wave amplitude is approx. 1.4% higher than the target amplitude, whereas a second gain correction results in a 0.6% higher wave amplitude. However, with the last gain correction, the focal time has shifted compared to one, and no gain correction. The wave series without correction has the lowest RMSE value. Since this gain correction has the lowest wave amplitude, the wave definition after one gain correction is chosen since this wave amplitude is close in value to the theoretical amplitude and transpires at approx. 350 s. This gain correction also has a lower

RMSE value than the second gain correction and is the time series with energy content closest to the target spectra. The second gain correction results in a more significant shift of the focused wave, transpiring earlier than the others. A third gain correction was not considered crucial because the time required to calibrate these waves was more time-consuming than the irregular 3-hour sea-state and, therefore, not conducted. The measured parameters compared to the target values are summarized in Table 3.8.

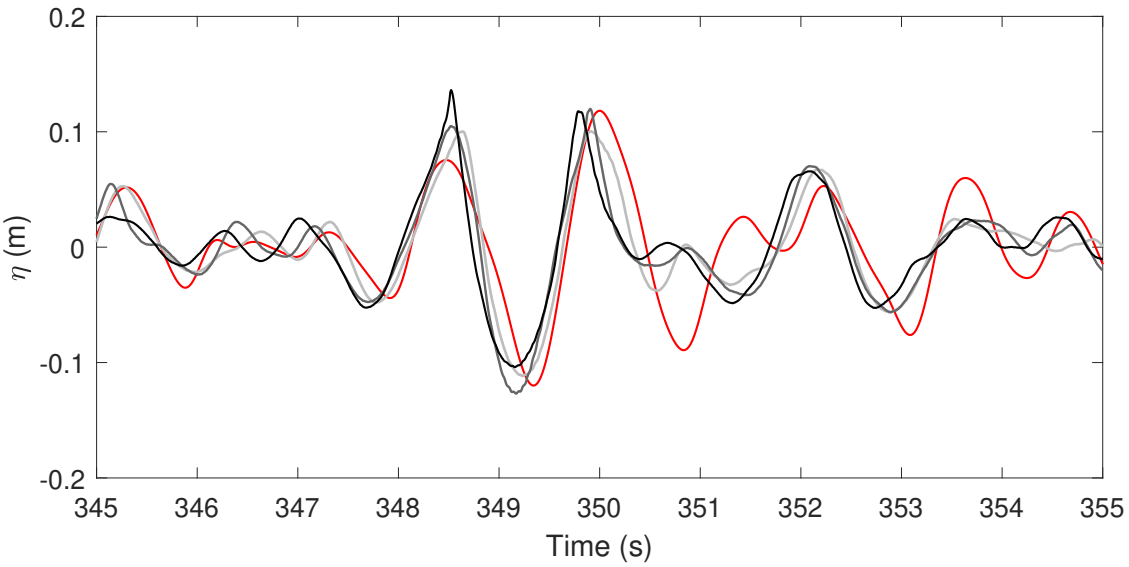

Figure 3.11: Results from the calibration of MLW time series where: (—) is target, (—) is without gain correction, (—) is after one gain correction, and (—) after two gain corrections.

Table 3.8: Measured properties of MLW with computed RMSE-values compared to target values for wave amplitude, focal time, and RMSE-values from the calibration of MLW definitions compared to target values.

Wave definition	Wave amplitude, m	Focal time, s	RMSE, m
Target	0.1181	350	∼
Gain 0	0.1003	349.9	0.0146
Gain 1	0.1198	349.9	0.0205
Gain 2	0.1174	349.8	0.0248

Observed from the calibration of MLW is a slight shift of the focal point in Figure 3.11. A study of the path of the focused wave downwave in the wave flume is included in Figure 3.12 as the author of [48] found that nonlinear interactions taint focal quality by shifting the focal position. Figure 3.12 is a minor shift where the maximum amplitude expected to arise at

the focal position appears to transpire at the position of WG6 located further from the wavemaker and behind the focal point. The exact position of the wave gauges are given in Figure 3.3 and Table 3.4. The wave forming at the position of WG6 has an amplitude of 0.1199 m compared to 0.1198 at the focal position. The shift of the focal point could mean that the actual wave forcing on the floater, which has also drifted backward, is higher than expected by theory. Therefore, analysis of the results should ideally consider this difference, which is not included in this thesis and suggested for further work.

However, compared to the theoretical wave series represented in red in this figure, the wave amplitude recorded at WG4, represented in black, is close in amplitude and shape. As this wave gauge is located at the center of the model's resting position, the wave data recorded by this wave gauge is further used in this thesis, as the methodology for calibrating these waves is not within this project's scope. The uncertainties in these methods and the slight shifting of the focal point are, therefore, only established to be further discussed with the results in Chapter 7.

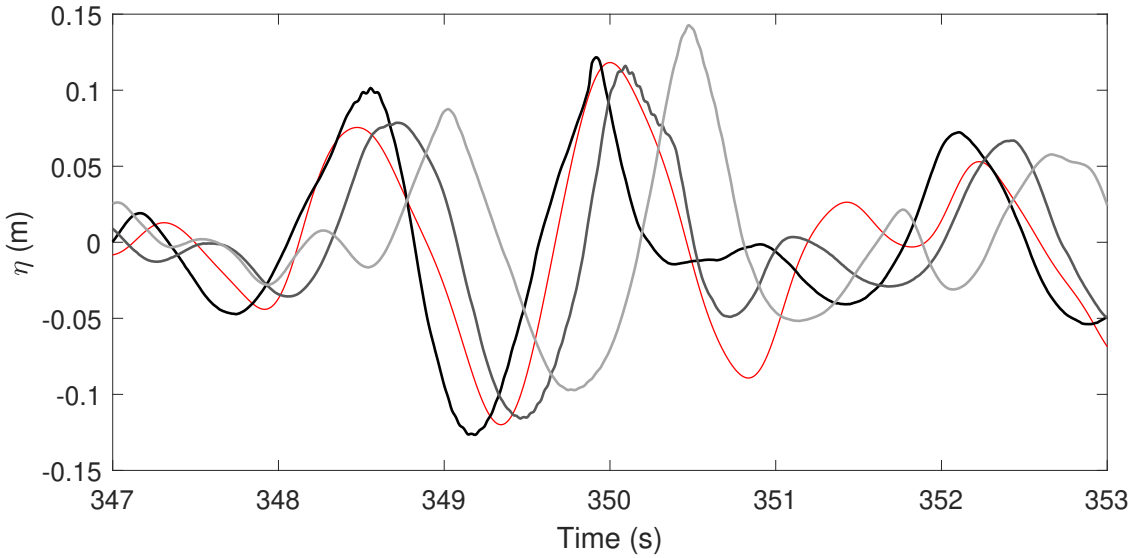

Figure 3.12: Recorded wave elevations of the focused wave in MLW at different locations in the wave flume where the target series is presented in (—), the wave gauge at resting position in (—), WG5 in (—), and WG6 in (—).

As the conditional waves have limited references regarding their calibration methods, the method used in this thesis is experimental. The generated wave definitions in the wave fume differ from the theoretical wave series as depicted in Figure 3.13. As the MLW series is an ir-

regular sea-state with a focused wave occurring with a specific amplitude, its wave period is irrelevant to this design. Therefore, the differences between the target and measured background sea are considered unimportant for the results where the focus lies on the measured wave amplitude, which only differs approximately by 1.4%. The steepness is theoretically 0.11 and, in theory, should not break, which was also observed during calibrations.

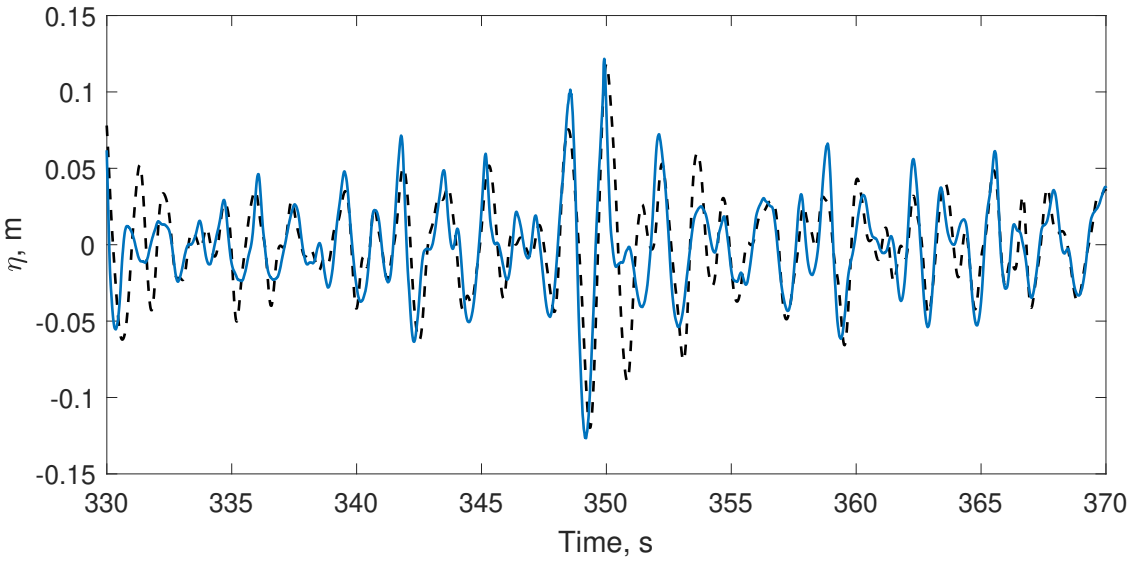

Figure 3.13: Measured wave elevations of MLW (—) compared to target wave elevations (- - -) during calibration of the conditional wave series.

3.7 Free Decay Test

Before experimental testing, a series of decay tests have been conducted for both FOWTs. The tests are carried out by displacing the models from their equilibrium and letting them oscillate freely until their motions are fully damped. The recorded time-series of the responses from the decay tests are least-square fitted using the exponential sinusoidal decay curve given in Eq. 2.44. The decaying rate yields the linear damping coefficient from Eq. 2.45. The damped eigenfrequency is estimated using a least-square fit method and used to compute the undamped eigenfrequencies using Eq. 2.9. This process is illustrated in Figure 3.14 showing the results from a decay test performed in heave for the semisubmersible. Here, the recorded oscillation is represented in blue, the curve-fit in dashed red, and the decaying exponential rate in a dashed black line. The damped eigenperiods for both concepts are presented in Table 3.9 in full-scale values with their respective estimated damping coefficient.

Good decay tests in sway for the spar-buoy were difficult to achieve due to the strong coupling in roll and the mooring configuration inducing a significant motion in yaw. Therefore, the recorded oscillations in this degree of freedom were insufficient to give an accurate estimate of its characteristics and, therefore, not included in Table 3.9.

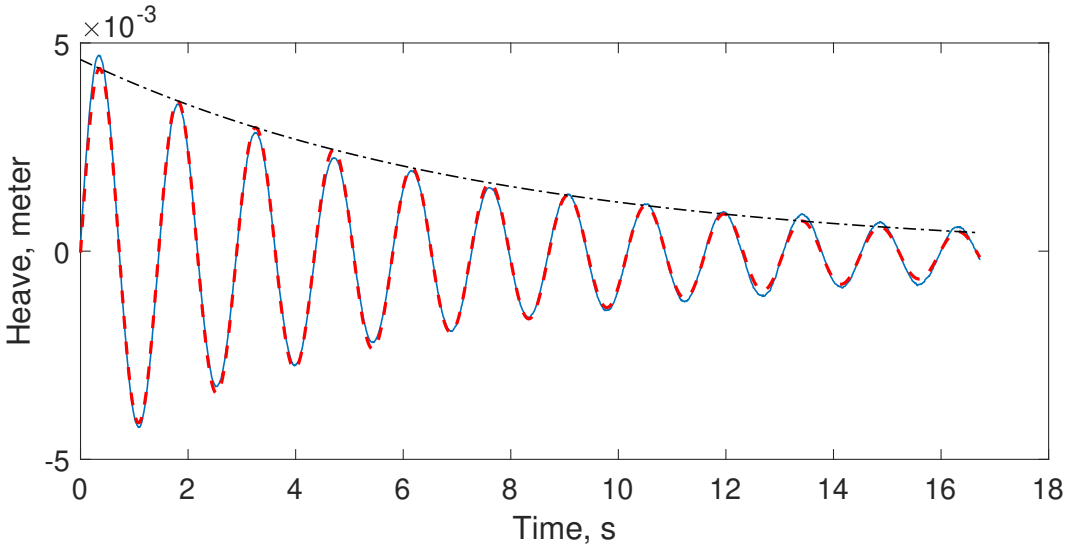

Figure 3.14: Recorded decay curve in heave for the semisubmersible in (——), the curve fitted line in (- - -), decaying exponential rate in (- - -).

Table 3.9: Eigenfrequencies and dampings for the spar-buoy and semisubmersible given in in model-scale values.

Floater / DOF	Spar-buoy		Semisubmersible	
	f_d [Hz]	n [Ns/m]	f_d [Hz]	n [Ns/m]
Surge	0.0670	0.027	0.131	0.030
Sway	$\sim$	0.011	0.127	0.028
Heave	0.361	0.025	0.689	0.132
Roll	0.732	0.020	0.387	0.077
Pitch	0.087	0.030	0.374	0.029
Yaw	0.111	0.035	0.141	0.022

3.8 Signal Processing

Before analyzing the experimental results, an essential part of evaluating and presenting these is how the data is processed. A high sampling frequency of 2000 Hz is used to record the mooring line tensions as this is the minimum integer frequency that the NI data acquisition unit can measure, and snap loads are phenomena short in time. This results in significant noise that needs to be filtered before further processing. As 2 Hz is the wavemaker's maximum generated wave frequency, the second-order forces are up to 4 Hz, and higher-order forces have even higher frequencies. A zero-phase low-pass filter is used to filter out the noise elements in the recorded time series where a cutout frequency is defined. Using a low cutout frequency results in a smoother signal but may also filter out too much of the data. Therefore, a cutout frequency of 16 Hz is used as this appears to filter out most of the noise while keeping up to 8 Hz effects in the signal. Figure 3.15 depicts the results from running the data through a zero-phase low-pass filter with a cutout frequency of 16 Hz, where the filtered signal, presented by a red line, shows significantly less disturbances compared to the original signal presented in grey.

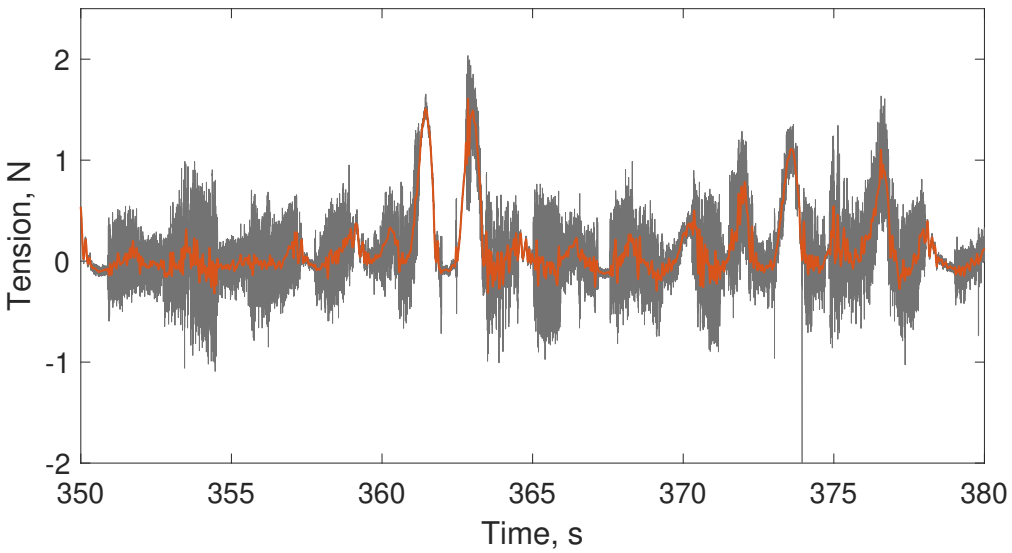

Figure 3.15: Mooring loads recordings before (—) and after (—) using a zero-phase low-pass filter to remove outliers and noise. The cutout frequency here is set to 16 Hz.

Great care is also taken when the data is cropped to ensure the correct phase information is obtained from the recordings. Therefore, a triggering function is implemented. This consists of a 5 V pulse signal sent from the wave maker while seas are generated in the wave flume.

This voltage signal automatically starts the floaters' recordings, while the recordings of the mooring line tensions are manually started through a LabView program. This program also records the wave generator's voltage signal, illustrated in Figure 3.16. Here, a pulse signal of approximately 5 V can be observed starting at ca. 54 s and ending at 1236 s, representing a simulation length of 1182 s. The time step in which the LabView program starts recording the pulse is used to crop the mooring line data where the start and end of the pulse are marked as a red circle. A pre-determined time lag is also implemented in Qualisys for recording the floaters' response, which is also accounted for when the data is cropped. This time leg is set to be 2.02 s which are added to the 30 s cropped from the beginning of the series to exclude data from the build-up phase.

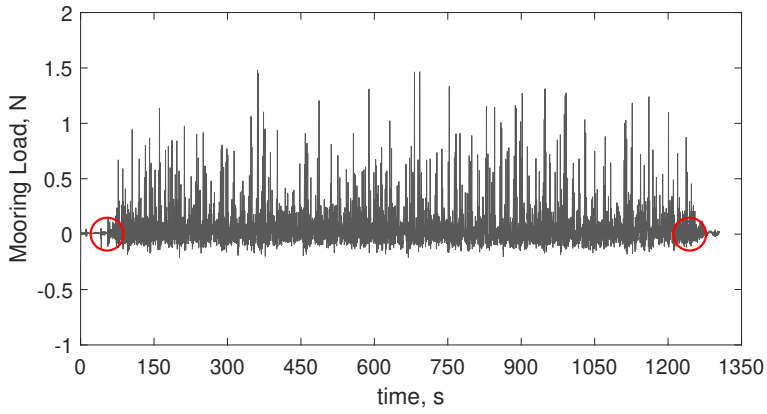

(a) Uncropped time series of recorded loads in mooring line 1 for the spar-buoy in H_s=0.13 m and T_p=17.3 s.

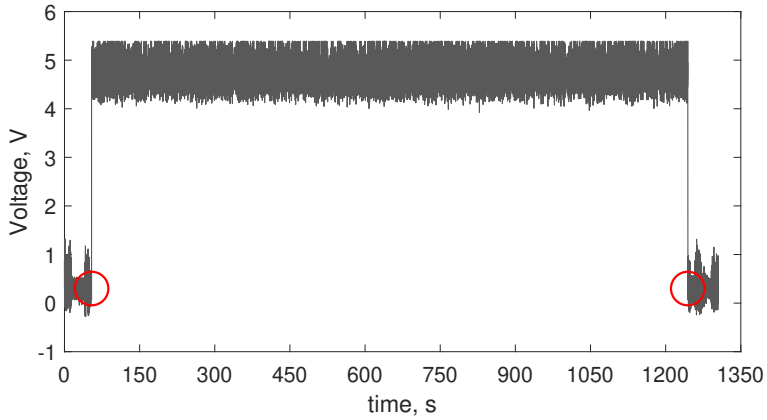

(b) Recorded pulse signal from the wave generator during when waves are generated.

Figure 3.16: An example of the triggering function consisting of a 5 V signal sent from the wavemaker while waves are generetated in the fume where (○) illustrates the start and stop of the pulse signal.

4. Numerical Methodology

The design and methodology for generating a 3D model of the spar buoy and setting up the station-keeping system are presented in detail for the Spar Buoy in this chapter. This includes the process from modeling a 3D model and generating a panel and structure model in GeniE to be used in the diffraction/radiation analysis in OrcaWave, to the complete setup in OrcaFlex.

4.1 3D model in GeniE

The spar buoy is modeled in GeniE (Sesam) following the main dimensions given in Figure 3.1. The spar buoy's main dimensions are measured directly from the physical model, and the total mass includes mooring lines, measurement apparatus, and additional equipment used in the experimental tests. The model-scale structure consists only of the substructure itself; hence the nacelle and hub are designed after fictional dimensions for illustration purposes. The same extends to the turbine blade geometry, which uses the foil geometry, NRELS822, downloaded from [51]. Here, the downloaded foil geometry is modeled using the function: *CreatePolylineFromASetofpoints(Array(...))* where the normalized coordinates, scaled to the desired size, are implemented as a string of coordinates in this function.

The plate thickness and material of the structure are not related to the full-scale turbine such that a dummy material and dummy thickness is used with zero density, and the spar buoy's total mass is instead included in the diffraction analysis. The turbine blades are included for illustration purposes only and not related to the full-scale version and are modeled in idle mode as no wind conditions are considered in this thesis. The full 3D model is displayed in Figure 4.1, where the damping plate is modeled after the measured dimension of the actual damping plate in the model scale given in full-scale values in Figure 4.2. The dimensions are

given in meters.

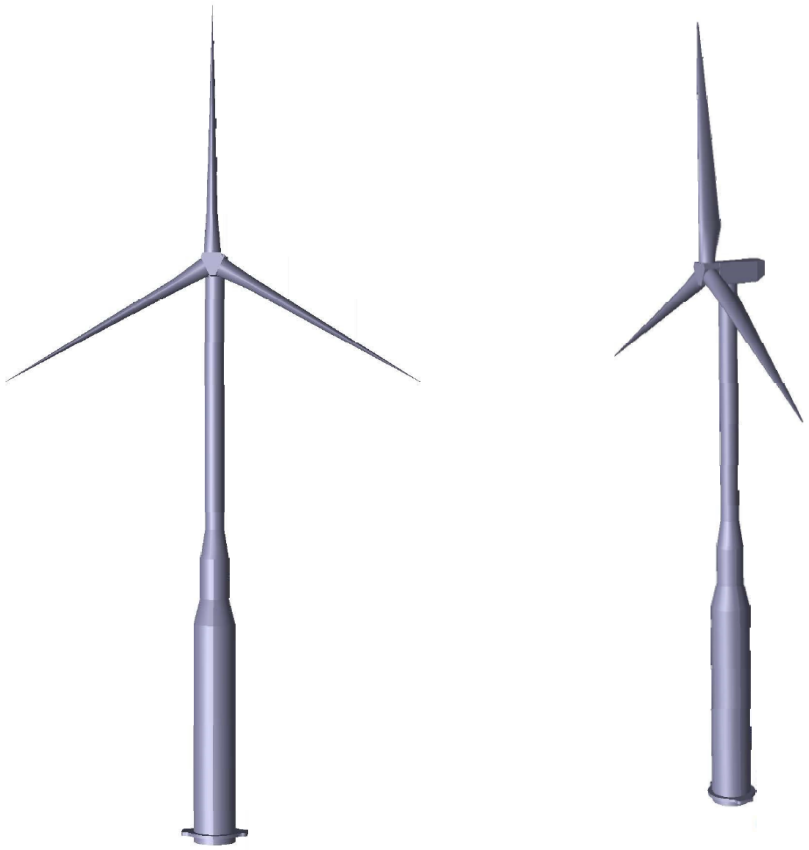

Figure 4.1: The 3D model of the spar buoy modeled in GeniE in idle mode using the measured dimension given in Figure 3.1. The design of the top structure, including the hub, nacelle, and turbine blades, are modeled using fictional dimensions, are only included for illustration purposes, and are not related to the full-scale version.

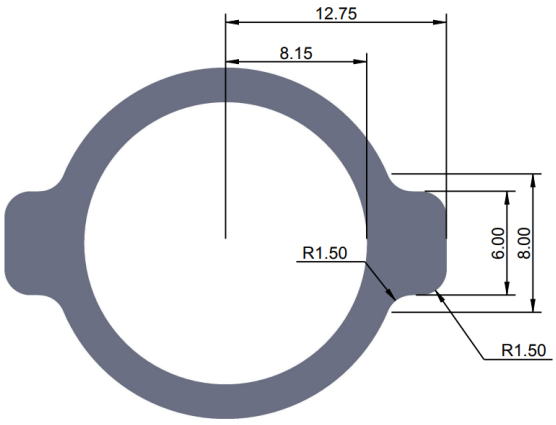

Figure 4.2: Sketch of measured dimensions of the damping plate given in full-scale dimensions in meters

4.2 Diffraction Analysis in OrcaWave

In linear theory, first-order forces are calculated in equilibrium positions. Therefore, the panel model represents the submerged part of the structure up to the mean water level (MWL). Based on the results of experimental tests, this is up to 90 m from the baseline. The center of mass is assumed to be located at the same position as the center of gravity, and the experimental value from Chapter 3 is used. In order to reduce the computational time in the diffraction/radiation analysis, the submerged part of the structure is also divided into four equally spaced sections such that only 1/4 of the model meshes, creating the panel model illustrated in Figure 4.3. The panel model is then imported to OrcaWave for the diffraction/radiation analysis. The hydrodynamic coefficients are obtained using the panel model in Figure 4.3 and the structural properties given in Table 4.1 as input in OrcaWave.

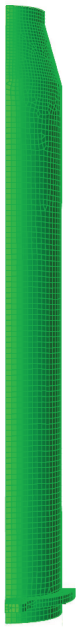

Figure 4.3: 1/4 panel model used in OrcaWave for diffraction/radiation analysis with a mesh element-size of 1 meter.

OrcaWave is a potential flow-based panel code. Therefore, the viscous forces acting on the structure are considered via Morison's equation with empirical drag coefficients as given in Eq. 2.46. Morison elements are defined in OrcaWave for the heave plate and the cylindrical shape of the substructure separately to account for viscous drag forces. These elements are

defined using the geometrical dimensions with the designated drag coefficients given in Table 4.2, inspired by values used in [52], and [53]. The latter reference states that a heave plate requires a separate drag coefficient as tank tests have shown the viscous drag forces on this plate to be independent of the Reynolds number due to its sharp edges. As a coefficient of 4.8 is used in both articles, this value is also used in this thesis for the damping plate. The 0.001 value for the drag coefficient used in heave for the cylinder was initially set to be zero, equal to the value used in [54]. However, a value of 0.001 results in more accurate heave damping, as seen in Figure 4.8. This small change from 0 to 0.001 and its effect on the system's damping may result from the quadratic velocity term in Morison's equation.

The environment in the diffraction/radiation analysis in OrcaWave is defined by a water depth of 220 m with a table of wave periods and wave headings. The wave periods are for this project defined from 10 s to 300 s with a time step varying from 0.1 s to 10 s. The finer time step is used for wave periods close to the spar buoy's eigenfrequencies for a finer resolution around these frequencies in the transfer functions. As only beam seas are studied in this project, only a single wave heading from 0 degrees is included.

Table 4.1: Input parameters in the diffraction analysis in OrcaWave.

Parameter, unit	**Value**
Draft, m	90.02
COM, m	[0, 0, 35.8]
R_{xx}, m	48.21
R_{yy}, m	48.21
R_{zz}, m	0

As Morison drag is quadratic, a linearized model in OrcaWave is obtained by linearization using a stochastic method based on a wave spectrum. The documentation for OrcaWave in [55] informs that different standard wave spectra can be used in the linearization, such as the JONSWAP spectrum. Inspired from the methods in [54] where the same spectrum used in the analysis in OrcaFlex is used to linearise the drag coefficient in OrcaWave, therefore, the JONSWAP spectrum defined by H_s=0.13 m and T_p=1.73 s is used here due to this sea-state being below the breaking wave limit as explained in Section 3.4.1. The linearization will affect the displacements RAOs, but not the load RAOs, damping, or added mass according to [54].

Table 4.2: Floating Platform Hydrodynamic Properties

Parameter, unit	**Value**	
Water Density, kg/m^3	1.025	
Water Depth, m	220	
Center of Buoyancy, m	[0, 0, 43.578]	
Viscous-Drag Coefficient	Cylinder	Damping Plate
C_{dx}	1.0	0.7
C_{dy}	1.0	0.7
C_{dz}	0.001	4.8

The settings used to compute the hydrodynamic coefficients in OrcaWave is panel pressures and velocities, meaning higher order effects are not considered. This decision is made to reduce the computational time, as higher-order effects increase this significantly. Mooring line stiffnesses and damping coefficients estimated from the experimental decay tests are not included in OrcaWave as these depend on the quadratic transfer functions (QTFs), which are not used in a linear model. Instead, these are included as input in OrcaFlex, further explained in Section 4.3. Figure 4.4 shows the resulting RAO curve in heave from the diffraction analysis, where an eigenfrequency of approximately 27.7 s is observed, close to the eigenperiod of 27.68 s from the experimental decay tests. The RAO curves for surge and pitch are not presented in this section as these depend on the mooring system, further explained in Section 4.3.

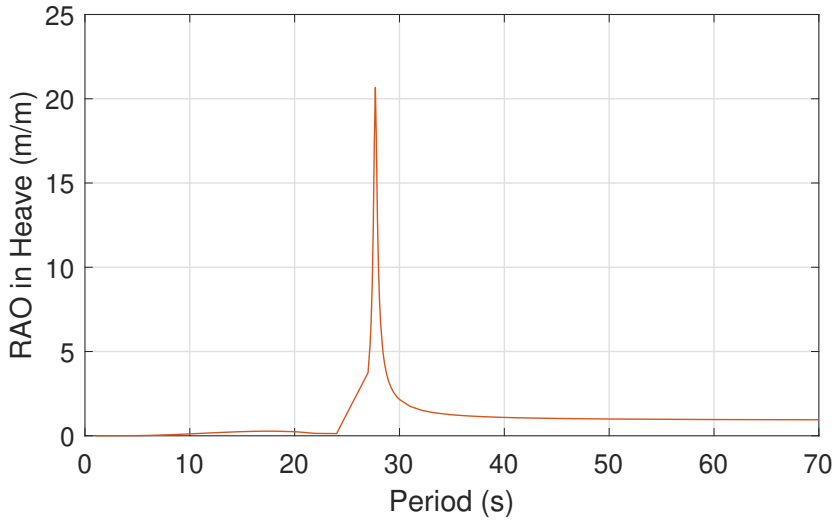

Figure 4.4: RAO curve in heave from diffraction analysis in OrcaWave with drag forces included by implementing Morison elements.

4.2.1 Mesh-sensitivity Analysis

A Mesh sensitivity analysis is conducted to consider if the mesh is refined enough to give accurate results without being unnecessarily dense, as the density affects the computational time. This is also conducted to study the sensitivity of the hydrodynamic coefficients related to the mesh density, where mesh-element sizes of 4 to 0.8 m are used to generate panel models imported to OrcaWave. An illustration of how the mesh density increases with the decrease in element size is given in Figure 4.5. Here the body mesh is displayed with symmetry in both xz and yz planes in OrcaWave. The corresponding panel element is the number of elements in the quarter panel model before using symmetry.

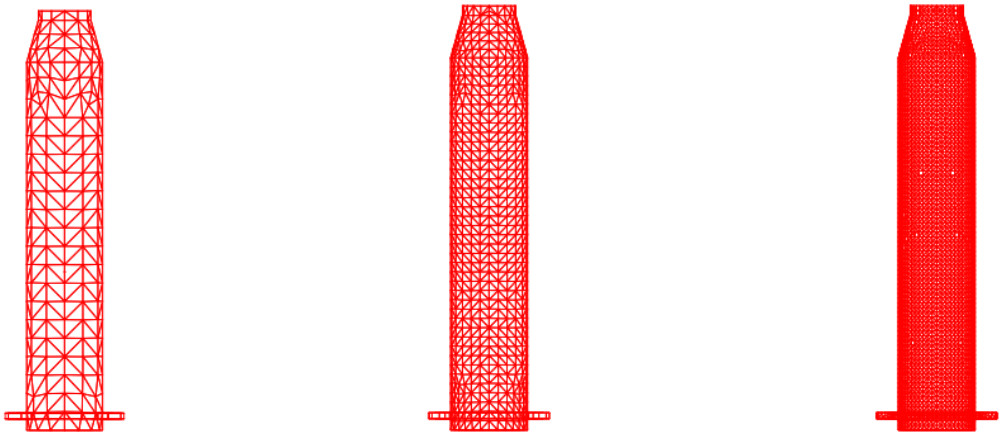

(a) Mesh-density of 4 m consiting of 348 panel elements

(b) Mesh-density of 2 m consisting of 1337 panel elements

(c) Mesh-density of 1 m consisting of 2102 panel elements

Figure 4.5: Three body-meshes of the spar buoy in OrcaWave with a mesh-density size in (a) of 4 m, (b) 2 m, and (c) 1 meter. The body meshes use symmetry in both xz and yz planes in OrcaWave.

The hydrodynamic coefficients evaluated in the mesh-sensitivity analysis are the RAO, added mass, and damping curves in heave. As the RAO curves are not generated to describe the spar buoy motions in its moored condition, the RAO curves in surge and pitch are therefore not included here as these are assumed to change when mooring lines are included in OrcaFlex in Section 4.3.1. The results from the sensitivity analysis are displayed in Figure 4.6. Figure 4.6a shows how the coarser panel models deviate the most, and the peak around 27.7 s appears to converge for the element sizes of 1.5, 1, and 0.9 m. The panel model with an element

size of 3 m shifts from 27.7 to 28 s in addition to a higher amplitude than the converged peak. A panel model consisting of panel elements of 4 m and 2 m appears to have a peak at 27.7 s but has a lower amplitude than the converged group. The most refined mesh with an element size of 0.8 m results in approximately a shifted peak to 27.6 s compared to the experimental eigenperiod equal to approx. 27.7 s. The same trends with the finer and coarser meshes are observed in Figure 4.6b and c for the added mass and damping coefficients.

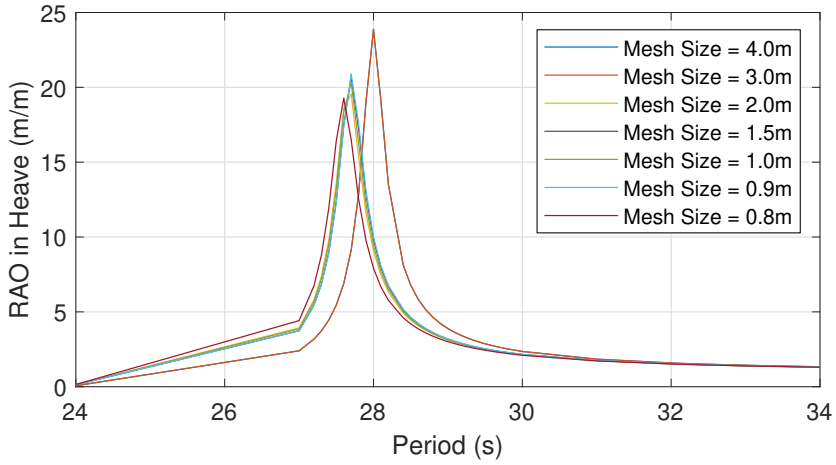

(a) RAO in heave

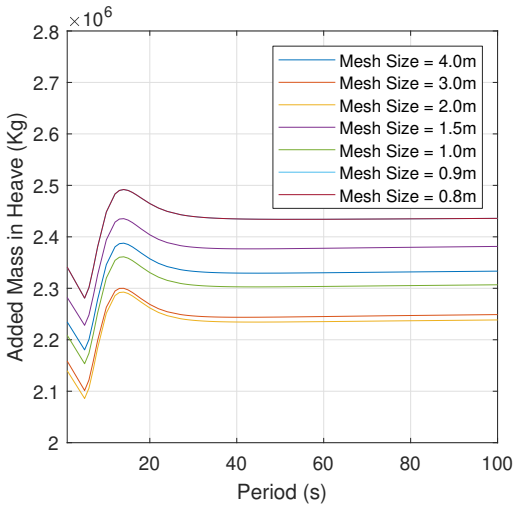

(b) Added mass in heave

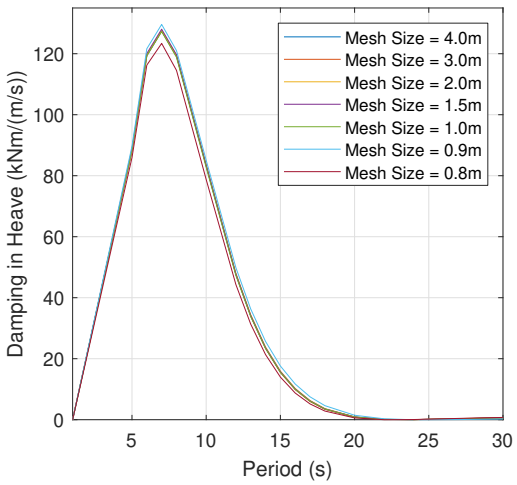

(c) Damping in heave

Figure 4.6: Figure (a), (b) and (c) compares the RAO curve, added mass and damping in heave related to the body-mesh of the spar buoy in the diffraction analysis in OrcaWave. The mesh-size of the panel elements from a coarser mesh of 4 m to a finer mesh of 0.8 m

A general method in generating a panel model is to use a more significant number of panels near the mean water level as the first order forces are computed by integrating the pressure

on the panel up to the mean water level. As the computational time was only a few minutes until a mesh size of 0.9 m and lower increased significantly, a mesh size of 1 m (2102 panels) is further used in this thesis. Using a coarser mesh on the cylindrical body with a finer mesh around mean sea level and damping plate could reduce the computational time and keep the finer mesh around areas of greater importance.

4.3 Numerical Setup in OrcaFlex

Initially, the imported hydrodynamic data from the diffraction analysis into OrcaFlex are checked against the data given in OrcaWave. This is to ensure the data is correctly imported before further setup. The spar buoy is modeled in its moored condition in OrcaFlex. The experimental mooring line configuration consists of slack lines mounted above the water where the mass is assumed to be negligible and the stiffness linear, as explained in Section 3.3. Therefore, the mooring lines are modeled using links-elements in OrcaFlex as these are modeled with an unstretched length and a linear stiffness coefficient as the only input, which is summarized in Table 4.3 for the individual mooring lines.

The input values used for modeling the spar buoy in OrcaFlex are all based on experimentally estimated values and setups and are therefore highly sensitive to inaccuracies from the experiment. Caution was taken when measuring the mooring lengths and angles and determining the mooring line stiffness as accurately as possible to minimize the differences between the numerical and experimental setup. Experiences and lessons have been learned along the way where the initial setup in OrcaFlex was set up as a replica of the experimental setup illustrated in Figure 3.3. This caused a motion in yaw that was not observed to the same extent experimentally, where a solution to constrain this motion was not found. The yaw-motion appeared to be caused by the mooring system, where a solution to minimize the yaw-motions was to make line 3 a duplication of mooring Line nr. 2 about the x-axis.

Using identical mooring lines about the x-axis mounted at 60 degrees to the incoming waves constrained the yaw motion. However, as can be seen in Figure 3.4 the mooring lines from the experiment are observably quite slack and hanging from the load cells, which are mounted 23 cm above the water, and the lines are touching the water along its path to the spar buoy. This

configuration is experimentally used to induce snap loads. However, it makes the numerical mooring configuration more challenging to recreate. Therefore, the links element may not be the best tool to model these numerically. However, due to the lack of information about the moorings in full scale, minimal parameters can be estimated from the experiment setup, making the link element a better fit when these are treated with linear stiffnesses. Because of this, the lengths of the three mooring lines are changed from the lengths given in Table 3.3 to 200 m and positioned at a distance of 200 m from the model. In addition to the mooring stiffness and lengths, the coordinates are all summarized in Table 4.3. The coordinates are related to the local vessel coordinate system in OrcaFlex, located at the model's center, 90 m below mean sea level.

The experimental mooring line stiffnesses have also been tuned numerically as the experimental stiffnesses in OrcaFlex resulted in an eigenperiod lower than the experimental eigenperiod for surge. A possible reason for the experimental mooring line stiffness no longer being a good fit for the numerical model may be a result of the changes in the numeric mooring line configuration. Therefore, the stiffnesses are tuned using the relation between the eigenfrequency from Eq. 2.43 assuming the total mass in the system is constant, and the only parameter changing is the mooring line stiffness, k. By using the initial stiffness coefficient from the experiment, as well as the relation between the numerical eigenperiod and target from the experiment:

$$k_{new} = k_{old} \cdot \left(\frac{T_{numerical}}{T_{target}} \right)^2,$$

results in a new stiffness used as input in OrcaFlex. This method is iterated until an eigenfrequency in surge sufficiently close to the experiment is achieved. The numerical eigenperiods in OrcaFlex are estimated by performing numerical decay tests in OrcaFlex, further explained in Section 4.3.1. Table 4.3 presents the final mooring line stiffnesses.

Table 4.3: Mooring system characteristics used as input in OrcaFlex given in full-scale dimensions scaled using Froude's geometrical scaling with λ=100.

Line nr.	**Stiffness, k [kN/m]**	**Length, l_0 [m]**	**Coordinates [m]**
Line 1	48.895	200.0	[-205.65, 0, 0]
Line 2	46.116	200.0	[100, -178.912, 0]
Line 3	46.116	200.0	[100, 178.912, 0]

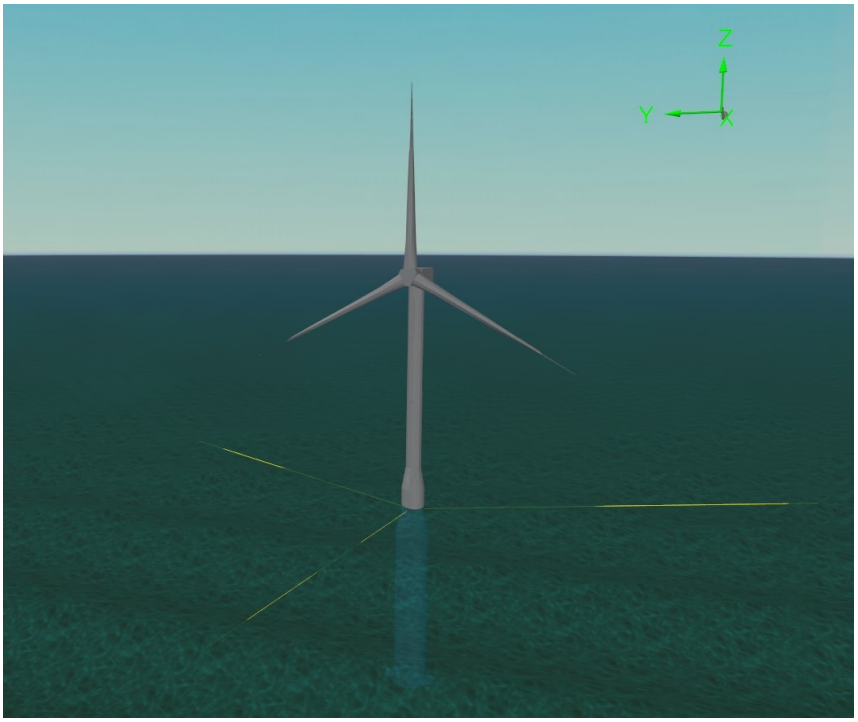

Figure 4.7: The spar buoy's complete setup with mooring lines modeled using *links* in OrcaFlex.

4.3.1 Decay Tests in OrcaFlex

Prior to time-series analysis in OrcaFlex, a series of decay tests have been conducted in surge, heave, and pitch for the numerical model in OrcaFlex. This ensures that the same system characteristics are correctly represented in the numerical model compared to the experiment. The decay tests are performed by setting an initial position in the desired degree of freedom in OrcaFlex and running a time series with waves of zero height, where to this author's knowledge, it does not appear possible to run a time series without a wave train. No other environmental effects are included, and the motion setting includes the effect from added mass and damping, in addition to other damping to include the linear damping coefficients estimated from the experimental decay tests to a value of 100 kNm/s in surge. The resulting decay curves are presented in Figure 4.8 and are normalized using the maximum amplitude.

The numerical decay curves are curved-fitted using the same methods as for the experimental decay curves in Section 3.7. The estimated numerical eigenperiods are compared to the experimental eigenperiods in Table 4.4 where the numerical results show a good fit compared to the experimental curves. However, the damping in pitch is slightly higher than in

the experiment, but due to the coupling effect between surge and pitch, a lower damping value results in a more uneven surge motion. Therefore, the final results presented here are considered sufficiently close to the experimental curves.

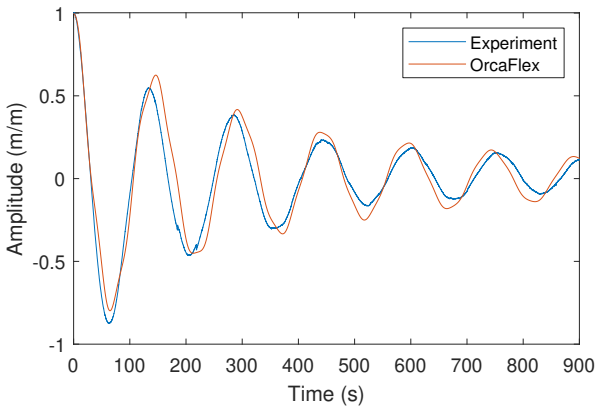

(a) Numerical and experimental decay test in surge.

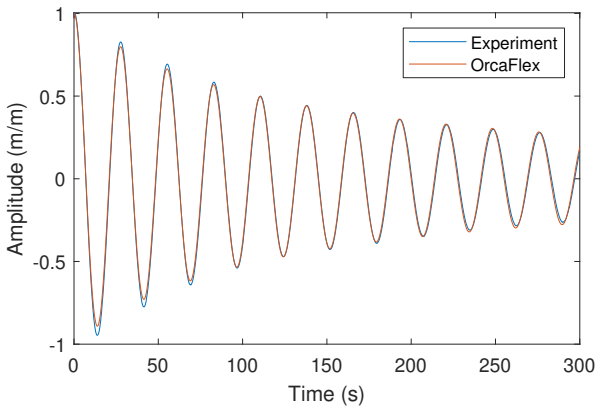

(b) Numerical and experimental decay test in heave.

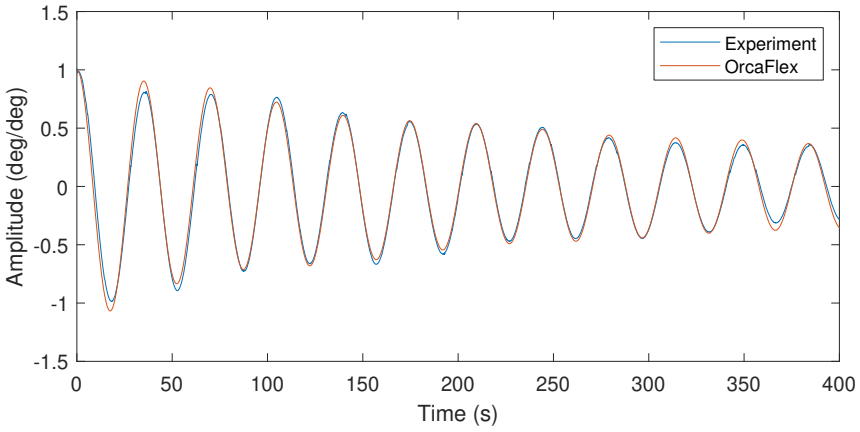

(c) Numerical and experimental decay test in pitch.

Figure 4.8: Figure (a)-(c) compares the mooring system characteristics in Orcaflex to the experimental setup in surge, heave and pich.

Table 4.4: A comparison of the full-scale eigenperiods in surge, heave, and pitch of the numerical model compared to eigenperiods from the experiment given in seconds.

DOF	**OrcaFlex**	**Experiment**
Surge	149.6	150.2
Heave	27.7	27.1
Pitch	34.9	34.9

5. Results - 3-Hour Random Sea-States

The results in this chapter are presented in full-scale values for both models. The chapter is sectioned into results for the spar-buoy and semisubmersible individually, except for comparing the RAO curves for both floaters and the extreme short-term statistics over the next two sections. The calibrated input wave spectra from Section 3.4.1 for the frequency- and time domain analysis are summarized and illustrated in Figure 5.1 in full-scale. The three sea states will be referred to as Sea 1, Sea 2 and Sea 3 in order to distinguish which sea state is studied. Sea 1 yields the lowest energy content and has a spectral peak frequency at 0.08 Hz compared to Sea 2 and 3, which has spectral peaks at 0.068 Hz and 0.058 Hz and also yields a higher energy content due to a higher significant wave height compared to Sea 1.

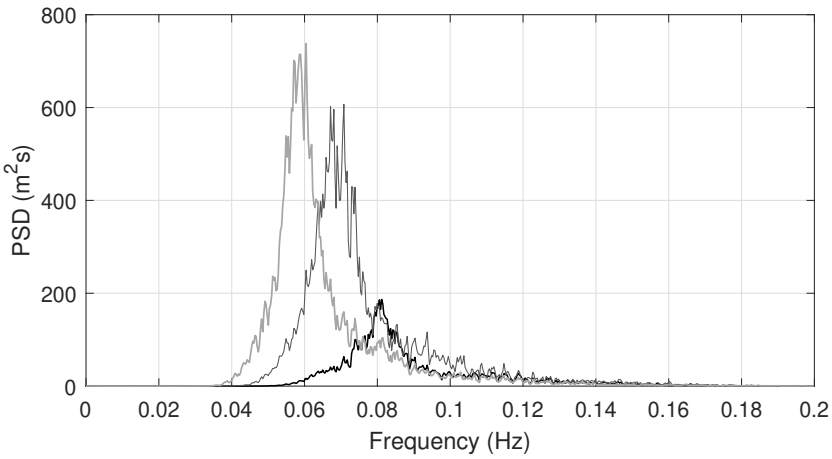

Figure 5.1: Power spectral density curve for Sea 1 defined by H_s=8 m, T_p=12.5 s in (—), Sea 2: H_s=13 m, T_p=14.6 s in (—), and sea 3 defined by H_s=13 m, T_p=17.3 s in (—).

5.1 Response Amplitude Operators

The RAO curves for both the spar-buoy and the semisubmersible in surge, heave and pitch are shown in Figure 5.2 and are computed using Sea 1. The RAO curves for both models have distinctive peaks at approximately their respective eigenfrequencies estimated from the de-

cay tests in Section 3.7. The coupling between surge and pitch motions is also observed with a small peak at pitch and surge's eigenfrequencies in each other's spectra. This is also observed for both models. However, the semisubmersible has its eigenfrequency closer to the first-order wave frequencies. This is especially the case for heave, which has an eigenfrequency at approx. 0.638 Hz, overlapping with the first order wave frequencies in all three sea states.

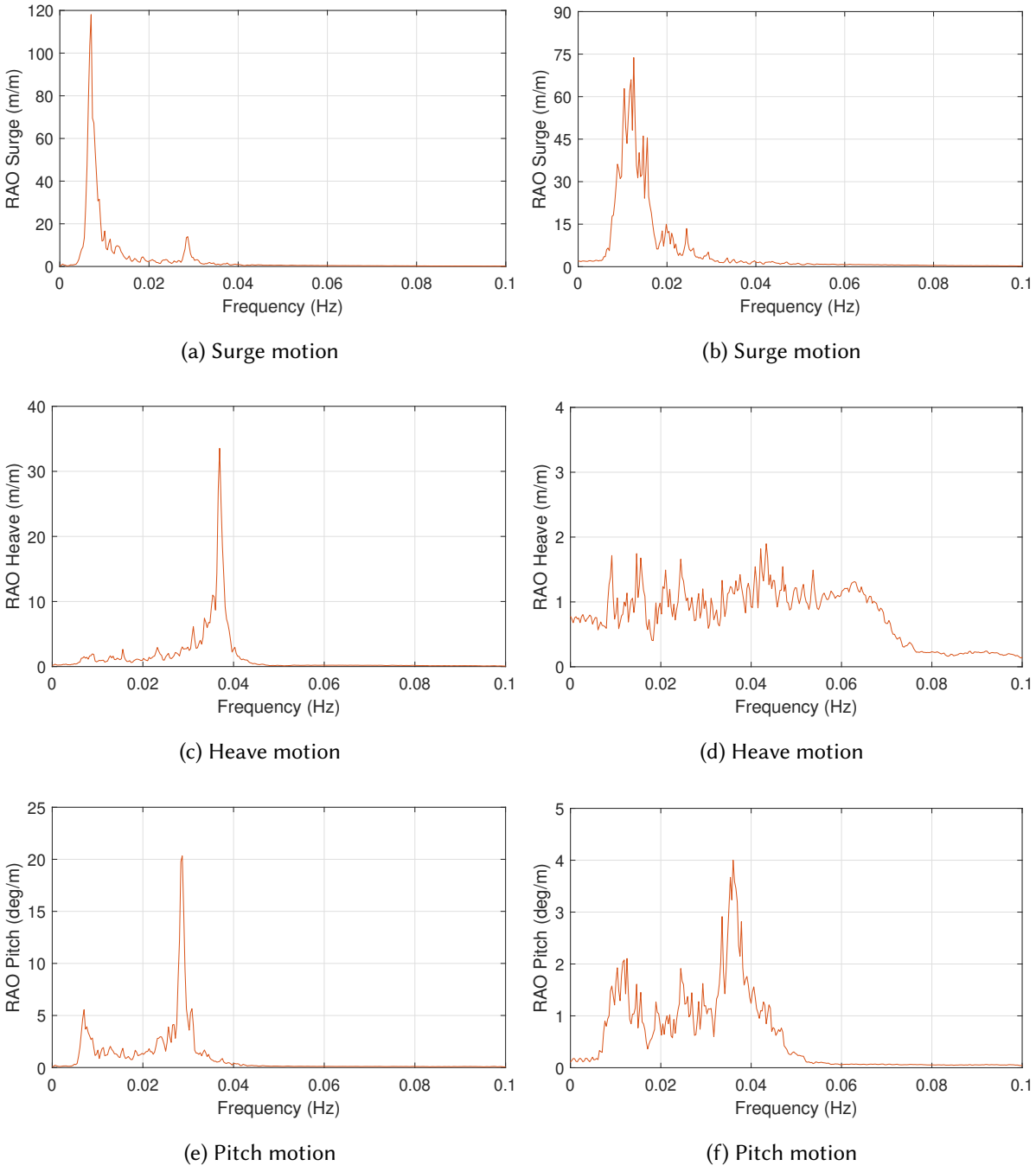

(a) Surge motion

(b) Surge motion

(c) Heave motion

(d) Heave motion

(e) Pitch motion

(f) Pitch motion

Figure 5.2: Motion amplitude RAOs in surge, heave and pitch for the spar-buoy in (a), (c) and (e), and the semisubersible in (b), (d) and (f) respectively.

Tension amplitude RAO curves for the spar buoy's mooring lines are presented in Figure 5.3a, and the semisubmersible's mooring lines are in Figure 5.3b. Both tension amplitude spectra have peaks below the first-order wave frequencies in the low-frequency area. The RAO curves for the mooring loads related to the spar-buoy have a clear peak at approximately 0.007 Hz and 0.0287 Hz, corresponding to the eigenfrequency in surge and pitch. The tension RAO for the semisubmersible's mooring lines does not have the same clear peaks but relatively high amplitudes around 0.01 Hz, with a peak on top of these at approximately 0.12 Hz. This frequency is close to the semisubmersible's eigenfrequency in surge. The same trends are observed in all three mooring lines, where lines 2 and 3 have lower amplitudes than line 1, aligned with the incoming wave direction for both models.

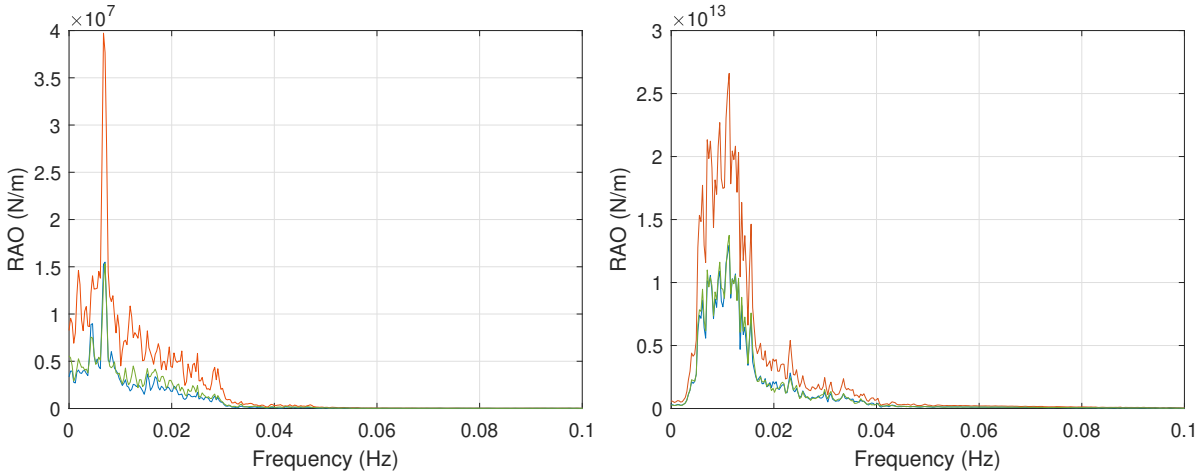

(a) Tension amplitude RAO for the spar-buoy's mooring lines.

(b) Tension amplitude RAO for the semisubmersible's mooring lines.

Figure 5.3: Tension amplitude RAOs for all three mooring lines used to position the spar-buoy in (a) and the semisubmersible in (b) presented in full-scale values. The (—) represents mooring line 1, (—) and (—) represents mooring line 2 and 3.

5.2 Short-Term Extreme Values

The extreme loads and responses during a short-term storm condition are computed through spectral analysis. The statistical parameters representing the significant response, the average of the 1/10 highest responses and the theoretical maximum response are computed for surge, heave and pitch for both models in all three sea states in Tables 5.1 and 5.2. The response statistics in surge are named x, with heave represented by z and pitch as $r2$. These tables show the extreme values increase from Sea 1 to Sea 3. This trend is observed in both

models. Additionally, the semisubmersible shows significantly greater response values in surge and heave. This floater's eigenfrequency in heave coincides with high energy amplitudes in the wave spectrum, which may induce significantly larger estimates in this degree of freedom. However, the pitch-response values are more significant for the spar-buoy despite its eigenfrequency being further from the first-order wave frequencies than the semisubmersible's eigenfrequency in this degree of freedom.

Table 5.1: Extreme values are given in full-scale for surge (x) and heave (z) given in meters, and pitch ($r2$) in degrees for the spar-buoy. The values are estimated from spectra recorded in all three sea-states.

	$\mathbf{x}_{1/3}$	$\mathbf{x}_{1/10}$	$\mathbf{x}_{max}$	$\mathbf{z}_{1/3}$	$\mathbf{z}_{1/10}$	$\mathbf{z}_{max}$	$\mathbf{r2}_{1/3}$	$\mathbf{r2}_{1/10}$	$\mathbf{r2}_{max}$
Sea 1	2.7	3.5	4.8	1.6	2.0	2.8	2.5	3.2	4.54
Sea 2	5.6	7.09	9.8	3.3	4.2	5.9	5.4	6.9	9.75
Sea 3	7.2	9.2	12.6	3.8	4.8	6.8	5.7	7.2	10.08

Table 5.2: Extreme values are given in full-scale for surge (x) and heave (z) given in meters, and pitch ($r2$) in degrees for the semisubmersible. The values are estimated from spectra recorded in all three sea-states.

	$\mathbf{x}_{1/3}$	$\mathbf{x}_{1/10}$	$\mathbf{x}_{max}$	$\mathbf{z}_{1/3}$	$\mathbf{z}_{1/10}$	$\mathbf{z}_{max}$	$\mathbf{r2}_{1/3}$	$\mathbf{r2}_{1/10}$	$\mathbf{r2}_{max}$
Sea 1	4.4	5.6	7.8	3.0	3.8	5.4	1.5	2.0	2.8
Sea 2	10.4	13.3	18.3	8.7	11.0	15.8	3.7	4.76	6.7
Sea 3	11.2	14.2	19.8	12.0	15.2	21.6	4.1	5.20	7.3

Assuming the mooring tensions follow a Rayleigh distribution, the same statistical parameters are computed using the mooring line tension spectra. These values are presented in Figure 5.4 for the spar-buoy and Figure 5.5 semisubmersible. Observable in these figures are the same tendencies as for the responses; the extreme values increase from Sea 1 to Sea 3. As expected, the short-term extreme loads in mooring line 1 are higher than in mooring lines 2, and 3 for both models as these are mounted at an angle to the incoming waves, resulting in the forces arising in these lines being shared by lines 2 and 3.

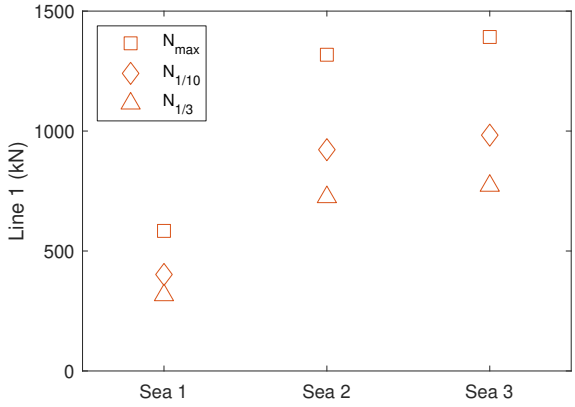

(a) Mooring line 1, spar-buoy.

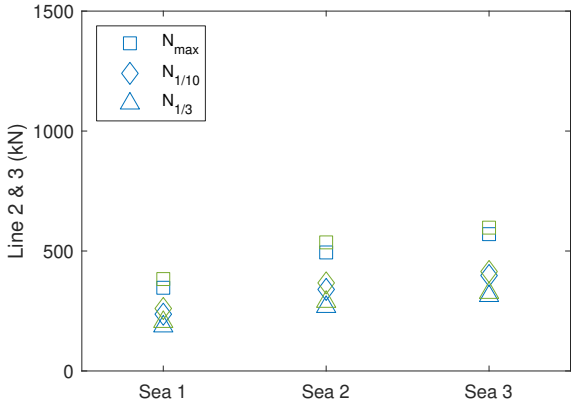

(b) Mooring line 2 and 3, spar-buoy.

Figure 5.4: Extreme statistical mooring loads in line 1 are represented by the (—) color, and mooring lines 2 and 3 in the colors (—) and (—) for the spar-buoy in all three sea-states in full-scale values.

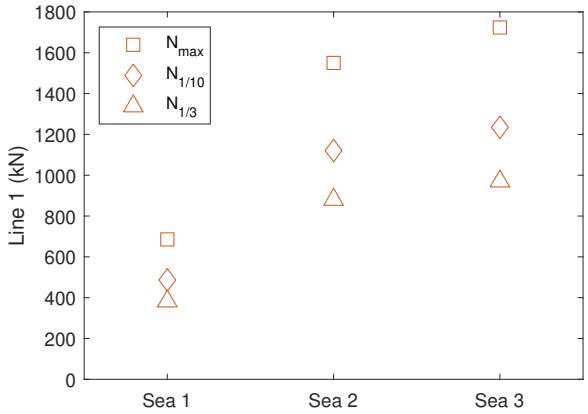

(a) Mooring line 1, semisubmersible.

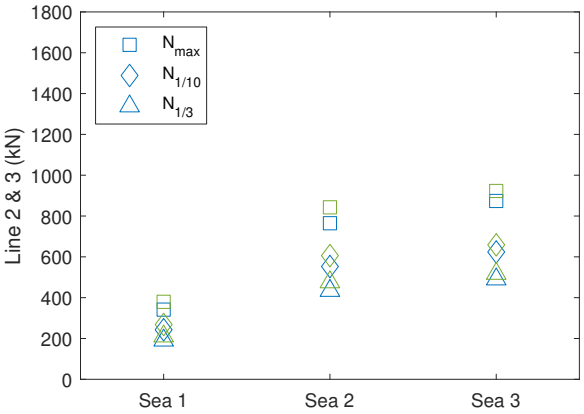

(b) Mooring line 2 and 3, semisubmersible.

Figure 5.5: Extreme statistical mooring loads in line 1 represented by the (—) color, and mooring line 2 and 3 in the colors (—) and (—) for the semisubmersible in all three sea-states in full-scale values.

Table 5.3: Extreme values in full-scale values for mooring line 1 given in kN for both FOWTs. The values are estimated from spectras recorded in all three sea-states.

	Spar-buoy			**Semisubmersible**		
	$N_{1/3}$	$N_{1/10}$	N_{max}	$N_{1/3}$	$N_{1/10}$	N_{max}
Sea 1	316.0	402.2	583.8	382.4	486.7	549.0
Sea 2	724.7	922.4	1318.1	880.4	1120.5	1228.9
Sea 3	772.2	982.9	1392.1	970.1	1234.7	1374.0

5.3 Time-Domain Results

The extreme results in the frequency domain are computed from the power spectral density curves recorded in the given sea-state and indicate the extreme statistical values. However, these demonstrate the estimated extreme values only, except given the relation between the extreme values and their related frequencies, the effects causing these are studied in the time domain.

5.3.1 Spar Buoy

The time series of the recorded mooring loads with the ten highest mooring load peaks are marked with a red circle in Figure 5.6a. The recordings are from measurements in Sea 3. The time step of when these peaks occur is used to extract the immediate response and wave elevations in the same sea-state and are marked as a red circle in Figures 5.6b and 5.7a and b. The time series are cropped to show the time interval of when the top ten mooring loads occur. The two first peaks arising at approximately 2700 s in the time series are both close in time and value and appear, therefore, as one peak in Figure 5.6a. Observed from the time series, the red circles in the wave elevations appear random and unrelated to extreme wave elevations. The mooring loads, however, appear to be linked with peaks in the surge and pitch responses in Figure 5.7.

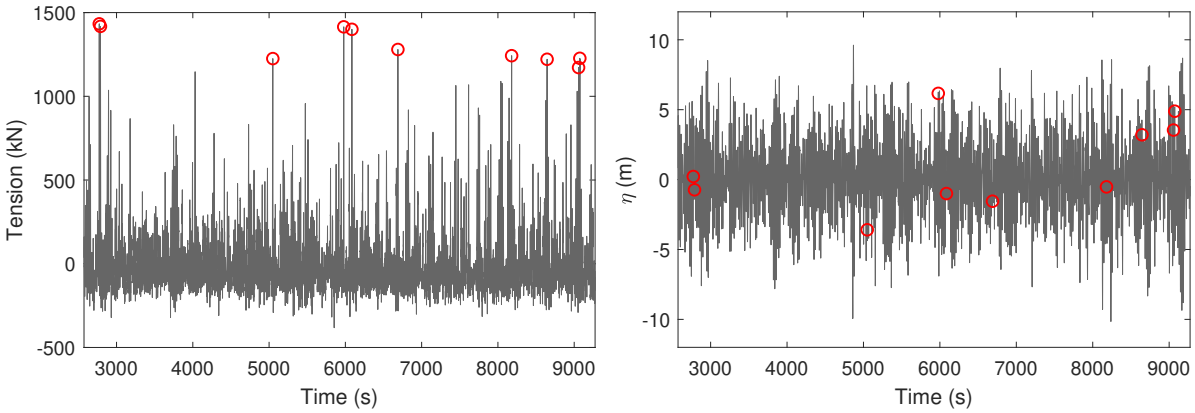

(a) Mooring tensions in line 1 recorded in Sea 3.

(b) Wave elevations recorded in sea 3.

Figure 5.6: Mooring tensions in line 1 given in (a) and wave elevations in (b) recorded in Sea 3 for the spar-buoy. The (○) marks the time of top ten mooring peaks occuring in this sea-state.

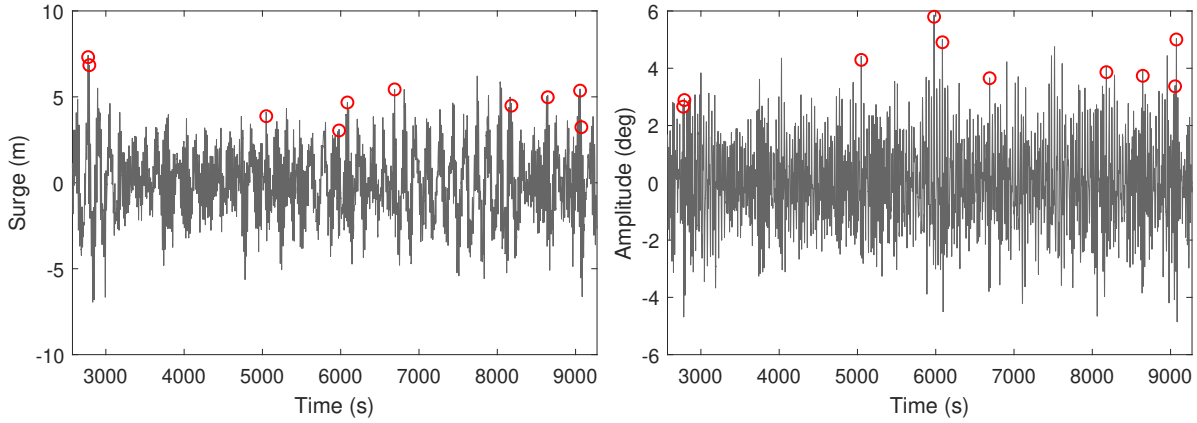

(a) Surge motions recorded in Sea 3

(b) Pitch motions recorded in Sea 3

Figure 5.7: Recorded responses in surge (a) and pitch in (b) from running Sea 3 with the spar-buoy. The (○) marks when the time top ten mooring tensions occur in this sea-state.

The top ten mooring load values are further compared to the local wave heights, wave steepness, surge, and pitch motion amplitudes for all three sea-states. Figure 5.8 illustrates the peak mooring loads compared to local wave height and local wave steepness in Sea 1 to Sea 3. Sea 1 is represented in blue, Sea 2 in red, and Sea 3 in yellow. These figures show no evident correlation between the extreme mooring loads and the local wave height and wave steepness, and these parameters are a poor fit for a linear model. In contradiction to the local wave height and wave steepness, the tensions appear linearly related to the responses in surge and pitch. Therefore, a linear regression model is used to explain the variation in the data and is represented by a black line in Figure 5.8. This is also computed to study an eventual coherence between the slope of the fitted line and mooring stiffness. To evaluate the goodness of fit of the linear model, the coefficient of determination, R^2, is used in this thesis utilizing the formulation from [56], given as:

$$R^2 = 1 - \frac{SSE}{SST},$$

where SSE is a value computed by taking the summation of the difference between the recorded mooring tensions and the tension values predicted by the linear model squared. SST is the total sum of squares of the mooring tensions multiplied by the variance of the same data samples minus one. The results from fitting a linear model to the mooring tensions and the spar buoys motions are summarized in Table 5.4 and illustrated in Figure 5.8. The R^2 value for relating mooring tensions and surge motions yielded an approximately 60% good

fit, compared to an 81.7% fit for the linear regression model for pitch motions. The latter results indicate that the variations in mooring loads for the spar-buoy can be well predicted by a linear model using motions in pitch. The slope of the fitted data in Figure 5.8a is 115.1 kN/m compared to the mooring stiffness approximated to 80.4 kN/m in Section 3.3.

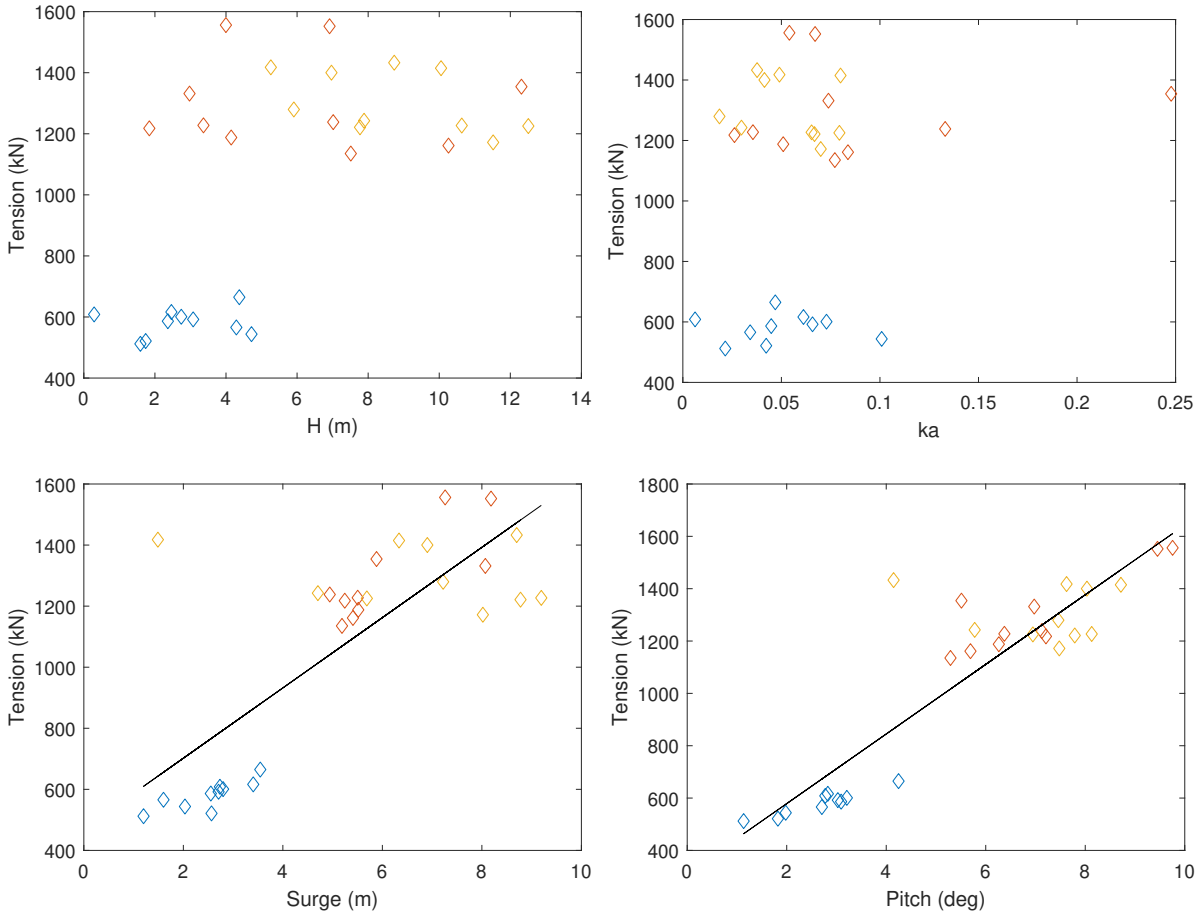

Figure 5.8: Top ten peak tensions in mooring line 1 compared to local wave heights in (a), local wave steepness in (b), motions in surge in (c) and pitch in (d) for the spar-buoy. Measurements from Sea 1 is presented in (—), Sea 2 in (—) and Sea 3 in (—) with the linear model in (—).

Table 5.4: Results from fitting a linear regression model to mooring tensions compared to motion amplitudes in surge and pitch for the spar-buoy in all three sea-states.

	Linear fit	R^2 (%)
Surge	y= 115.1x+471.8	59.9
Pitch	y= 133.0x+312.8	81.7

The top ten tensions recorded in Sea 3 is summarized in Table 5.5 with the local wave height, wave steepness, motions in surge, and pitch for the spar-buoy. This table is included as Sea 3 is used as the background sea in the MLW and CRRW definitions in Chapter 6. In this table, the maximum pitch response coincides with the maximum recorded mooring tension, which is not the case for the other parameters studied in this sea-state. The same tables for Sea 1 and 2 are included in Appendix A.

Table 5.5: Top ten mooring tensions with corresponding time stamp, local wave height, wave steepness, surge and pitch motions recorded in Sea 3.

Time [s]	N [kN]	H [m]	ka [∼]	Surge [m]	Pitch [deg]
2773.6	1432.8	8.7	0.037	8.7	4.1
2789.0	1417.7	5.3	0.049	1.5	7.6
5049.0	1225.3	12.5	0.079	5.7	6.9
5978.8	1414.9	10.1	0.080	6.3	8.7
6085.7	1400.1	7.0	0.041	6.9	8.0
6688.7	1279.6	5.9	0.019	7.2	7.5
8179.9	1242.6	7.9	0.030	4.7	5.8
8644.6	1221.2	7.8	0.067	8.8	7.8
9057.4	1171.8	11.5	0.070	8.0	7.5
9073.9	1227.0	10.6	0.065	9.2	8.1
Mean	1303.3	8.7	0.054	7.0	7.2

The mooring lines are mounted with a pre-tension value recorded to be 35 kN in full scale in mooring line 1. Using the criteria from Section 2.9, most of the mooring loads for the spar-buoy follow a slack event and are, from this definition, defined as snap loads. The frequency of occurrence of the snap loads demonstrates the number of snap loads with a given magnitude, which is presented in Figure 5.9 for all three sea-states. Here, the pre-tension value and the static tension, defined as the mean value of the total peak tensions, are used to define a snap load. The total number of snap loads defined in Sea 1 is 221, compared to Sea 2 and 3, where the total are 213 and 208. The corresponding static tensions are 187.5 kN, 341.5 kN, and 338.3 kN, respectively. Most of the snap loads defined in Sea 1 are between 187.5 and 300 kN, whereas in seas 2 and 3, most snap loads are higher and most frequently in a magnitude of approximately 350 to 800 kN.

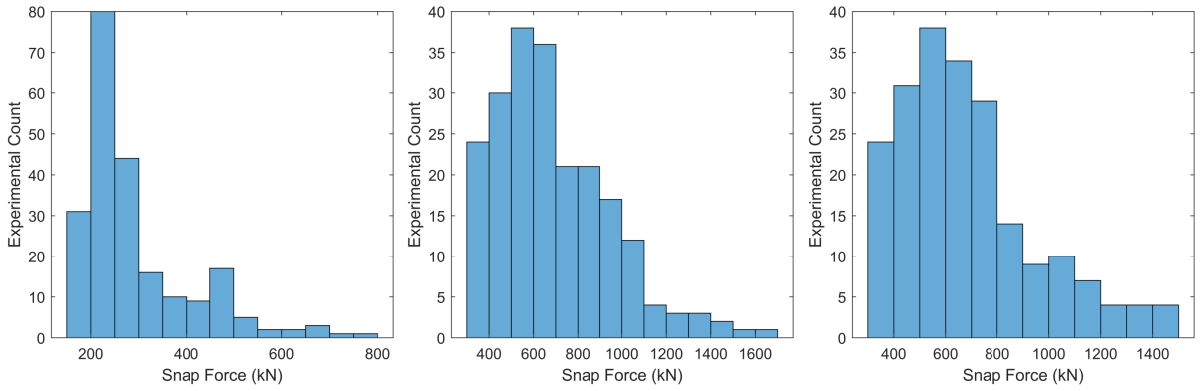

(a) Sea 1 (b) Sea 2 (c) Sea 3

Figure 5.9: Frequency of occurence of a snap load against snap force in all three sea-states. where the total number of snap loads defined in (a) 221, (b) 213, and (c) 208.

In realistic mooring systems, these loads are beneficial to avoid. Therefore, assessing how frequently these loads exceed the static load and how much greater the static loads should be to reduce the size and number of snap loads is useful. Therefore, the snap forces normalized by the static tension are presented in Figure 5.10. Observed in this figure is approximately 65% of the snap loads in Sea 1 being 1-1.5 times greater than the static tension compared to Sea 2 and 3, where 29% and 31% snap loads are 1.5-2 times the static tension. Assuming the mooring systems behave as linear systems, by multiplying the static tension by 2.5 in Sea 1, the number of snap loads reduces by approx. 88%. By tripling the static tension in Sea 2 and 3, the number of snap loads in these sea states reduces by 88.7% and 87.5%, respectively. However, the system is likely nonlinear in events such as snap loads and as the mooring lines are quite slack.

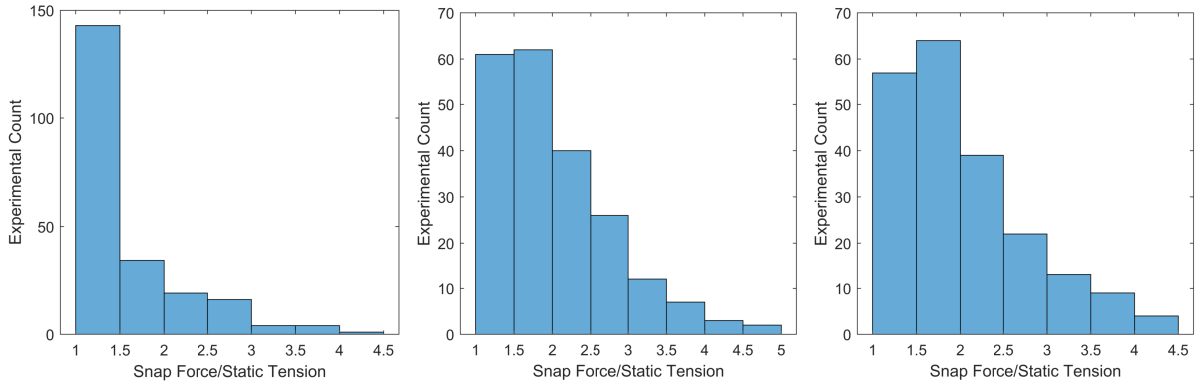

(a) Sea 1, static tension = 187.5 kN (b) Sea 2, static tension = 341.5 kN (c) Sea 3, static tension = 338.3 kN

Figure 5.10: Frequency of occurrence of a snap load in mooring line 1 in all three sea-states normalized by the static tension.

5.3.2 Semisubmersible

The time series of the recorded mooring loads for the semisubmersible in Sea 3 with the ten highest tensions peaks are marked with a red circle in Figure 5.11a. Six out of ten tension peaks arise towards the end of the recordings, where five peaks are between 8000-1000 s. The time step of when the tension peaks transpire is marked as a red circle in the wave elevation series, motion amplitudes in both surge and pitch. The mooring tension peaks coincide with peak responses in surge and are less coherent with motion amplitudes in pitch compared to the spar-buoy. However, some coherence with pitch is observed.

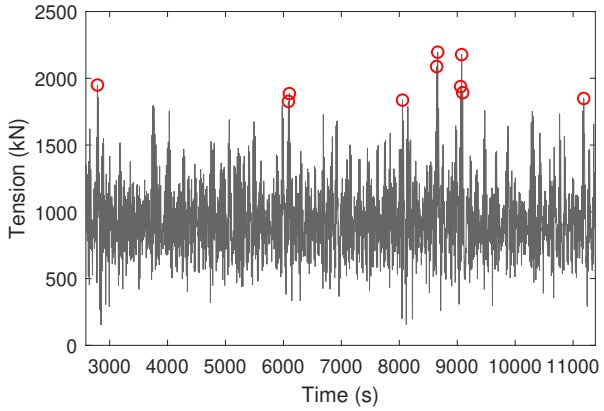

(a) Mooring tensions in line 1 recorded in Sea 3.

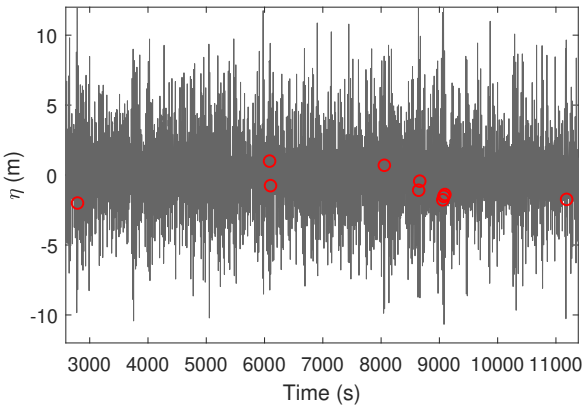

(b) Wave elevations recorded in Sea 3.

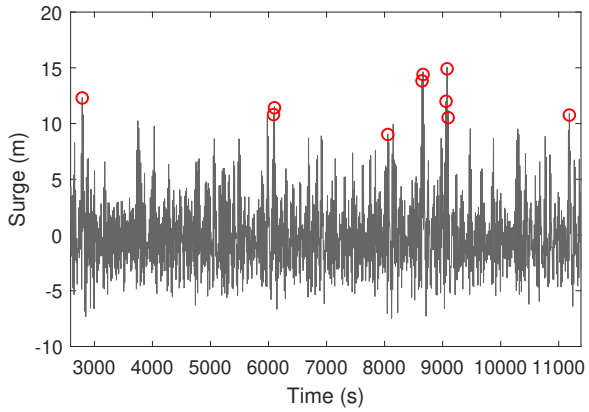

(c) Surge motions recorded in Sea 3

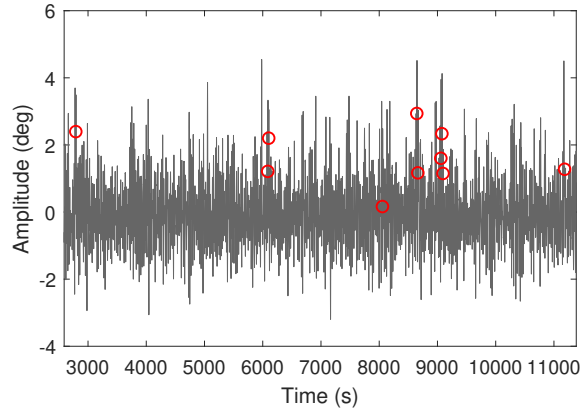

(d) Pitch motions recorded in Sea 3

Figure 5.11: Recorded mooring tensions in line 1 given in (a) and wave elevations in (b) surge motions in (c) pitch motions in (d) recorded in Sea 3 for the semisubmersible. The (○) marks the time of the top ten mooring peaks occurring in this sea-state

Tensions in mooring line 1 and responses in surge between 8500 - 9200 s with the top five mooring loads recorded in Sea 3 are marked as red circles in Figure 5.12. The top five peak loads occur approximately at 8663 s in the series, at the same time as the model appears to be drifting, as depicted in Figure 5.12. Additionally, the same figure shows how tensions in mooring line 1 follow the motion amplitudes in surge. It also appears to be a slow-drift motion with a frequency of approx. 0.01 Hz, close to the semisubmersible eigenfrequency in surge. The more rapid oscillations imposed on the slow-drift motion oscillate with two frequencies, approx. 0.037 Hz and 0.068 Hz, close to the eigenfrequencies in pitch and heave. The second largest tension arises at approx. 9076 s in the time series and do not appear to be related to motions in surge. From Table 5.7 this peak coincides with the highest wave in this table in addition to a steeper wave compared to the wave emerging at the maximum tension event.

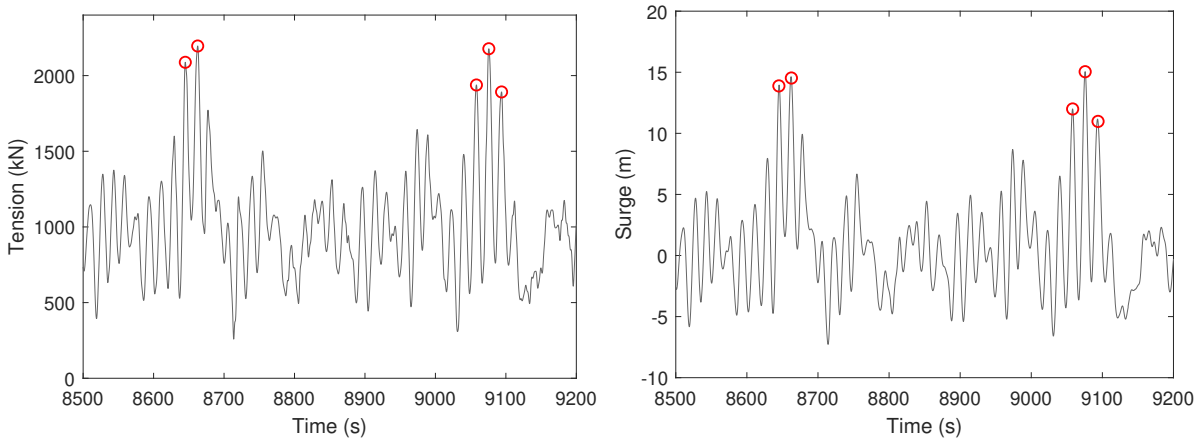

Figure 5.12: Cropped time series of tension in mooring line 1 (left) and motions in surge (right) (—)

The top ten mooring tensions are also defined from tests with the semisubmersible. These are presented in Table 5.7 with the local wave height, wave steepness, and local responses in surge and pitch recorded in all three sea-states. The top ten mooring loads are also compared to the local wave height and steepness in Figure 5.13a and b, and the response in surge and pitch in Figure 5.13c and d. Similar to Section 5.3, a linear regression model is used to explain the variation in the data given in Table 5.7, and is represented as a black line in Figure 5.13. The coefficient of determination is computed and included in Table 5.6 with the linear regression model. Similar to the spar-buoy, the mooring tensions appear to have minimal correlation with the local wave steepness. However, the R^2 indicates a relatively good fit for

a linear model describing the relation between tensions and the local wave height and response in pitch, where the best fit is with the data set with mooring tension and the recorded response in surge.

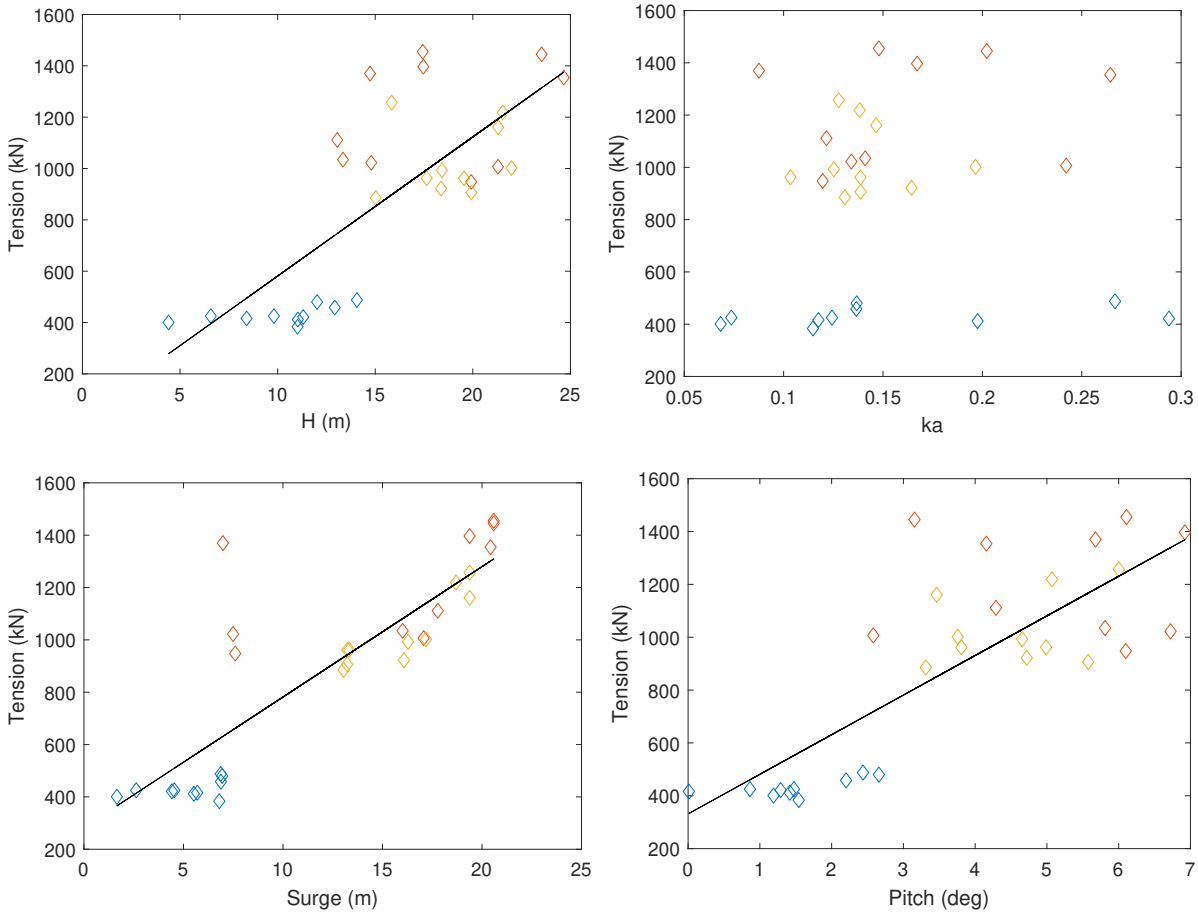

Figure 5.13: Top ten peak tensions in mooring line 1 compared to local wave heights in (a), local wave steepness in (b), motions in surge in (c), and pitch in (d). Measurements from Sea 1 is presented in (—), Sea 2 in (—) and Sea 3 in (—) with the linear model in (—).

Table 5.6: Results from fitting a linear regression model to mooring tensions compared to wave heights and motions in surge and pitch for the semisubmersible in all three sea-states.

	Linear fit	R^2 (%)
Wave Height	y=54.2x+39.0	56.7
Surge	y=49.8x+283.3	71.8
Pitch	y=149.9x+331.3	63.1

However, none of the top tension peaks follows a slack event. Using the criteria given in Section 2.9, a slack condition is defined for mooring line 1 as a tension recorded less than 94.5 kN. As the lowest tension recorded in Sea 3 is 153.2 kN, no loads are defined in the recordings of the tensions arising in mooring line 1 for the semisubmersible's mooring system. As the recorded tensions in lines 2 and 3 are significantly lower, the same tendency is also assumed in these mooring lines.

Table 5.7: Top ten mooring tensions with corresponding time stamp, local wave height, wave steepness, surge, and pitch motions recorded in Sea 3.

Time [s]	N [kN]	H [m]	ka [∼]	Surge [m]	Pitch [deg]
2790	1949.2	22.0	0.197	17.2	3.8
6086	1827.2	15.0	0.131	13.1	3.3
6102	1885.3	17.6	0.139	13.2	3.8
8055	1836.3	18.4	0.164	16.1	4.7
8645	2087.9	21.3	0.147	19.4	3.5
8663	2195.6	15.9	0.128	19.4	6.0
9058	1938.0	18.4	0.125	16.3	4.7
9076	2177.5	21.5	0.138	18.7	5.1
9094	1892.0	19.6	0.104	13.3	5.0
11183	1848.8	19.9	0.139	13.2	5.6
Mean	1963.8	19.0	0.141	16.0	4.6

5.4 OrcaFlex

This section presents results from numerical analyses in OrcaFlex and compares these to experimental results in Section 5.1 and 5.2. The same sea-states are used in OrcaFlex for 10800 s, representing a 3-hour sea-state. A ramp-up time of 100 s to allow the sea to be fully developed and transients to settle before the 3-hour sea is included. The time series are not directly compared between OrcaFlex and the experiment in the time domain as the seed number used in generating the random sea is different. Therefore the phases and formation of wave groups and other effects will differ, and results from the frequency domain are the only results compared.

Figure 5.14 display the motion amplitude RAOs in surge, heave, and pitch and the tension RAO in line 1 generated in OrcaFlex in Sea 1 compared to the experimental curves from Section 5.1. All RAO curves are normalized using their maximum amplitude as their frequencies are of interest and not the amplitudes themselves. The recorded peak frequencies are given in Table 5.8 where the agreement is closest for surge and mooring line 1 with approx. 2.6% deviation in heave. The numerical RAO curve in pitch has three peaks around the experimental eigenperiod, where the highest peak has a frequency of approx. 3.2% larger than the floater's experimental eigenperiod.

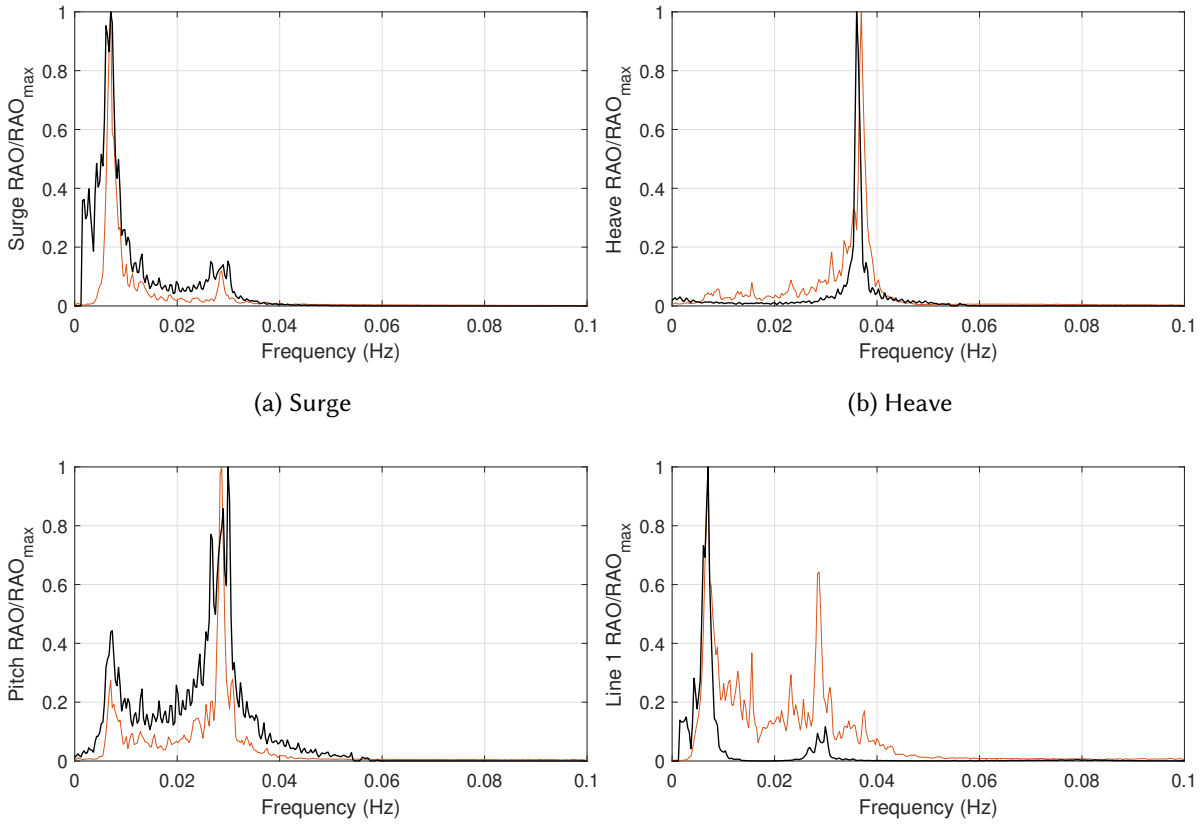

(a) Surge (b) Heave

(c) Pitch (d) Line 1

Figure 5.14: Comparison of motion amplitude RAOs recorded in (a) surge, (b) heave, (c) pitch, and (d) tension RAOs for line 1 with numerical results in (—) and experimental results in (—) Sea 1.

Table 5.8: Numerical and experimental eigenperiods in seconds estimated from RAO curves from OrcaFlex in surge, heave, pitch, and mooring line 1.

	Surge	**Heave**	**Pitch**	**Line 1**
OrcaFlex	149.3	27.8	36.0	149.2
Experiment	149.6	27.1	34.9	149.5

The short-term extreme values are included in Table 5.9 where the overall extreme values are lower than the experimental values in Table 5.1. This is also observed in Table 5.10 for mooring tensions. The extreme values are also largest in Sea 2 compared to experimental results were these increase in magnitude from Sea 1 to Sea 3.

Table 5.9: Extreme values for motions in surge (x) and heave (z) given in m, and pitch ($r2$) in degrees for the spar-buoy. The values are estimated from spectras recorded in all three sea-states in OrcaFlex.

	$\mathbf{x}_{1/3}$	$\mathbf{x}_{1/10}$	$\mathbf{x}_{max}$	$\mathbf{z}_{1/3}$	$\mathbf{z}_{1/10}$	$\mathbf{z}_{max}$	$\mathbf{r2}_{1/3}$	$\mathbf{r2}_{1/10}$	$\mathbf{r2}_{max}$
Sea 1	1.61	2.04	2.30	0.03	0.04	0.05	0.49	0.63	0.84
Sea 2	4.10	5.22	5.75	0.12	0.15	0.20	1.16	1.48	1.97
Sea 3	3.68	4.68	5.23	0.23	0.29	0.39	1.23	1.58	2.12

Table 5.10: Extreme values in full-scale values for mooring line 1 given in kN in all three sea-states.

	$\mathbf{N}_{1/3}$	$\mathbf{N}_{1/10}$	$\mathbf{N}_{max}$
Sea 1	71.9	91.4	106.2
Sea 2	187.1	238.2	273.3
Sea 3	171.7	218.5	259.7

6. Results - Conditional Waves

This chapter is outlined to include the method for computing MLRW and CRRW as these wave definitions need experimental results from chapter 5 in determining these. This chapter presents the results using MLWs, MLRWs, and CRRWs for both the spar buoy and semisubmersible and compares the results from the 3-hour sea-states.

6.1 Most Likely Response Wave (MLRW)

MLRW is a single wave group designed with properties to excite extreme response in a specific degree of freedom of the structure in question. As this wave definition is based on the floater's characteristics, the transfer functions and phase angles needed for the wave definition are computed from the recorded responses during the white noise test. Different MLRW profiles are computed to excite extreme response in surge for both the spar buoy and the semisubmersible, in addition to inducing an extreme response in pitch for the semisubmersible.

The transfer functions and phase-angles between the incident waves and recorded responses are computed through a spectral analysis of the recorded time series using a Fast Fourier Transform (FFT) technique, as explained in Section 2.3.2. The response spectrum is computed using the cross-correlation function using Eq. 2.18, while the input wave spectrum is computed based on the autocorrelation function using Eq. 2.16. This results in a complex transfer function where the phase-angles are computed using Eq. 2.20. As the white noise test only generates wave frequencies between 0.3-2 Hz, the phase angles are zero outside this frequency interval, whereas the complex transfer function is considered from 0-3 Hz. The resulting transfer functions and related phase angles for surge motions for the spar buoy and semisubmersible are depicted in Figure 6.1.

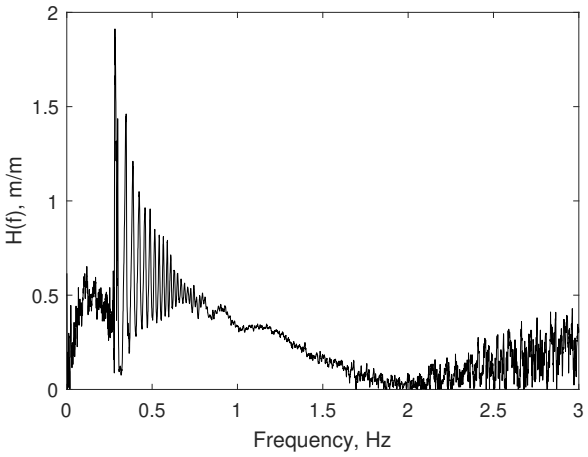

(a) Complex transfer function in surge (spar buoy).

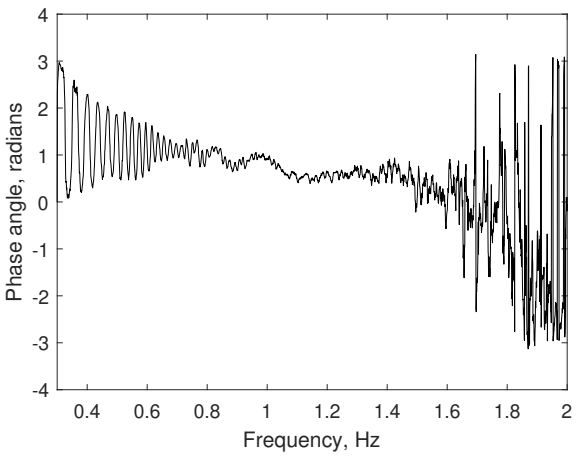

(b) Related Phase-angles to (a).

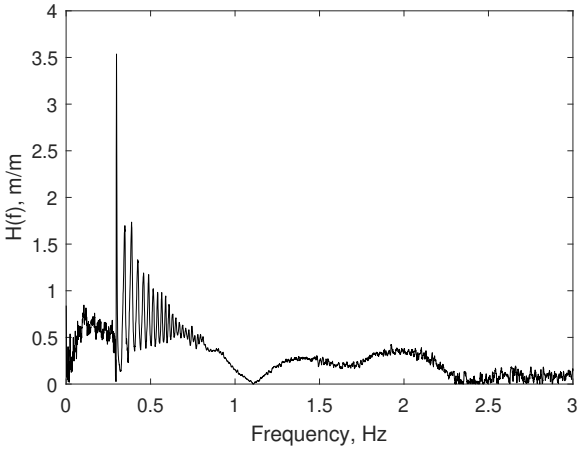

(c) Complex transfer function in surge (Semi)

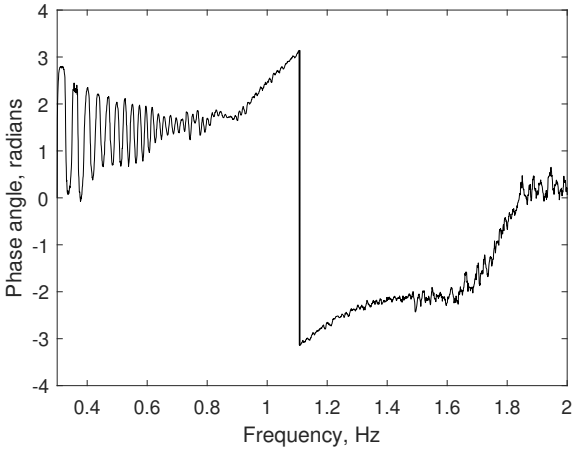

(d) Related Phase-angles to (c).

Figure 6.1: Figure (a) and (b) is the computed transfer function and related phase-angles of the spar buoy's response in surge, (c) and (d) the computed transfer function and related phase angles for the semisubmersible in surge, all from the white noise test.

The transfer function and its related phase-angles for the semisubmersible's responses in pitch are computed using the same methods as previously formulated, except the input wave spectrum for pitch is scaled using Froude's scaling to represent a full-scale wave spectrum. This is due to the response amplitudes in pitch being equal in both model- and full-scale. Therefore, using the model-scale wave spectrum will result in an unrealistically high estimate of the responses in pitch. Using the transfer functions and phase-angles computed for the individual degree of freedom for both floaters, the MLRW profile is derived using the formulations given in Section 3.4.2. The input response amplitude used in the definition of these wave profiles is summarized in Table 6.1 for surge for both floaters and pitch for

the semisubmersible only. This response value is the expected maximum response amplitude generated by this wave profile. This input response-value is defined from the maximum recorded response amplitude recorded in the 3-hour sea state characterized by $H_s = 0.13$ m and $T_p = 1.73$ s.

Table 6.1: Response amplitudes used as input values in the MLRW definition for both FOWTs recorded in $H_s = 0.13$ m and $T_p = 1.73$ s given in model-scale values.

	Spar buoy	Semisubmersible
$a_{\eta,surge}$	0.0742 m	0.0935 m
$a_{\eta,pitch}$	$\sim$	5.56°

As the CRRW realization is an MLRW wave profile embedded in a random background sea, the length of the MLRW and CRRW time series is set to be 400 s long for the same reasons the MLW time series explained in Section 3.4.2. The MLRW definition computed to excite a maximum response in surge for the spar buoy is presented in Figure 6.2. The MLRW realizations for maximum response in surge and pitch for the semisubmersible are presented in Figure 6.3. As expected, the wave amplitudes for the three different realizations vary as the transfer functions, and phase-angles used in the MLRW definitions differ as these uniquely describe the relationship between the response in a degree of freedom and the incident wave. Therefore, the phases and amplitudes in the MLRW profile diverge correspondingly.

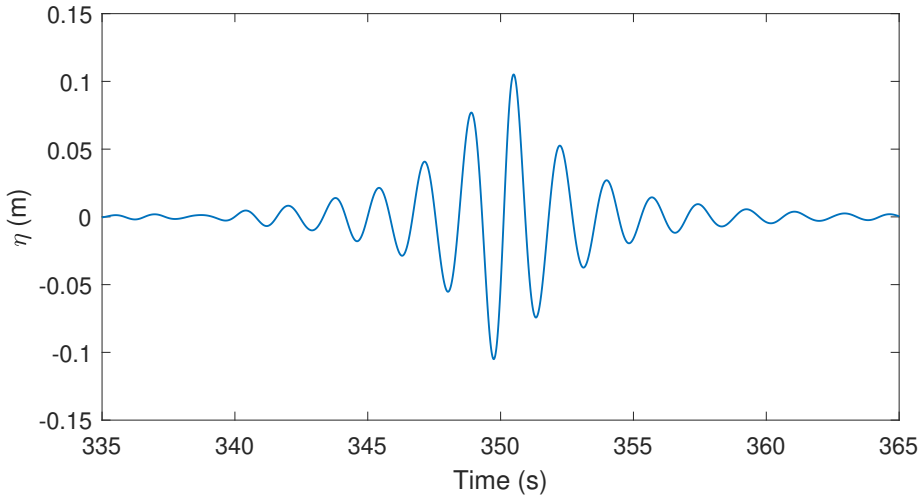

Figure 6.2: Cropped time series of the theoretical MLRW profile computed to induce an extreme response in surge for the spar buoy foundation. The time series are cropped to show the MLRW realization around the focal time set to 350 s in the 400-second long time series.

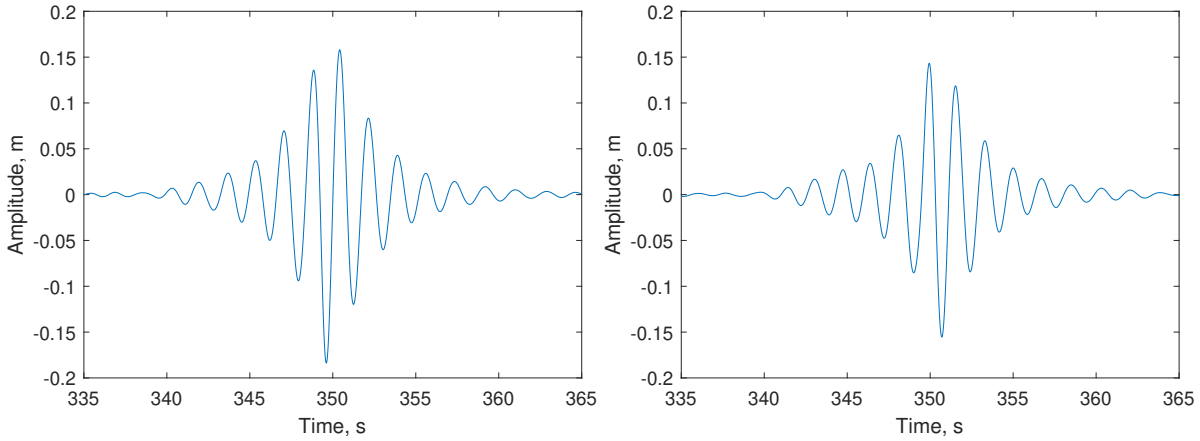

(a) The MLRW series conditioned on surge. (semi)

(b) The MLRW series conditioned on pitch (semi).

Figure 6.3: Figures (a) and (b) are cropped time series of the theoretical MLRW profile computed to induce a maximum response in surge and pitch, respectively, for the semisubmersible foundation. The time series are cropped to show the MLRW realization around the focal time set to 350 s in the 400 s long time series.

6.2 Conditional Random Response Wave (CRRW)

The CRRW definition is computed by adding the MLRW time series to a background sea-state using Eq. 2.37. The random background sea used in the definition of the CRRW profile is the same irregular sea-state used in the MLW profile in Section 3.4.2: Sea 3 defined by $H_s = 0.13$ m and $T_p = 1.73$ s. Figure 6.4a illustrates the theoretical CRRW profile designed to excite maximum response in surge for the spar buoy floater compared to the random background sea. Observable in this figure is again a difference between the CRRW and the background sea around the focal time, and the time series being identical elsewhere.

The CRRW series designed for inducing an extreme response in surge and pitch is for the semisubmersible presented in Figure 6.4. From the three realizations of the CRRW series, it can be observed that the wave group at the focal time (at 350 s) differs greatly. However, all three series are identical up to 335 s and from 360 s in both CRRW and the random background sea.

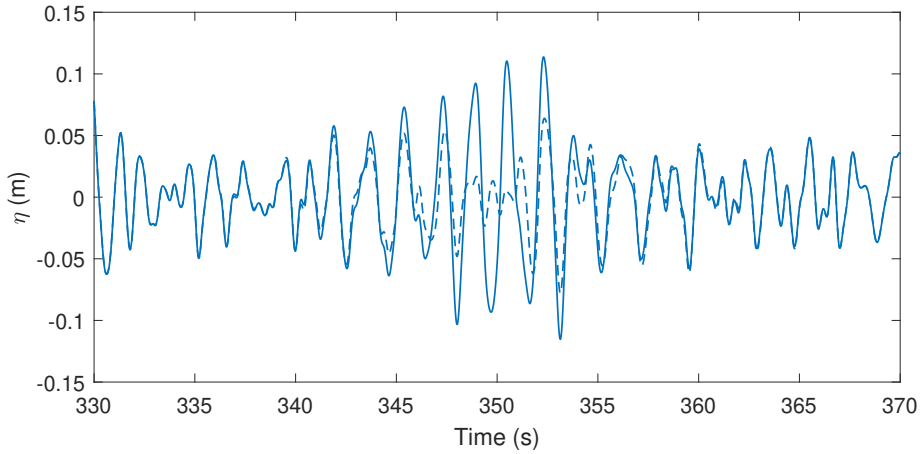

(a) The CRRW series conditioned on surge (spar buoy)

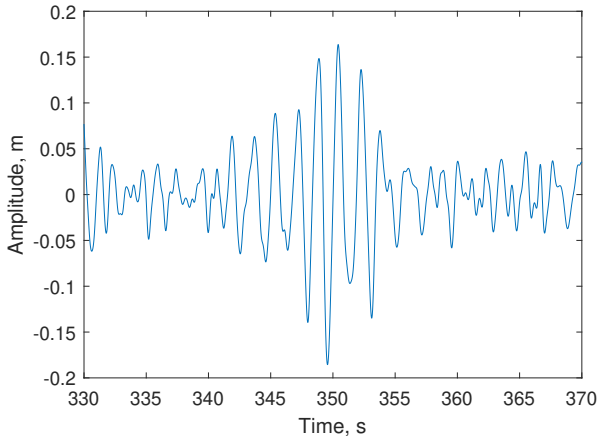

(b) The CRRW series conditioned on surge (semi)

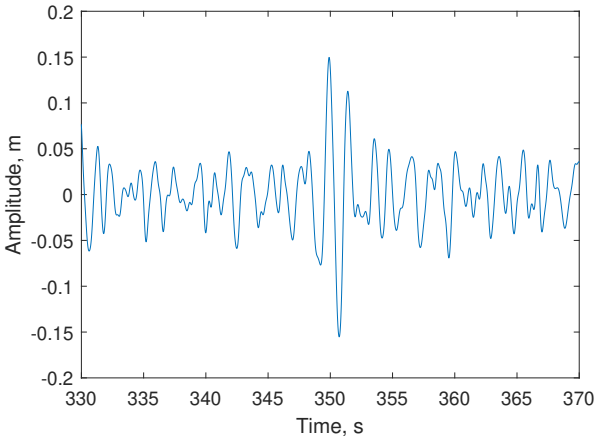

(c) The CRRW series conditioned on pitch (semi).

Figure 6.4: Figures (a), (b), and (c) is the cropped time series of the theoretical CRRW profile computed to induce a maximum response in surge and pitch, respectively, for the spar buoy in (a) and the semisubmersible in (b) and (c). The time series are cropped to show the CRRW realization around the focal time set to 350 s in the 400 s long time series.

6.3 Calibration of MLRW and CRRW

The MLRW and CRRW definitions are calibrated using the same methodology for the MLW profile explained in Chapter 3, Section 3.6.2. Here, the frequency-dependent wave amplitudes in the MLRW profile and the stochastic background sea are individually multiplied by a frequency-dependent gain factor before the two wave definitions are added together using Eq. 2.37. Since this wave definition do not consist of a single focused wave that arises at the focal time, the focus is therefore on the formation of the wave group consisting of three peaks around the focal time, approximately between 348 - 353 s.

An illustration of the recorded CRRW series during calibration is compared to the theoretical wave profile in Figure 6.5. The time series presented in this figure is the CRRW designed based on the transfer function in surge for the spar buoy. Here it can be observed that a second gain correction results in a better fit compared to no gain correction and one gain correction. The computed RMSE-values is included in Table 6.2. The wave runs with no gain correction results in the lowest RMSE value. However, observable from the time series is that this wave definition is no longer the best fit of the three wave runs of the CRRW. One gain correction results in an RMSE-value of 0.0212 m and whereas a second gain correction results in an RMSE-value of 0.0186 m and is observable as a better fit of the three runs.

Table 6.2: RMSE-values in meters for measured wave elevations of MLRW and CRRW conditioned on the response in surge for the spar buoy during calibration

Wave Definition	RMSE_{MLRW}	RMSE_{CRRW}
Gain 0	0.0089	0.0145
Gain 1	0.0093	0.0212
Gain 2	0.0105	0.0186

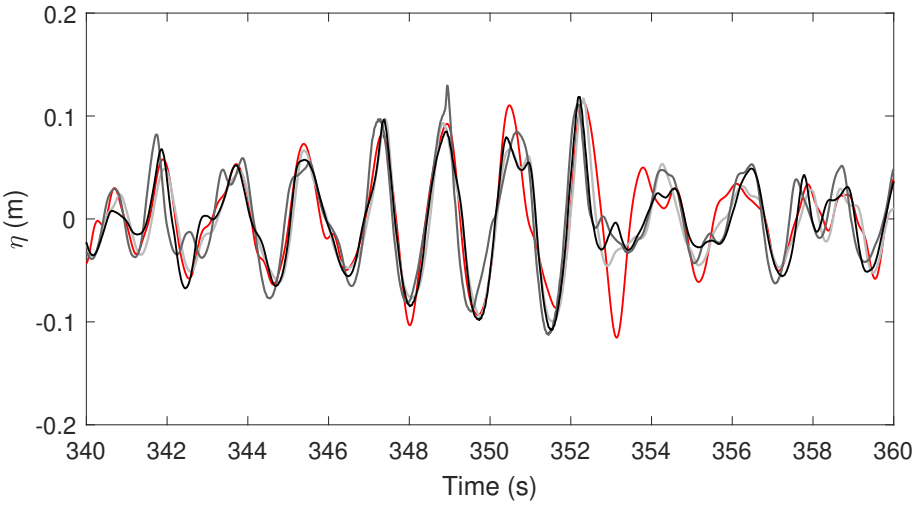

Figure 6.5: Results from the calibration of CRRW time series where: (—) is the target, (—) is without gain correction, (—) is after one gain correction, and (—) after two gain corrections designed to excite maximum response in surge for the spar buoy.

As for the MLRW series, this wave definition is used individually and in the definition of the CRRW series. Therefore, this wave definition is calibrated using the same methodology described, independent of the CRRW. The RMSE-value is again computed from the recorded

wave series during the calibration to give an estimate of the accuracy of the simulated wave series compared to the theoretical definitions. The calibrated wave spectra of all CRRW and MLRW definitions for the spar buoy and semisubmersible are included in Appendix B.

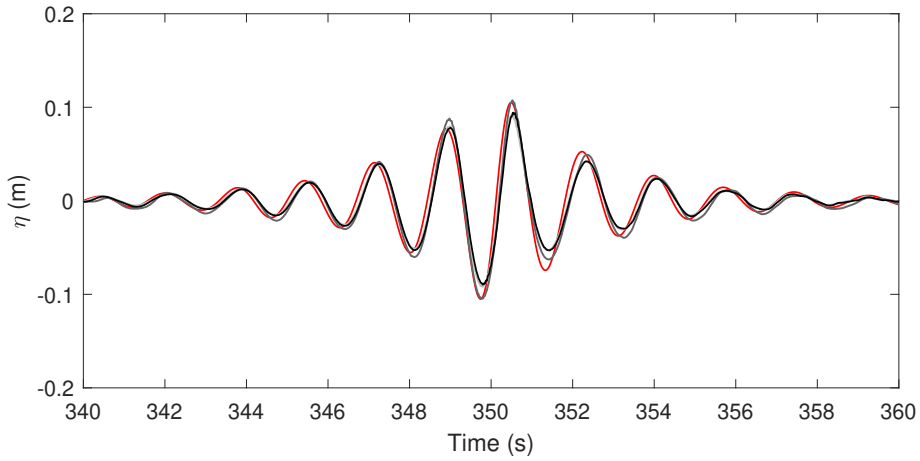

Figure 6.6: Results from the calibration of MLRW time series where: (—) is the target, (—) is without gain correction, (—) is after one gain correction, and (—) after two gain corrections designed to excite maximum response in surge for the spar buoy.

6.4 Repeatability

Three runs of MLW, MLRW, and CRRW are repeated in the wave tank with the spar buoy present to study the repeatability of wave generation and the resulting response and mooring loads. As a measure of similarity, the RMSE-value of the last two runs compared to the first run of the individual wave series is computed and presented in Table 6.3. This is computed over the full-time series. Figure 6.7 shows three measured wave series of MLW in three 20 s intervals: one at the beginning of the series, the middle, and the last around the focal time. The similarity between the first wave run and the following two runs appear quite similar, which are complemented by an average RMSE-value of 0.005 m.

Figure 6.8 depicts recorded wave elevations of MLRW and CRRW elevations around the focal time at 350 s. The MLRW and CRRW definitions are designed to excite extreme response in surge based on spar buoy's characteristics. Equal to the measured wave elevations of the MLW in Figure 6.7, both MLRW and CRRW demonstrate a good level of similarity between all three wave runs generated in the tank. This extends to the recorded mooring loads in line 1 and surge response in Figure 6.8b and c. The summarized RMSE-values of the mea-

sured wave elevations, response in surge, and mooring loads are presented in Table 6.3 for all three wave definitions. The overall RMSE values are low, and the wave series are considered repeatable.

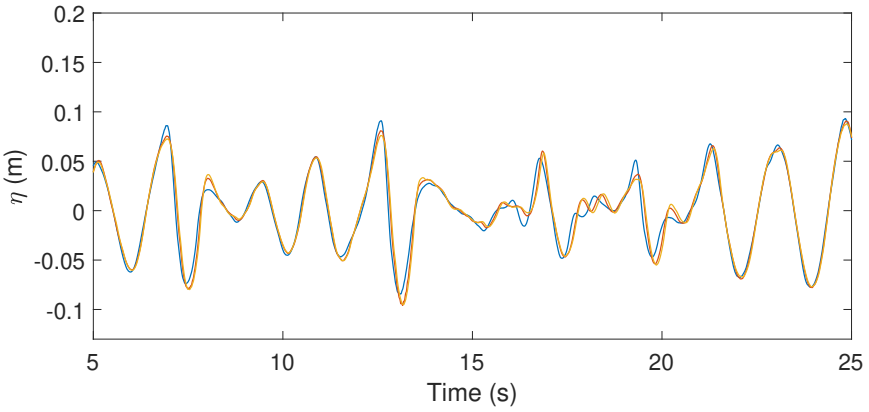

(a) 5 to 25 s.

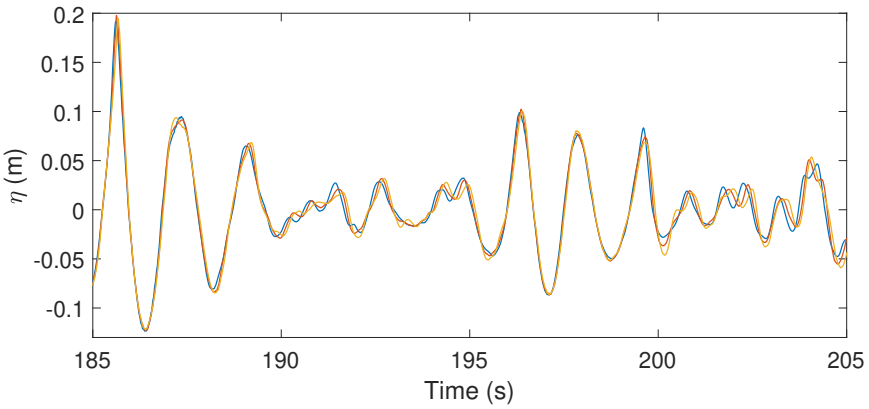

(b) 185 to 205 s.

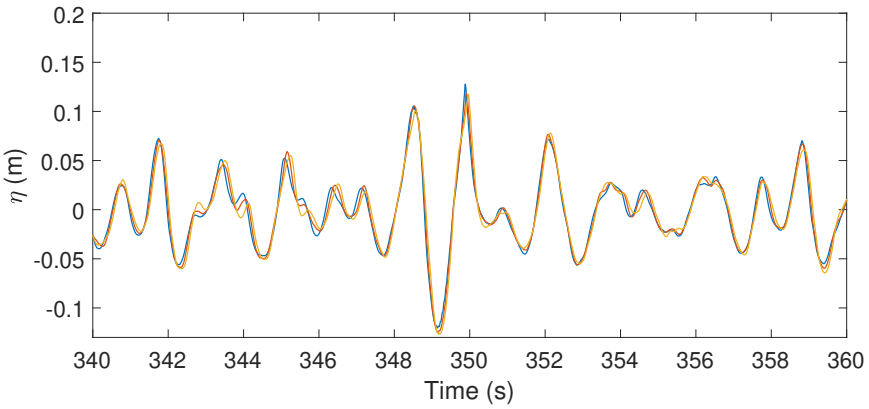

(c) 340 to 360 s.

Figure 6.7: Figure (a)-(c) demonstrating the repeatability of the wave generation of MLW where measured wave elevations at three different 20 s interval along the 400 s long time series, where (—) is the first run, (—) second, and (—) third run.

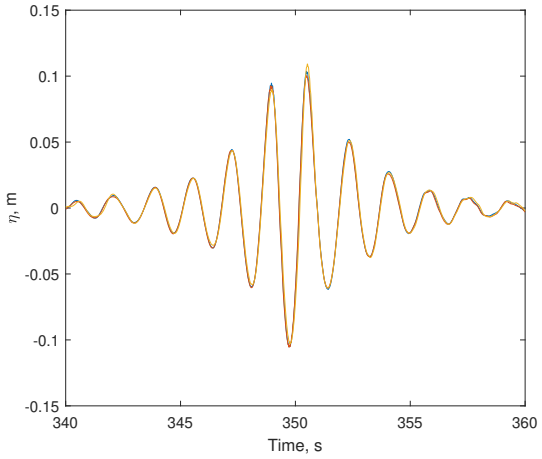

(a) Recordings of MLRW.

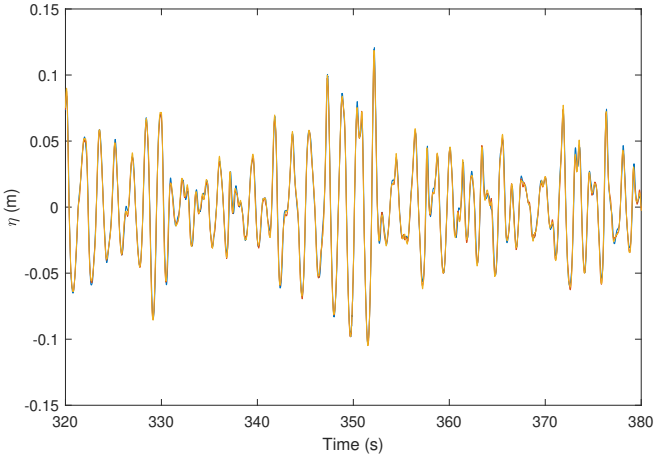

(b) Recordings of CRRW.

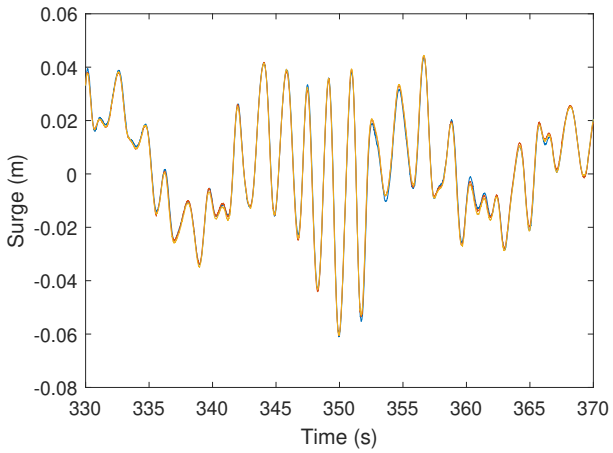

(c) Recorded motions in surge in CRRW.

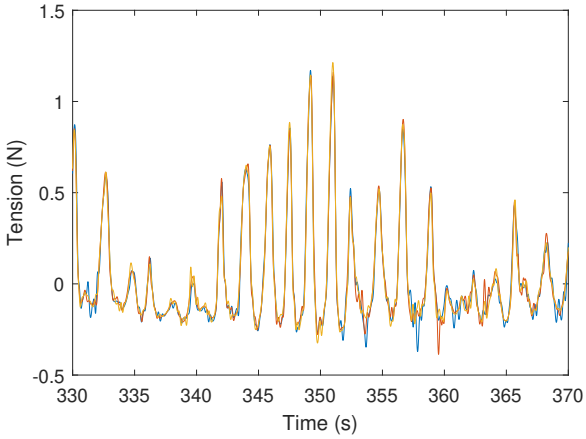

(d) Recorded tensions in mooring line 1 in CRRW.

Figure 6.8: Figures (a) and (b) demonstrate the repeatability of the recorded wave elevations of MLRW and CRRW, respectively, around the focal time set to 350 s where (—) is the first run, (—) second, and (—) third run.

Table 6.3: RMSE-values for measured wave elevations of MLW, MLRW, and CRRW compared to the first run of the individual waves generated.

		MLRW			CRRW		
Run #	η, m	η, m	Surge, m	Tension, N	η, m	Surge, m	Tension, N
Run 2	0.0067	0.0034	0.0006	0.0634	0.0058	0.0017	0.046
Run 3	0.0108	0.0032	0.0014	0.1394	0.0066	0.0021	0.051

6.5 Most Likely Wave Analysis

The results from the conditional wave analysis are presented over this and the next section in full-scale values for both FOWTs. Both sections are divided into subsections presenting results for the two floaters separately. The MLW series presented in this section is designed with an extreme wave height that takes form at a focal time set for 3500 s in the 4000 s long time series in full scale, as previously explained. This wave series is not related to the characteristics of the floater, and an identical wave series is therefore used for both models. The focused wave has a recorded wave height of 24.7 m and steepness of 0.103.

6.5.1 Spar Buoy

The top three recorded responses in surge and pitch, in addition to mooring tension in line 1, are included in Table 6.4. Heave is not included as this DOF demonstrated an insignificant correlation to the recorded mooring tensions in Chapter 5. The most extreme event with the highest load and response in surge and pitch is not recorded at the focal time but at an earlier event in the time series. At this time stamp, the highest wave is recorded with a wave height of 28 m and steepness of 0.186. Observable from the time series of when this event occurs in Figure 6.9 in line with the definition of snap loads from Section 2.9, this mooring tension follows a slack event and is, per the definition given in this section, a snap load. This peak is higher than the top ten recorded mooring loads for the spar buoy from the 3-hour sea states in Chapter 5. This is further discussed in Chapter 7.

Table 6.4: This table includes the top three mooring loads with the local wave height, wave steepness and responses in surge and pitch, and time of occurrence in MLW recorded for the spar buoy.

Time [s]	Tension [kN]	H [m]	ka [∼]	Surge [m]	Pitch [deg]
1859.2	2421.2	28.0	0.186	11.2	10.5
3202.6	2007.0	18.0	0.102	9.8	9.7
3487.1	1663.2	15.1	0.158	7.4	6.8

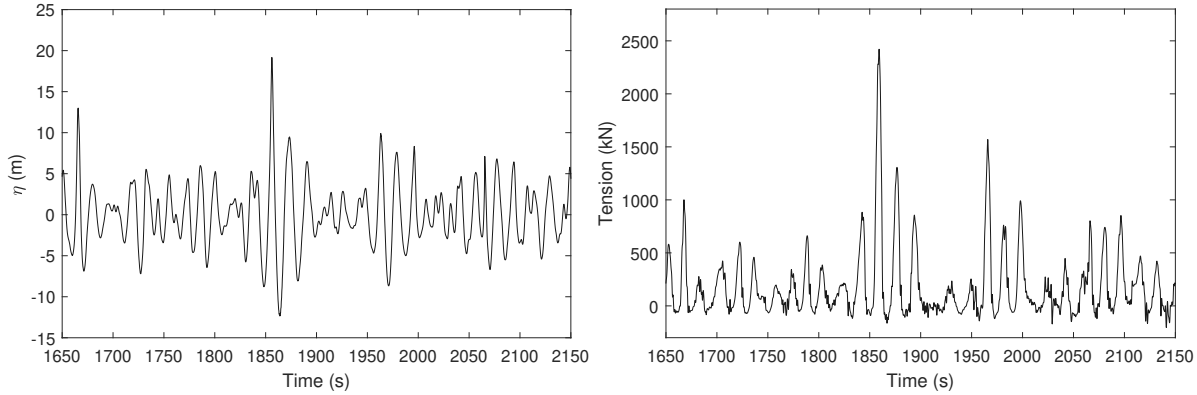

(a) Extreme event at 1860 s in the MLW series. (b) Tensions in mooring line 1 at time of extreme event.

Figure 6.9: Recorded surface elevations in (a) and corresponding tensions in mooring line 1 in (b) during an extreme event occurring in 1860 s in the MLW series.

Cropped time series of the recorded surge and pitch motions are depicted in Figure 6.10. This figure shows a significant response in surge and pitch occurring at 3487 s immediately before the focal time, more extensive than the same parameters recorded in the time of the focused wave. The recorded mooring tension and responses at the time of the focused wave are included in Table 6.6, along with recordings for the semisubmersible exposed to the same wave series. Here, the responses are significantly lower than the top three recorded tensions.

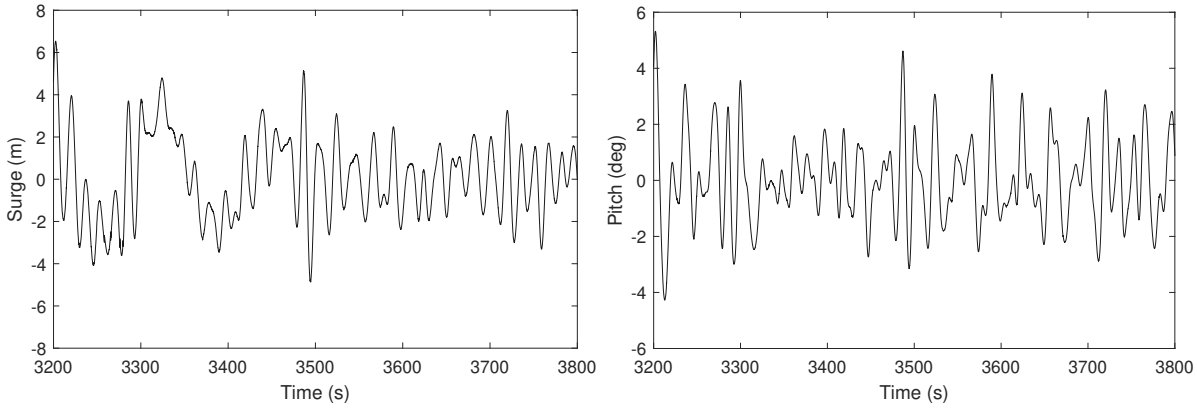

(a) Recorded response in surge around the focal time. (b) Recorded response in pitch around the focal time.

Figure 6.10: Surge and pitch motions in MLW designed to excite extreme response in surge based on the spar buoy's transfer function and related phase-angles.

6.5.2 Semisubmersible

The top three mooring tensions recorded from tests with the semisubmersible in the MLW series are presented in Table 6.6 with the corresponding local wave height, wave steepness, and responses in surge and pitch. The highest mooring load occur again at approximately 1860 s. At this time, the surge response yields a value of 24.1 m which is 21.7% larger than the theoretical maximum response computed from the response spectrum in Chapter 5. The recorded mooring load and responses in surge and pitch at the focal time are significantly lower compared to the values in Table 6.5. These are therefore included in a separate table with the recorded values with the spar buoy floater in Table 6.6 and will be further discussed in Chapter 7.

Table 6.5: This table includes the top three mooring loads with the local wave height, wave steepness and responses in surge and pitch, and time of occurrence in MLW recorded for the semisubmersible.

Time [s]	Tension [kN]	H [m]	ka [∼]	Surge [m]	Pitch [deg]
1860.5	2401.9	28.2	0.2554	24.1	8.8
1877.6	2701.1	21.3	0.1072	18.6	2.6
3202.6	2096.3	16.8	0.1008	16.3	7.8

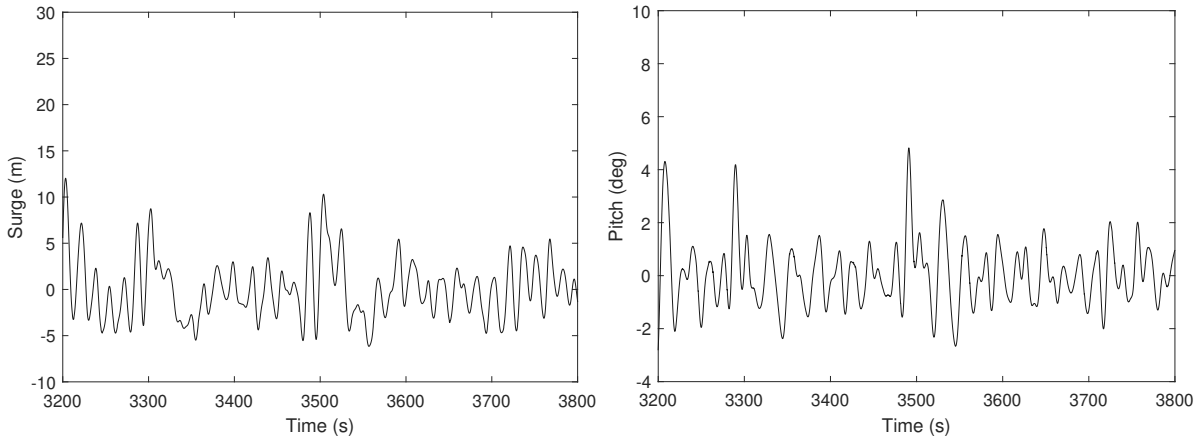

(a) Recorded response in surge around the focal time. (b) Recorded response in pitch around the focal time.

Figure 6.11: Surge and pitch motions in MLRW designed to excite extreme response in surge based on the semisubmersible transfer function and related phase-angles.

Table 6.6: Recorded values at the focal time for both floaters in tests with the MLW series.

FOWT	Tension [kN]	Surge [m]	Pitch [deg]
Spar buoy	487.8	6.6	5.1
Semisubmersible	1855.3	10.3	1.6

6.6 Conditional Random Response Wave Analysis

This section concentrates on the recorded responses in surge and pitch in the CRRW series for both floaters around the focal time. The CRRW definition is conditioned on the transfer function in surge for the spar buoy and both surge and pitch individually for the semisubmersible. The results presented in the tables are given as motion amplitudes as the extreme input response in the computation of MLRW and CRRW is given as amplitude for comparison.

6.6.1 Spar Buoy

The CRRW is designed to induce a response amplitude of 7.42 m in full scale in surge for the spar buoy, as explained in Section 6.2. The recorded response amplitude at the focal point is approx. 5.0 m, 32.6% lower than the input value. This response amplitude yields a total motion of 10 m, 48.5% larger than the surge motion recorded at the focal time in MLW. However, the recorded response motions are lower than the theoretical maximum value in Table 5.1 computed from the response spectrum. The response amplitude excited by the focused wave group in the MLRW definition is 5.0 m. The measured response values in surge, pitch, and mooring tensions in line 1 are included in Table 6.7 for both MLRW and CRRW for comparison, where the recorded mooring tensions are lower in CRRW than in MLRW in line with the motion amplitude in pitch, and tensions in mooring line 1.

Table 6.7: Motion amplitudes and mooring tensions in line 1 measured at the focal time in MLRW and CRRW series designed using the spar buoy's transfer function in surge.

	Surge [m]	Pitch [deg]	Tension [kN]
MLRW	5.0	4.1	1344
CRRW	5.0	3.7	1311

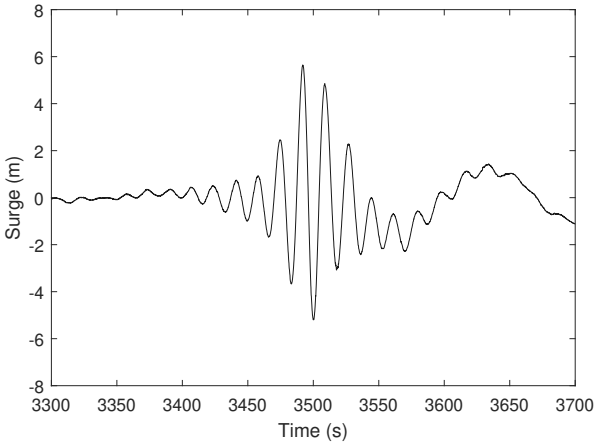

(a) Response in surge recorded in MLRW.

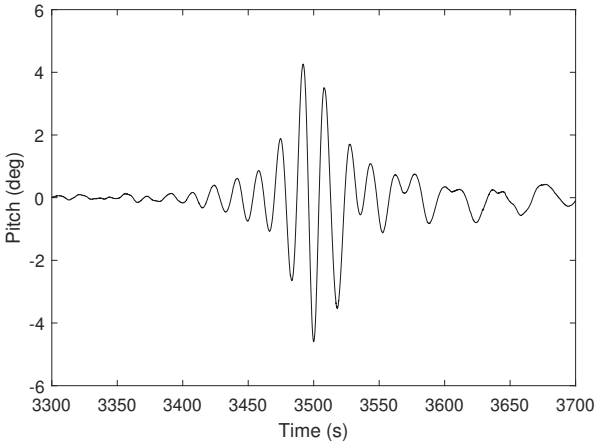

(b) Response in pitch recorded in MLRW.

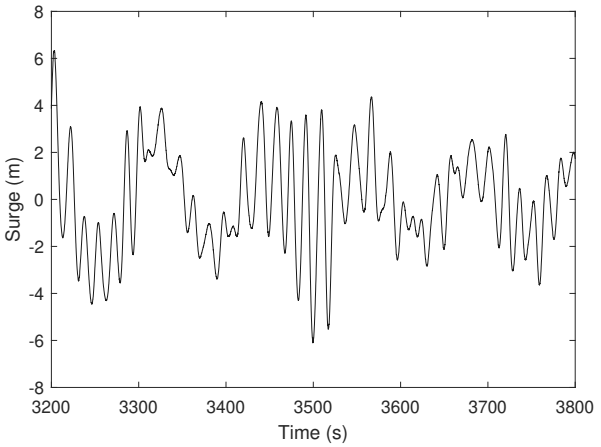

(c) Response in surge recorded in CRRW.

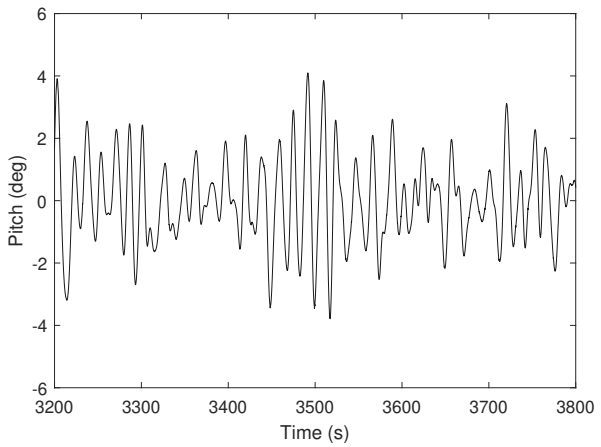

(d) Response in pitch recorded in CRRW.

Figure 6.12: Surge and pitch motions in MLRW in (a) and (b) and in CRRW in (c) and (d), both designed to excite extreme response in surge based on the spar buoy's transfer function and related phase angles recorded in white noise series.

6.6.2 Semisubmersible

Figure 6.13 depicts surge and pitch motions in MLRW compared to CRRW, both conditioned on surge, and Figure 6.14 depicts the same degrees of freedom recorded in CRRW conditioned on pitch. Time series in both figures are cropped to demonstrate responses and loads recorded at the focal time.

From Figure 6.13, it is observed a drifting of the floater where it has drifted approximately 27 m in surge in full scale. The response amplitude is approximately 10.3 m compared to the input amplitude of 9.35 m, approximately approx. 10.2% larger. The recorded response

amplitude in surge in MLRW and CRRW is relatively close. However, the response amplitude in pitch decrease when the MLRW is embedded in Sea 3, creating the CRRW series. Motion in pitch is approx. 9.8 degrees compared to 7.9 degrees in CRRW. The recorded response amplitude in pitch in MLRW presented in Figure 6.13 is more significant than in the CRRW designed to induce an extreme response in pitch where the model rotates at 9.8 degrees compared to approx. 8 degrees in Figure 6.14. The surge motions in MLRW and CRRW are conditioned on transfer function, and phase angles in surge yield a translation of 24 m in MLRW and 27.5 m in CRRW in Figure 6.13 from its initial position, compared to 18 m in Figure 6.14. The mooring tensions in MLRW were recorded but, due to an unidentified error, are not readable and, therefore, not included in Table 6.8. The recorded motion amplitude in pitch at the focal time deviates by 29.9% from the input value.

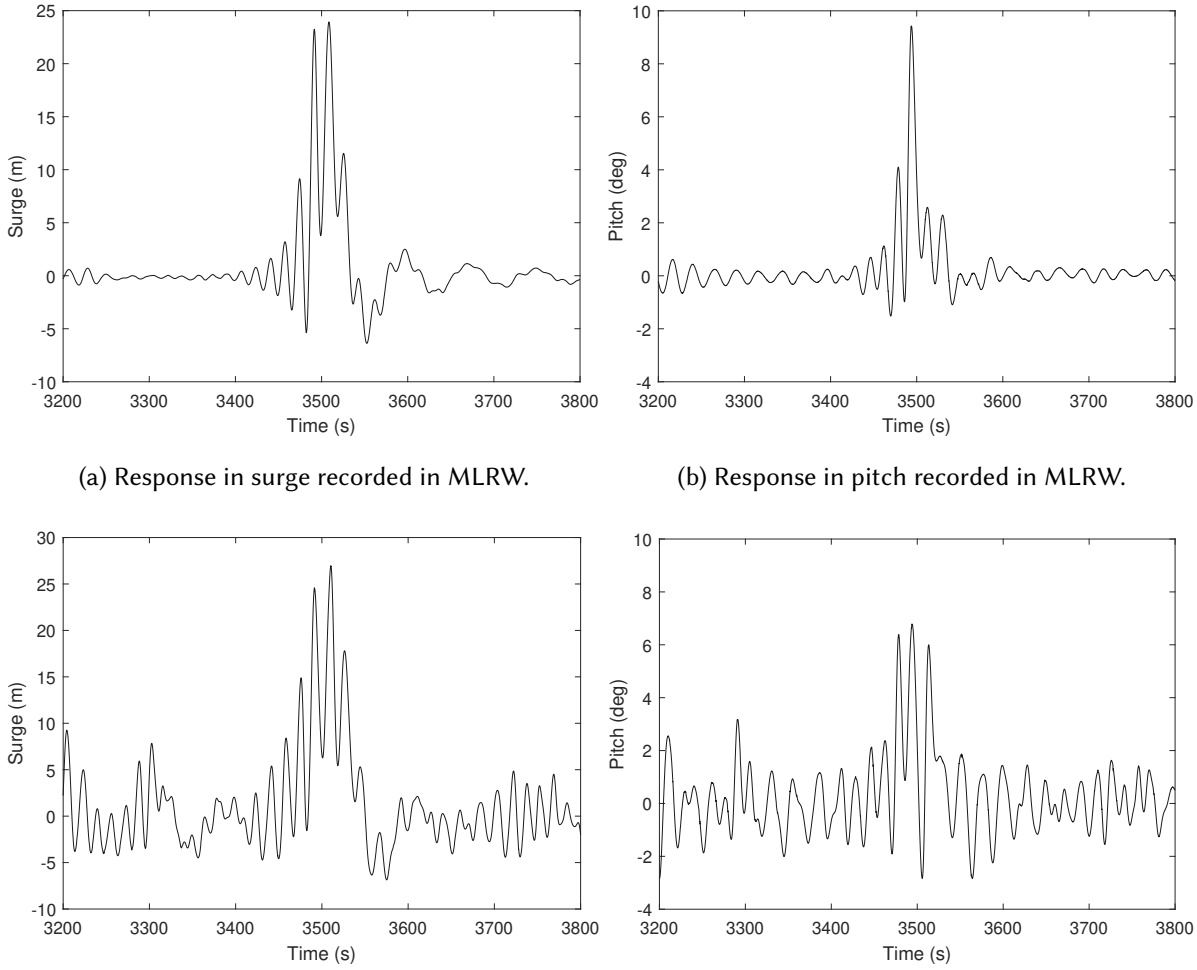

(a) Response in surge recorded in MLRW.

(b) Response in pitch recorded in MLRW.

(c) Response in surge recorded in CRRW.

(d) Response in pitch recorded in CRRW.

Figure 6.13: Surge and pitch motions recorded in MLRW series in (a) and (b) and in CRRW in (c) and (d). Both wave definitions are designed to excite extreme response in surge based on the semisubmersible's transfer function and related phase angles.

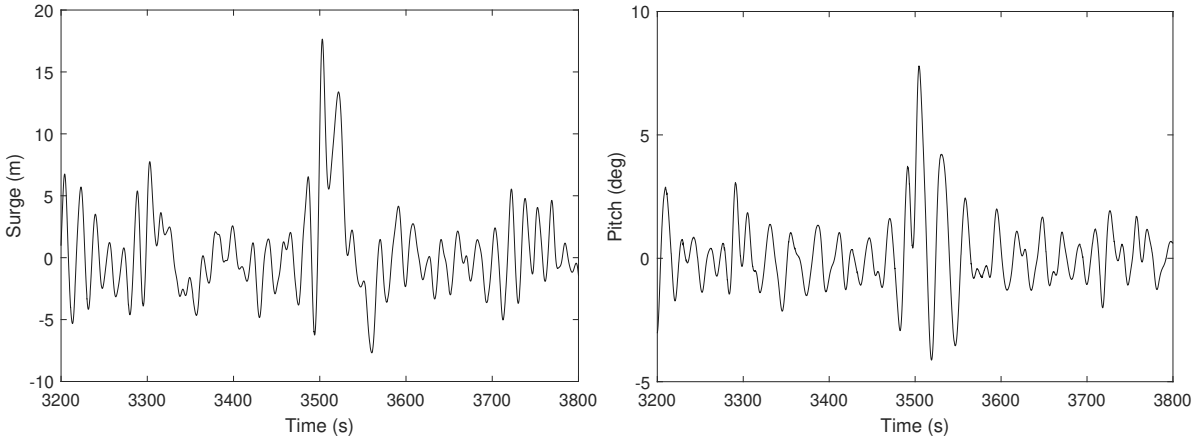

(a) Response in surge recorded in CRRW.

(b) Response in pitch recorded in CRRW.

Figure 6.14: Surge and pitch motions recorded in CRRW series in (a) and (b) designed to excite extreme response in pitch based on the semisubmersible's transfer function and related phase angles.

Table 6.8: Motion amplitudes and tensions in line 1 related to semisubmersible recorded at the focal time in MLRW and CRRW designed for surge and pitch.

	Designed for surge		Designed for pitch
	MLRW	CRRW	CRRW
Surge [m]	10.1	10.3	11.9
Pitch [deg]	4.9	7.9	3.9
Tension [kN]	$\sim$	3164.6	2361.4

7. Discussion

This chapter summarize and discuss the methodologies and theory inline with the results presented in Chapter 5 and 6.

In experimental tests, uncertainties are always present. Efforts throughout this thesis have been made to minimize the uncertainties in the experimental setup and testing. Inevitable are tank effects such as reflections from the tank walls and beach, uncertainties in the measurement apparatus, and human errors, also discussed in previous chapters. It is difficult, however, to determine the combined effect of the individual uncertainties; thus, their impact on the results is difficult to detect but important to be aware of when analyzing experimental results.

The most significant uncertainty in the calibration of the wave series lies in the calibration of the conditional waves as these are manually calibrated, building on methods used in a Master's project in [48]. However, literature supporting this method for waves conditioned on a floater's response is limited. In this thesis, the waves are calibrated by comparing the energy content in the measured wave spectra to the theoretical spectrum. The theoretical spectrum is the background sea in which the frequencies around the focal time are not considered and may be altered during calibration. The conditional waves embedded in a random background sea may be most affected by this, as seen in the calibration of MLW and CRRW, where the recorded wave series varies significantly more than MLRW, which is quite similar to the theoretical wave series. Additionally, a shift of the focal point is observed for the MLW series and is most likely present in the CRRW but more challenging to evaluate as the generated and recorded CRRW series differ greatly from the theoretical series.

Despite running a white noise test experimentally, the RAO curves for the spar buoy and

semisubmersible in each relevant degree of freedom in beam seas in Chapter 5 are computed in sea 1. Using the transfer functions from the white noise test, such as for computing the conditional waves, would give a more accurate result. White noise spectra contain equal energy over a broader range of frequencies than irregular seas, which contain waves with different wave-frequency amplitudes. Additionally, the irregular seas studied in this thesis are well above the eigenfrequencies in surge and pitch but close to heave for both floaters, especially the semisubmersible. This may cause a large amplitude in the transfer function in heave (above 30 m for the spar buoy), as this frequency is excited by energy from the first-order wave frequencies.

The mooring line characteristics are chosen for the individual floater to achieve different characteristics, but both setups are configurated to achieve a system with eigenfrequencies below the peak frequency in the first order wave frequencies. The mooring line stiffnesses and length used for the spar buoy are configurated to represent slack mooring lines to induce snap loads. However, as the experimental tests with the semisubmersible were conducted in cooperation with a company developing this model for commercial use, the mooring line characteristics are chosen to represent a realistic mooring system. Because this information is not yet publicly available, the specifics of this setup are not included in this publication. The different mooring line characteristics may be the cause for no snap loads being defined in the recordings for the semisubmersible using the criteria from Section 2.9. In real mooring systems, avoiding these particular loads due to fatigue is beneficial, which is successfully achieved in the sea-states studied in this thesis for this model.

In comparison, in the recordings of the mooring tensions from the setup with the spar buoy, snap loads frequently occur in all three sea states. In the most extreme sea-states (seas 2 and 3), it is observed from Figure 5.10 that the static tension in mooring line 1 is expected to increase its static tension by 2.5 times to reduce the size and number of snap loads, assuming the mooring lines behave as a linear system. However, the mooring systems are probably nonlinear in the events of snap loads and because the mooring lines used in the setup are quite slack, inducing nonlinear behavior.

Results from Chapter 5 also demonstrate that the maximum mooring tensions appeared to

correlate with the maximum responses in pitch for the spar buoy, and there was no apparent correlation to the local wave height and local wave steepness for this model in Figure 5.8. The spar buoy design is characterized by a significant response in pitch and strong coupling between surge and pitch as this foundation achieves stability through a moment balance between the low center of gravity and the center of buoyancy. The semisubmersible's design induces a coupling in surge and pitch as well. However, its response in surge is more significant than in pitch due to its three-column design, which increases the hydrostatic stiffness in heave, roll, and pitch due to its larger water plane area. This is also reflected in the extreme tensions compared to extreme responses, where the semisubmersible in Figure 5.13 shows a more significant correlation between the motion in surge and tensions. It may be argued that multiple columns in the design of the semisubmersible is also the reason for this model showing a stronger correlation between the local wave height and recorded response in surge, and as the mooring tensions follow the surge motions, is causing the strong linear relationship between the response in surge and mooring tensions. It can also be argued that the lack of correlation between the mooring load, wave height, and steepness might suggest that these parameters alone are not the cause for extreme responses and mooring loads. This could indicate that the wave history's contribution is significant and necessary to study in wave-body interactions of a moored floating body.

In addition to the experimental tests, the spar buoy is modeled as a 3D model in full-scale and used in the time-series analysis in OrcaFlex. Here, estimated values from the experimental setup are used to build a 3D model in GeniE, diffraction analysis in OrcaWave, and mooring line configuration in OrcaFlex. The eigenfrequencies from numerical decay tests and RAO curves compare well to the experimental results. However, the extreme statistical values of the responses in surge, heave, and pitch, in addition to the mooring tensions, are significantly lower in OrcaFlex compared to the experimental results, similar to results achieved in [19–21]. The diffraction analysis and effects included in OrcaFlex to compute responses and hydrodynamic loads are based on linear theory. No higher effects are included in this project as this significantly increases the computational time. Therefore, the response and loads will be underpredicted despite the most significant contribution being from linear excitation forces. Higher-order effects, especially difference-frequency loads, are significant for slack-moored structures as their eigenfrequencies are in the same range. Higher-order

effects contribute to a smaller extent than linear forces but may contribute to the response and loads being underpredicted.

The damping in the system in numerical codes can be included in forms of damping matrices in the diffraction analysis or by incorporating a linear or quadratic damping coefficient in OrcaFlex in each DOF. It may therefore be a sensitive parameter affecting the response and mooring loads. The damping in the system is tuned after experimental decay curves in this project, where the method resulting in most similar results to the experiment was to tune the drag coefficient until similar damping was achieved. As the drag force is dependent on the Reynolds number, this coefficient can have an exponential effect with the increased severity in the environment, causing a too large damping effect in extreme environments, such as the sea-states studied in this thesis represents. Additionally, as the Reynolds number of the model might be so low compared to the full-scale model, the drag coefficient cannot be assumed to be Reynolds number independent. Thus the experimentally obtained drag coefficients would not be representative.

The numerical response and mooring loads are not compared to experimental time series in this thesis despite the same sea-states being used. This is because the seed number used to compute phases in the irregular seas are different such that the wave groups and wave steepness, among other effects, are coherently different; thus, time series are dissimilar. The statistical values should be similar regardless of the seed number and are therefore compared. The RAO curves, both numerically and experimentally, are computed using sea 1 for comparison as this sea-state is studied both experimentally and numerically and contains frequencies furthest from the spar buoys eigenfrequencies among the other irregular test cases studied in this project. Additionally, the same sea-states include the same frequency range and, ideally, the same energy amplitude per frequency component neglecting minor differences, such as wave tank reflections.

The effect of using a different seed number is observed in the Most Likely Wave analysis in Section 6.5 where the same wave parameters used to define the background sea are the same used in Sea 3 in the experimental tests. Despite this, the recorded responses and mooring tensions recorded in MLW at an extreme event transpiring approximately at 1859 s in

the series is not recorded in Sea 3 and is also more extreme than any of the waves and tensions among responses recorded in this sea in Chapter 5. The focused wave amplitude in the MLW series is defined by a theoretical extreme wave height calculated from the wave spectra of Sea 3, where the response and mooring tensions recorded at the focal time are lower than those recorded at 1859 s and in Chapter 5. However, the MLRW and CRRW conditioned on the spar buoys transfer function in surge yields a motion amplitude in surge equal to 10 meters, larger than the motions recorded at the focal time in MLW, as can be observed in Table 7.1. In this table, the results from both Chapter 5 and 6 are summarized. As the extreme input response in the computation of this wave definition is 14.84 m, the recorded response is lower than the input and, therefore, lower than the expected value. The same trend is observed for the semisubmersible. For this floater, the recorded motions at the focal time are closer to the input used in this wave definition, maybe due to tauter lines being used.

Table 7.1: Summarized values of the theoretical maximum motions in surge, pitch, and mooring tensions computed in Sea 3 compared to the same parameters recorded at the focal time in MLW, MLRW, and CRRW.

	Sea 3	MLW	MLRW	CRRW
Surge, m	12.6	6.6	10.0	10.0
Pitch, deg	10.1	5.1	8.2	7.4
Tension, kN	1392	488	1344	1311

A reason for the underprediction of the extreme response in surge at the focal time can be related to the decision of the focal point. The floaters' instant position is challenging to match experimentally as the model drifts when exposed to incident waves. Therefore, using the model's resting position as the focal point is less accurate than the instant position of the model's COG. The author of [48] also found that due to nonlinear interactions, the focal point shifts from the input position in the Njord Wave synthesis program. This may also be observed in the MLW time series, where the maximum surface elevation occurs at WG6 and could be more significant further downstream, which cannot be evaluated as WG6 is the wave gauge located the furthest from the wavemaker. The maximum amplitude occurs at the focal point but is only 0.001 m higher than the wave amplitude at WG6. Additionally, the wave is not symmetric at this point, indicating that the wave is not entirely in focus.

The transfer functions are used in the computation of the MLRW series. These are computed using recordings from the white noise test where the models were taken out of the wave tank while the design waves were computed and calibrated. Therefore, the system characteristics in the irregular seas may diverge from MLRW and CRRW due to minor changes in the length of the mooring lines and spring stiffness caused by the disassemblement. Alternatively, if the connection point on the floater has shifted, all factors could cause the system's eigenfrequencies to change. Measures were made to reduce these uncertainties, such as markings on the mooring lines to ensure the same lengths are maintained throughout. Decay tests before and after the calibration of design waves should have been conducted to check if the same characteristics are kept.

However, using experimental recordings to compute the transfer function and phase angles, these are therefore sensitive to filtering methods and signal processing where noise, for instance, can result in detrimental effects. Ideally, the transfer function and phase-angles used in the computation should be generated numerically to remove these uncertainties, but it was not conducted as the numerical model was not finished at the time of the experimental tests in MarinLab. Some parameters from the experimental setup were needed in the numerical model, such as mooring stiffness and experimental decay tests to tune the damping in the numerical model.

8. Conclusion

The extreme responses and mooring loads for a spar buoy and semisubmersible floater are studied in irregular sea-states and conditional waves representing extreme wave conditions. In addition to experimental tests, a numerical analysis was performed with a 3D model of the spar buoy in OrcaFlex to validate the hydrodynamic modeling against experimental results.

The numerical decay tests and RAO curves have demonstrated that the link element in OrcaFlex can be used to model a light mooring system for a floating spar. However, the short-term statistics of the numerical responses and mooring loads in all three sea-states are severely underpredicted despite decay tests being quite similar in damping and eigenfrequencies. This supports the results in [20] which stated that numerical decay tests might not be sufficient to estimate the real damping of the floater and its positioning system in all environments.

A direct correlation between extreme mooring tensions, wave height, and wave steepness has not been found in this project. The results in Chapter 5 indicate a correlation between the design characteristics of the floater where the tensions in moorings for the spar buoy have the highest correlation determination coefficient of 81.6% with pitch, and 71.8% for the semisubmersible with surge. Results confirm that the slack mooring lines used to position the spar buoy do induce snap loads. By assuming a linear behavior in the mooring lines, an increase of the static tension by a factor of 2.5 appears to reduce the size and number of snap loads occurring in all three sea-states.

The experimental MLW and CRRW series diverge around focal time to the theoretical wave series. The focal point is challenging to match the floater's instant center position in waves as the slack lines allow the models to drift. For both models, the more extreme responses and

loads recorded at the focal time in CRRW and MLRW are higher than in the MLW series, indicating that most extreme events do not necessarily arise from extreme wave heights as stated by [33] and [57]. Compared to the irregular sea-states, the extreme responses and tensions are more significant in the irregular waves compared to the conditioned ones. Therefore, the results indicate that irregular sea-states may be a better method for studying extreme responses and mooring tensions. However, the randomness in these seas requires multiple test cases in the form of different seed numbers to gain better certainties that the most extreme events are captured. As this is a costly method, a numerical approach, validated by experimentation, maybe an overall better method if a solution to the underprediction in numerical codes, as documented in this project among the work presented in [19; 21], is found.

As a final concluding remark, due to the uncertainties associated with experimental results using conditional waves, the work presented can therefore not conclude if the conditional waves can be used to generate extreme responses and tensions more effectively than 3-hour sea-states. Instead, the work presented can contribute as a comparative database for students, researchers, and industries wishing to continue researching critical wave episodes for FOWTs, building on the methods and theory presented.

9. Suggestions for Further Work

The work presented in this thesis has demonstrated further research needs in multiple areas to be studied in later projects.

The methodology used to calibrate the conditional waves presents significant uncertainties in the results; hence developing new methods that preserve their properties is therefore highly recommended. Also, using experimental results to compute the transfer function needed in the definition of the MLRW and CRRW introduces uncertainties excluded if computed in numerical codes. Therefore, a further study on MLRW and CRRW in industrial codes using the numerical transfer functions and phase angles is recommended. In addition, using a numerical second-order time series to predict the floater's drift position and use this information to determine a focal point would ensure greater accuracy in the results.

Moreover, it is recommended to compute the quadratic transfer functions in the diffraction analyses, so higher-order effects can be included in OrcaFlex to evaluate if the responses and mooring loads remain underestimated. Further studies on modeling mooring line dynamics are also recommended, and if the link element can be used to model a light mooring system compared to the line element typically used in OrcaFlex. It is advised to conduct further research on tuning the damping in irregular sea-states than the traditional method using experimental decay tests to evaluate if this is a better strategy. A final suggestion is to use other sources of damping, such as linear or quadratic damping coefficients, rather than tuning the drag coefficients.

References

[1] International Energy Agency (IEA), "Offshore Wind Outlook 2019," November, 2019.

[2] UNFCCC, "The Paris Agreement." [Online]. Available: https://unfccc.int/process-and-meetings/the-paris-agreement/the-paris-agreement

[3] European Commission, "The european green deal," *Eur. Comm*, vol. 53, no. 9, p24, 2019.

[4] K. Freeman, C. Frost, G. Hundleby, A. Roberts, B. Valpy, H. Holttinen, L. Ramírez, and I. Pineda, "Our Energy Our Future," p. 78, 2019. [Online]. Available: https://windeurope.org/about-wind/reports/our-energy-our-future/

[5] A. N. Robertson, S. Gueydon, E. Bachynski, L. Wang, J. Jonkman, and D. Alarcón, "OC6 Phase I : Investigating the Underprediction of Low-frequency Hydrodynamic Loads and Responses of a Floating Wind Turbine." 2020.

[6] ETIPWIND, "Set-plan offshore wind implementation plan," Brussels, 2018.

[7] J. Davidson and J. Ringwood, "Mathematical Modelling of Mooring Systems for Wave Energy Converters - A Review," *Ener*, vol. 10, no. 5, p.666, 2017.

[8] R. E. Harrison, L. Johanning, and J. Wolfram, "Mooring Systems for Wave Energy Converters: A Review of Design Issues and Choices," *Marec*, 2004.

[9] Equinor, "Flytende havvind i Equinor - equinor.com." [Online]. Available: https://www.equinor.com/no/what-we-do/floating-wind.html

[10] Orcina, "OrcaFlex - Documentation," 12.1b Edition. 2022,. [Online]. Available: https://www.orcina.com/webhelp/OrcaFlex/Default.htm

[11] J. Jonkman, K. Shaler, J. Jonkman, and K. Shaler, "FAST . Farm User ' s Guide and Theory Manual FAST . Farm User ' s Guide and Theory Manual," no. April, 2021.

[12] M. Leimeister, A. Kolios, and M. Collu, "Critical Review of Floating Support Structures for Offshore Wind Farm Deployment," *Journal of Physics: Conference Series*, vol. 1104, p. 012007, 10 2018.

[13] P. K. Stansby and E. C. Moreno, "Hydrodynamics of the multi-float wave energy converter M4 with slack moorings: Time domain linear diffraction-radiation modelling with mean force and experimental comparison," *Applied Ocean Research*, vol. 97, p. 102070, apr 2020.

[14] J. Jonkman and W. Musial, "Offshore Code Comparison Collaboration (OC3) for IEA Task 23 Offshore Wind Technology and Deployment." no. December, 2010.

[15] J. Jonkman, S. Butterfield, W. Musial, and G. Scott, "Definition of a 5-MW Reference Wind Turbine for offshore System Development." NREL/TP-500-38060. NREL: Golden, CO, 2009.

[16] A. Robertson, J. Jonkman, M. Masciola, H. Song, A. Goupee, A. Coulling, and C. Luan, "Definition of the Semisubmersible Floating System for Phase II of OC4," *NREL Technical Report*, 2014.

[17] A. Ross and G. Mckinnon, "Orcina Project 1405 Wind Turbine Validation Report," 2018.

[18] A. Robertson, J. Jonkman, F. Vorpahl, J. Qvist, L. Frøyd, X. Chen, J. Azcona, E. Uzunoglu, C. G. Soares, C. Luan, F. Pengcheng, A. Yde, T. Larsen, R. Buils, L. Lei, T. A. Nygard, A. Heege, S. R. Vatne, T. Duarte, C. Godreau, H. Fabricius, A. W. Nielsen, H. Riber, C. Le, R. Abele, F. Beyer, A. Yamaguchi, K. Jin, H. Shin, W. Shi, H. Park, M. Alves, and M. Guérinel, "Offshore Code Comparison Collaboration Continuation Within IEA Wind Task 30 : Phase II Results Regarding a Floating Semisubmersible Wind System Preprint," no. March 2014.

[19] N. Robertson, C. Guedes, R. Harries, A. Yde, C. Galinos, P. Bozonnet, R. Bergua, J. Galvan, I. Mendikoa, C. Barrera, and A. N. Robertson, "C5 Project Phase II: Validation of Global Loads of the DeepCwind Floating Semisubmersible Wind Turbine," *Energy Procedia*, vol. 137, pp. 38–57, 2017.

[20] A. Pegalajar-Jurado and H. Bredmose, "Reproduction of Slow-Drift Motions of a Floating

Wind Turbine Using Second-Order Hydrodynamics and Operational Modal Analysis," *Marine Structures*, 66, pp. 178-196, 2019.

[21] J. Azcona, F. Bouchotrouch, and F. Vittori, "Low-frequency dynamics of a floating wind turbine in wave tank–scaled experiments with SiL hybrid method," *Wind Energy*, 22, pp. 1402-1413, 2019.

[22] S. Chakrabarti, *Hydrodynamics of Offshore Structures*. WIT press, 1987.

[23] B. Pettersen, "Marin Teknikk 3 - Hydrodynamikk," *Pensumhefte*, Akademika, 2020.

[24] O. M. Faltinsen, *Sea Loads on Ships and Offshore Structures*, ser. Cambridge Ocean Technology Series. Cambridge University Press, 1990.

[25] S. Steen, *Experimental Methods in Marine Hydrodynamics*, Lecture Notes, August 2014.

[26] DNV GL, *Environmental Conditions and Environmental Loads*, Recommended Practice DNV-RP-C205, October 2010.

[27] K. Hasselmann, T. P. Barnett, E. Bouws, and H. Carlson, "Measurements of Wind-Wave Growth and Swell Decay During the Joint North Sea Wave Project (JONSWAP)," January, 1973.

[28] DNV GL, *Wave loads*, Class Guidelines DNVGL-CG-0130, January 2018.

[29] J. P. Bentley, *Principles of Measurement Systems*, 4th ed. Harlow: Pearson Education Limited, 2005.

[30] J. Fredsoe and B. M. Sumer, *Hydrodynamics Around Cylindrical Structures (Revised Edition)*, ser. Advanced Series On Ocean Engineering. London: World Scientific Publishing Company, 2006, vol. 26.

[31] M. Longuet-Higgins, "On the Statistical Distribution of the Heights of Sea Waves," *Journal of Marine Research*, vol. Xl, no. 203, pp. 0–44, 1952.

[32] P. Tromans, A. R. Anaturk, and P. Hagemeijer, "A New Model for the Kinematics of Large Ocean Waves - Application as a Design Wave," *Proc. 1st Offshore and Polar Engineering (ISOPE) Conference, Edinburgh*, vol. 3, 1991.

[33] D. Jesper Skjoldager, "Application of Conditional Waves as Critical Wave Episodes for Extreme Loads on Marine Structures," Ph.D. dissertation, Danmarks Technical University, July 2004.

[34] M. J. Cassidy, R. E. Taylor, and G. T. Houlsby, "Analysis of Jack-up Units Using a Constrained NewWave Methodology," *Applied Ocean Research*, vol. 23, no. 4, pp. 221–234, 2001.

[35] P. H. Taylor, P. Jonathan, and L. A. Harland, "Time Domain Simulation of Jack-up Dynamics With the Extremes of a Gaussian Process," *Proceedings of the 14ht International Conference on Offshore Mechanic and Arctic Engineering (OMAE)*, vol. 1-A, 1995.

[36] M. Lerch, M. De-Prada-Gil, and C. Molins, "The influence of different wind and wave conditions on the energy yield and downtime of a Spar-buoy floating wind turbine," *Renewable Energy*, vol. 136, pp. 1–14, 2019. [Online]. Available: https://doi.org/10.1016/j.renene.2018.12.096

[37] S. K. Chakrabarti, *Handbook of Offshore Engineering (2-Volume Set).* St. Louis: Elsevier Science Technology, 2005.

[38] J. R. Morison, M. P. O'Brien, J. W. Johnson, and S. A. Schaaf, "The Force Exerted by Surface Waves on Piles," *Pet. Trans.*, 189, 149-54, 1950.

[39] Orcina, "Environment theory," 2022. [Online]. Available: https://www.orcina.com/webhelp/OrcaFlex/

[40] A. Campanile, V. Piscopo, and A. Scamardella, "Mooring Design and Selection for Floating Offshore Wind Turbines on Intermediate and Deep Water Depths," *Ocean Engineering*, vol. 148, pp. 349–360, jan 2018.

[41] DNV GL, *Modelling and Analysis of Marine Operations*, Recommended Practice DNV-RP-H103, April 2011.

[42] W. T. Hsu, K. P. Thiagarajan, M. Hall, M. MaCnicoll, and R. Akers, "Snap loads on mooring lines of a floating offshore wind turbine structure," *Proceedings of the International Conference on Offshore Mechanics and Arctic Engineering - OMAE*, vol. 9A, 2014.

[43] Edinburgh Designs, "Absorbing wavemakers," 2022. [Online]. Available: http://www4.edesign.co.uk/waves/absorbing-wavemakers/

[44] J. M. J. Journée and W. W. Massie, "Offshore hydrodynamics," 1. ed. Delft University of Technology, 2001.

[45] P. Hinrichsen, "Bifilar Suspension Measurement of Keelboat Inertia Parameters," *21st Chesapeake Sailing Yacht Symposium, CSYS 2013*, pp. 1–37, 2013.

[46] H. D. Young, R. A. Freedman, and A. L. Ford, *Sears and Zemansky's University Physics: With Modern Physics (Global Edition).* Harlow: Pearson Education, 2016, vol. 14th Edition.

[47] D. Lande-Sudall, T. Høyven, K. Herfjord, and T. Thuestad, "Wave-induced collision loads and moments between a spar-buoy floating wind turbine and an installation vessel," *Journal of Physics: Conference Series*, vol. 1669, p. 012009, 10 2020.

[48] M. G. Øen, "An Open Database of Free-surface Gravity Waves for Validation of Numerical Wave Tanks," Master's thesis, University of Bergen, June 2021.

[49] Statoil, "Barents East blocks Metocean Design Basis," Tech. Rep., 2015.

[50] Edinburgh Designs, "Njord wave synthesis manual - reference manual," [PDF]. 2016.

[51] NREL, "S822 airfoil shape," 2021. [Online]. Available: https://wind.nrel.gov/airfoils/shapes/S822_Shape.html

[52] P. K. Stansby, E. Carpintero Moreno, D. D. Apsley, and T. J. Stallard, "Slack-moored Semi-submersible Wind Floater With Damping Plates in Waves: Linear Diffraction Modelling With Mean Forces and Experiments," *Journal of Fluids and Structures*, vol. 90, pp. 410–431, 2019.

[53] A. Robertson, J. Jonkman, M. Masciola, and H. Song, "Definition of the Semisubmersible Floating System for Phase ll of OC4," NREL, Tech. Rep. September, 2014.

[54] Orcina, "Diffraction: L02 OC4 Semi-sub," 2022. [Online]. Available: www.orcina.com

[55] Orcina, "OrcaWave - Data: Wave spectrum," version 11.1d. 2022,. [Online]. Available: https://www.orcina.com/webhelp/OrcaWave/Default.htm

[56] J. L. Devore, K. N. Berk, and M. A. Carlton, *Modern Mathematical Statistics with Applications*, 3rd ed., ser. Springer Texts in Statistics. Cham: Springer International Publishing AG, 2021.

[57] M. Hann, D. Greaves, A. Raby, and B. Howey, "Use of constrained focused waves to measure extreme loading of a taut moored floating wave energy converter," *Ocean Engineering*, vol. 148, no. October 2017, pp. 33–42, 2018.

A. Appendix A

This appendix is a supplement to the time-domain results presented in Chapter 5.

A.1 Time-Domain Results - Spar Buoy

The top ten tensions recorded in seas 1 and 2 is summarized in Table A.1 and A.2 with the local wave height, wave steepness, motions in surge and pitch for the spar buoy. These values are used in Figure 5.8 and Table 5.4.

Table A.1: Top ten mooring tensions with corresponding time stamp, local wave height,wave steepness, surge and pitch motion amplitudes recorded in sea 1

Peak nr. #	Time [s]	N [kN]	H [m]	ka [∼]	Surge [m]	Pitch [deg]
1	95.1	543.8	4.7	0.100	2.0	2.0
2	152.9	600.8	2.7	0.073	2.8	3.2
3	276.2	586.3	2.4	0.045	2.6	3.1
4	362.5	521.2	1.7	0.042	2.6	1.8
5	395.8	512.0	1.6	0.022	1.2	1.1
6	597.9	664.8	4.4	0.047	3.5	4.2
7	690.8	592.1	3.1	0.066	2.7	3.0
8	983.9	608.4	0.3	0.006	2.7	2.8
9	1116.8	616.3	2.5	0.061	3.4	2.8
10	1119.6	565.8	4.3	0.034	1.6	2.7

Table A.2: Top ten mooring tensions with corresponding time stamp, local wave height,wave steepness, surge and pitch motion amplitudes recorded in sea 2

Peak nr. #	Time [s]	N [kN]	H [m]	ka [∼]	Surge [m]	Pitch [deg]
1	1125.0	1161.3	10.3	0.084	5.4	5.7
2	1155.0	1217.8	1.8	0.026	5.2	7.2
3	1515.0	1354.3	12.3	0.248	5.9	5.5
4	2759.0	1238.2	7.0	0.133	4.9	7.1
5	2787.0	1556.0	4.0	0.054	7.3	9.8
6	5977.0	1552.2	6.9	0.067	8.2	9.5
7	7758.0	1227.6	3.4	0.036	5.5	6.4
8	8178.0	1187.8	4.2	0.051	5.5	6.3
9	10426.0	1135.2	7.5	0.077	5.2	5.3
10	11165.0	1331.6	3.0	0.074	8.1	7.0

A.2 Time-Domain Results - Semisubmersible

The top ten tensions recorded in seas 1 and 2 are summarized in Table A.3 and A.4 with the local wave height, wave steepness, motions in surge, and pitch for the semisubmersible. These values are used in Figure 5.13 and Table 5.6.

Table A.3: Top ten mooring tensions with corresponding time stamp, local wave height,wave steepness, surge and pitch motion amplitudes recorded in sea 1 for the semi

Peak nr. #	Time [s]	N [kN]	H [m]	ka [∼]	Surge [m]	Pitch [deg]
1	668.2	1319.7	11.3	0.29	4.4	1.3
2	1414.2	1333.7	6.7	0.07	2.6	0.9
3	1564.2	1269.6	4.4	0.07	1.4	1.2
4	2775.9	1360.3	12.9	0.14	6.7	2.2
5	3476.1	1299.4	8.4	0.12	3.3	0.1
6	5993.8	1375.9	12.0	0.14	6.9	2.7
7	6643.5	1319.7	9.8	0.12	4.4	1.5
8	10440.7	1299.8	11.0	0.20	5.5	1.4
9	11182.8	1386.3	14.1	0.27	6.9	2.4
10	11355.0	1270.0	10.1	0.14	4.8	1.4

Table A.4: Top ten mooring tensions with corresponding time stamp, local wave height,wave steepness, surge and pitch motion amplitudes recorded in sea 2 for the semi

Peak nr. #	Time [s]	N [kN]	H [m]	ka [∼]	Surge [m]	Pitch [deg]
1	2774.6	2447.5	17.4	0.15	17.2	6.1
2	2789.8	2430.9	23.5	0.20	17.7	3.2
3	5978.5	2328.4	24.7	0.26	15.7	4.2
4	5993.8	2330.9	14.7	0.09	15.1	5.7
5	6922.9	2023.0	13.3	0.14	11.7	5.8
6	7477.4	1994.3	21.3	0.24	12.7	2.6
7	8661.8	2097.0	13.1	0.12	12.8	4.3
8	8677.0	1946.9	19.9	0.12	11.9	6.1
9	10863.0	1840.6	17.8	0.26	10.2	3.3
10	11181.1	2387.3	17.5	0.17	16.4	6.9

B. Appendix B

This appendix supplements the results from the calibration of the conditional waves presented in Chapter 5.

B.1 The Most Likely Response Wave (MLRW)

Spar Buoy

Figure B.1 depicts the measured wave spectra of the MLRW conditioned on the spar buoy's response in surge. The black line represents the target spectrum, and the grey line is the measured spectrum. One gain correction results in the best fit compared to the target spectrum as no gain correction, and two gain corrections result in lower energy content. Figure B.2 illustrates the generated wave series of the MLRW compared to the theoretical series, where the calibrated wave series demonstrate a good fit.

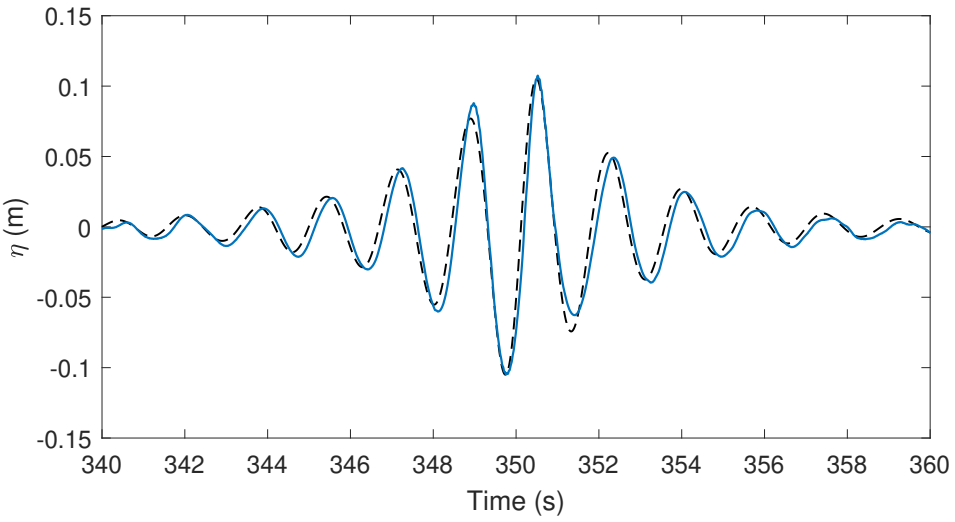

Figure B.1: Results from the calibration of MLW time series where: (—) is target, (—) is without gain correction, (—) is after one gain correction, and (—) after two gain corrections.

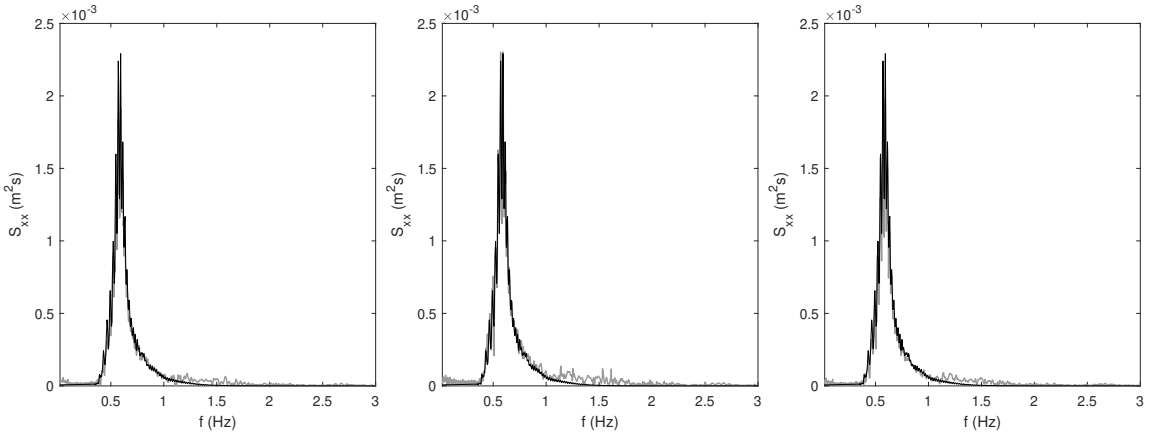

Figure B.2: Recorded wave spectra of MLRW (—) compared to target spectra (—) where (a) is measured wave spectra from uncalibrated wave series, (b) is the measured wave spectra after one gain correction, and (c) is the measured wave spectra after two gain corrections.

Semisubmersible

The MLRW definition designed to induce maximum response for the semisubmersible uses the same gain correction factor series as for spar buoy. This is because the expected differences between the theoretical series as input and the recorded series depend on the wavemaker's transfer function. The measured wave spectrum before and after applying the spar buoy's transfer function is depicted in Figure B.3. The calibrated wave series is depicted in Figure B.4 and differs significantly from the theoretical wave series as the wave amplitude between 348 s and 350 s breaks and dissipates energy.

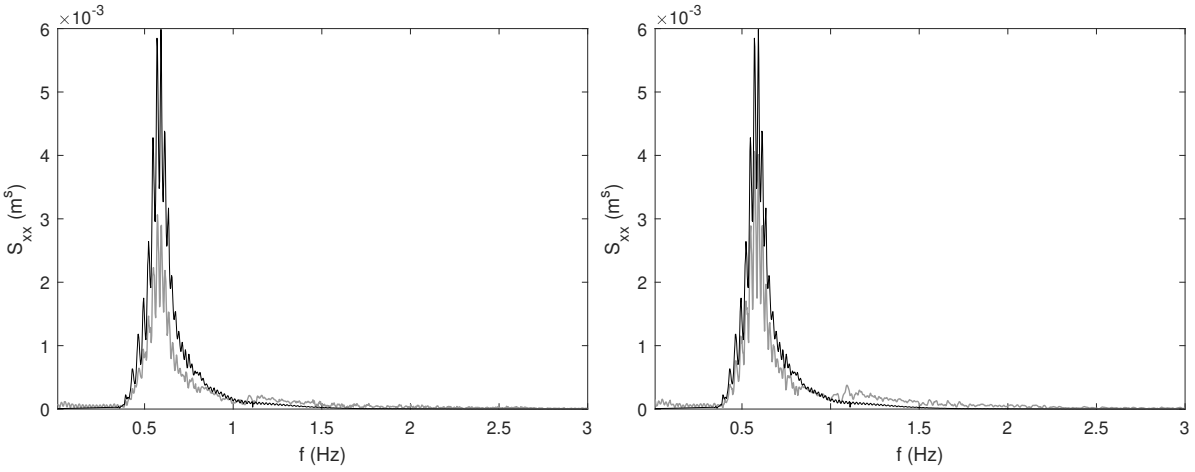

Figure B.3: Recorded wave spectra of MLRW for the semisubmersible's response in surge in (—) compared to target spectra (—) where (a) is measured wave spectra from uncalibrated wave series, (b) is the measured wave spectra after one gain correction.

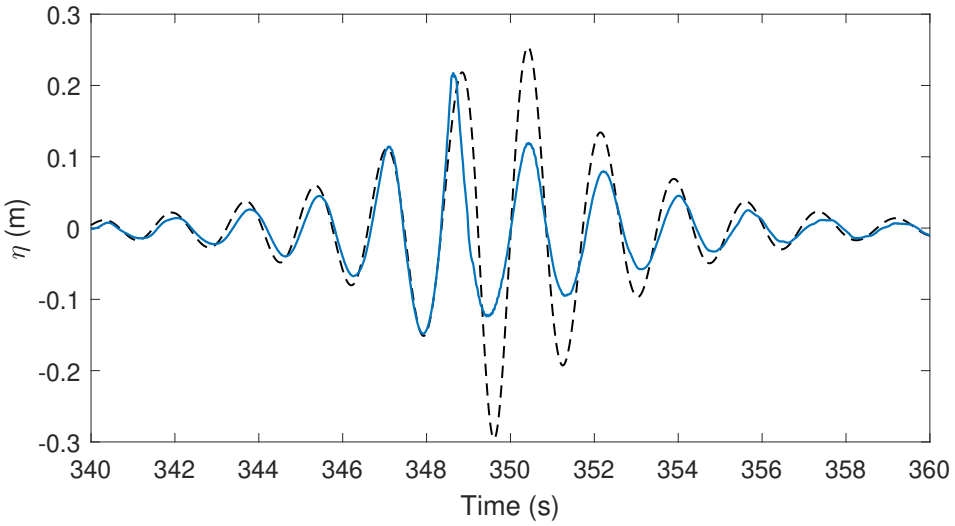

Figure B.4: Measured wave elevations of MLRW (spar buoy) for surge (—) compared to target wave elevations (- - -) during calibration of the conditional wave series.

B.2 Conditional Random Response Wave (CRRW)

Spar Buoy

Figure B.5 shows the resulting wave spectra from the calibration. The recorded surface elevations with no gain correction and one and two gain corrections are compared to the theoretical wave profile. The calibrated wave series is depicted in Figure B.6.

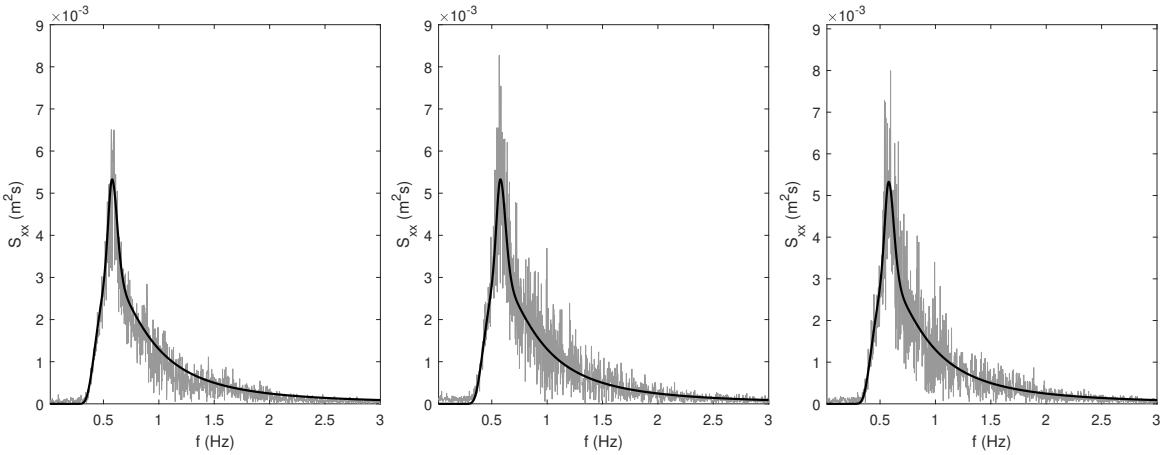

Figure B.5: Recorded wave spectra of CRRW (—) compared to target spectra (—), with a JONSWAP fit with $H_s = 0.13$m, $T_p = 1.73$s, where (a) is measured wave spectra from uncalibrated wave series, (b) is the measured wave spectra after one gain correction, and (c) is the measured wave spectra after two gain corrections.

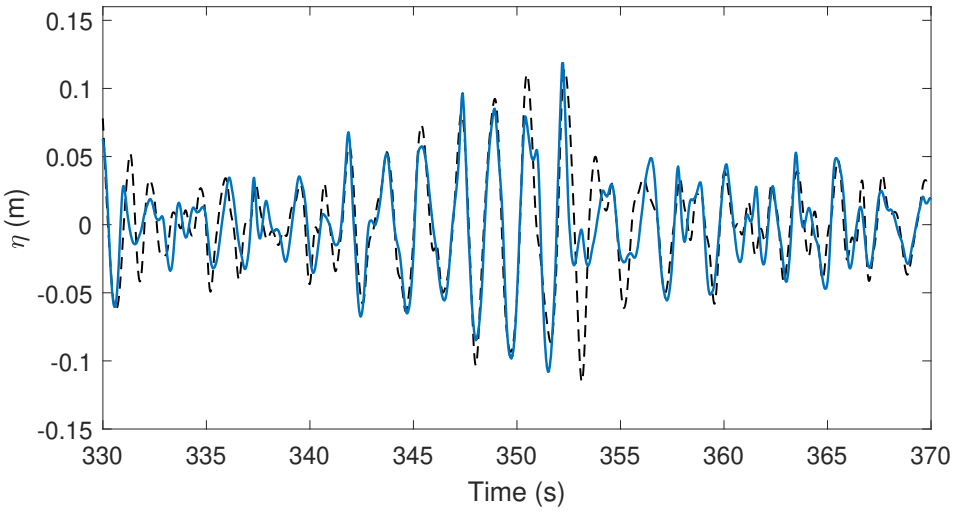

Figure B.6: Measured wave elevations of CRRW (spar buoy) for surge (—) compared to target wave elevations (- - -) during calibration of the conditional wave series.

Semisubmersible

Similar to the calibration of the MLRW conditioned on the semisubmersible's response, the CRRW definitions are for surge calibrated using the same transfer function as for the CRRW conditioned on the spar buoys response in surge. Due to time limitations in the tank, the CRRW in pitch was not calibrated. The measured wave spectra compared to the target spectrum are illustrated in Figure B.7. The measured time-series compared to target series are given in Figure B.8 and B.9.

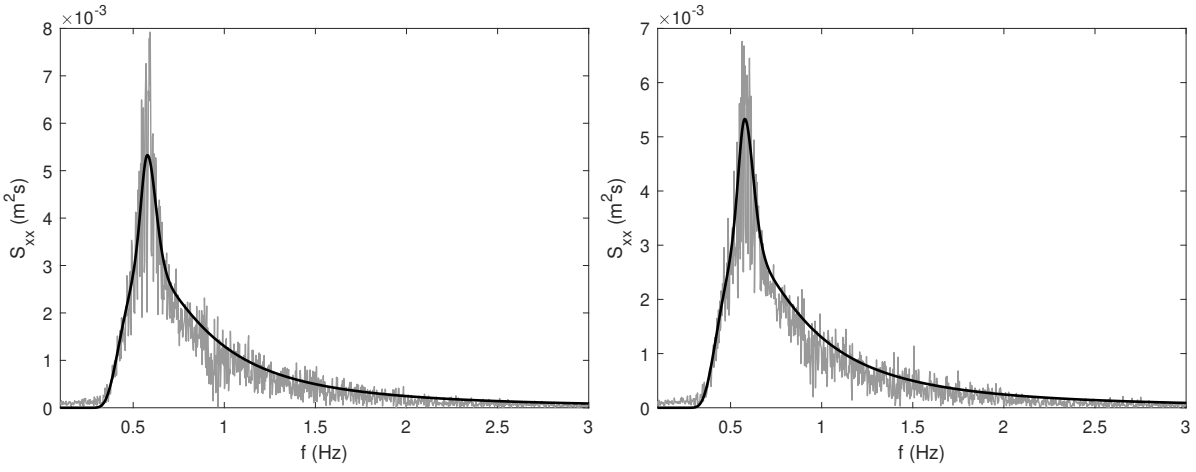

Figure B.7: Recorded wave spectra of CRRW in (—) for the semisubmersible's response in surge in (a) and pitch in (b) compared to target spectra (—).

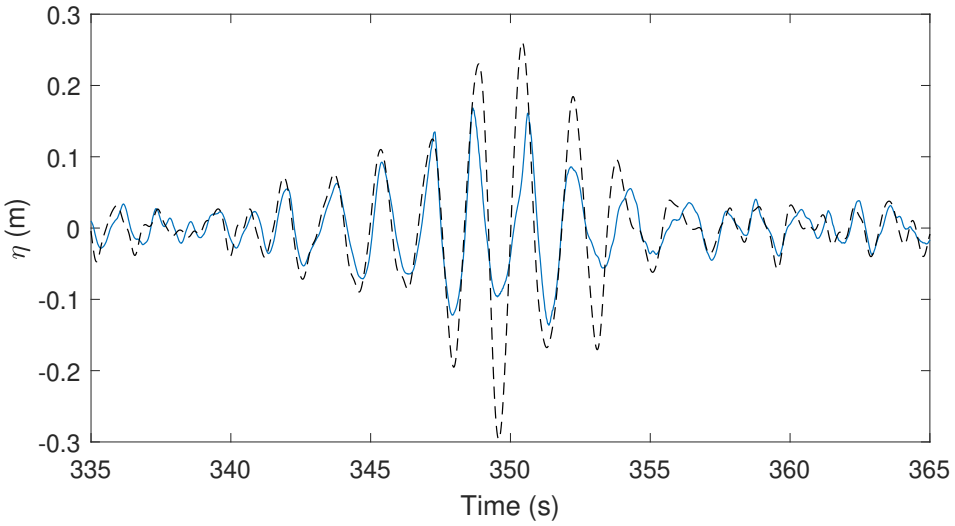

Figure B.8: Measured wave elevations of CRRW (semi) for surge (—) compared to target wave elevations (- - -) during calibration of the conditional wave series.

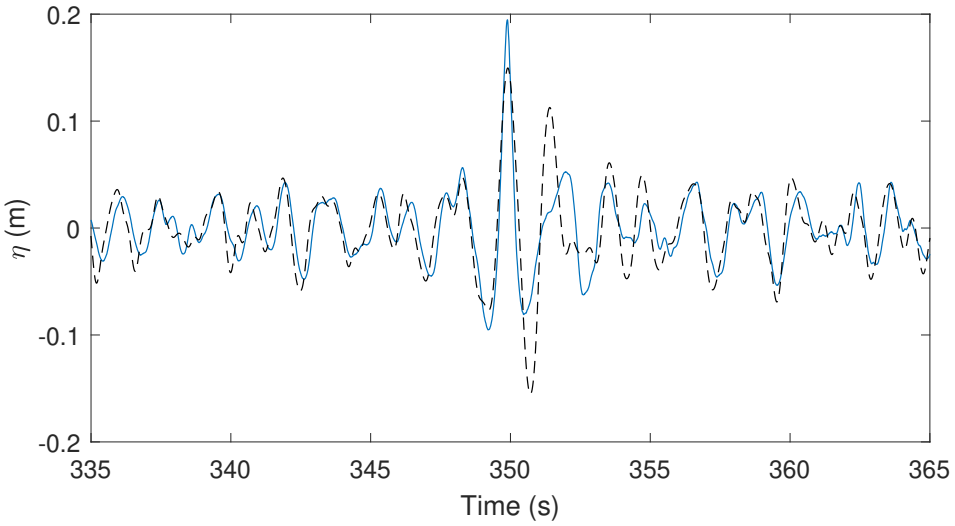

Figure B.9: Measured wave elevations of CRRW (semi) for pitch (—) compared to target wave elevations (- - -) during calibration of the conditional wave series.